A PARAMETRIC INVESTIGATION OF TIP INJECTION FOR ACTIVE TIP VORTEX CONTROL

A THESIS SUBMITTED TO
THE GRADUATE SCHOOL OF NATURAL AND APPLIED SCIENCES
OF
MIDDLE EAST TECHNICAL UNIVERSITY

BY

RIZA CAN DEDEKARGINOĞLU

IN PARTIAL FULFILLMENT OF THE REQUIREMENTS
FOR
THE DEGREE OF MASTER OF SCIENCE
IN
AEROSPACE ENGINEERING
DECEMBER 2010

Approval of the thesis:

A PARAMETRIC INVESTIGATION OF TIP INJECTION FOR ACTIVE TIP VORTEX CONTROL

submitted by **RIZA CAN DEDEKARGINOĞLU** in partial fulfillment of the requirements for the degree of **Master of Science in Aerospace Engineering Department, Middle East Technical University** by,

Prof. Dr. Canan Özgen
Dean, Graduate School of **Natural and Applied Sciences** _____

Prof. Dr. Ozan Tekinalp
Head of Department, **Aerospace Engineering** _____

Asst. Prof. Dr. Oğuz Uzol
Supervisor, **Aerospace Engineering Department, METU** _____

Examining Committee Members:

Prof. Dr. İsmail H. TUNCER
Aerospace Engineering, METU _____

Asst. Prof. Dr. Oğuz Uzol
Aerospace Engineering, METU _____

Prof. Dr. Serkan ÖZGEN
Aerospace Engineering, METU _____

Assoc. Prof. Dr. D. Funda KURTULUŞ
Aerospace Engineering, METU _____

Emre Gürdamar,
Systems Engineer, FNSS _____

Date: _____

I hereby declare that all information in this document has been obtained and presented in accordance with academic rules and ethical conduct. I also declare that, as required by these rules and conduct, I have fully cited and referenced all material and results that are not original to this work.

Name, Last Name: RIZA CAN DEDEKARGINOĞLU

Signature:

ABSTRACT

A PARAMETRIC INVESTIGATION OF TIP INJECTION FOR ACTIVE TIP VORTEX CONTROL

Dedekargınoğlu, Rıza Can
M.Sc., Department of Aerospace Engineering
Supervisor :Asst. Prof. Dr. Oğuz Uzol

December 2010, 79 pages

Wing tip vortex is a challenging phenomenon that reduces the lift generation at the tip region of the wing. For aerial vehicles, several methodologies were presented for the sake of controlling vortices and alleviating effects of tip loss.

In this study, the effect of wing tip injection on wing tip vortex structure was investigated computationally. A NACA0015 profile rectangular wing was employed with an aspect ratio of 3, at a free stream Reynolds number of 67000. 10 identical ejection holes along the wing were prepared chordwise to provide cross sectional air flow in order to determine the net effect of ejection over wing tip vortices and wake flow field.

Study setup consists of a wind tunnel that is 1.6m long, 0.6m wide and 0.6m high, which the wing is attached to one side of it as a cantilever beam. Chord length of the wing is 0.1m and span is 0.3m. A constant free stream air flow is maintained with 10 m/s of velocity.

Computer aided drawing (CAD) and grid generation were carried out using commercial tools. Whole setup was drawn using Rhinoceros. Surface mesh was created using ANSYS Gambit, ANSYS T-Grid software was used for generating the viscous mesh over the wing and finally for volume mesh ANSYS Gambit was utilized once more. FLUENT was chosen to be the flow solution tool with k-ω SST turbulence model.

For 3 different angles of attack cases, respectively, 4°, 8° and 12°, several injection scenarios were defined. There are 3 steady injection cases for each angle of attack case namely, no injection case, uniform injection case, triangular waveform injection case where there is no injection at the leading edge tip whereas there is injection which is equal to the uniform injection velocity at the trailing edge tip. Moreover there are 5 additional scenarios for 8° angle of attack case that are, sinusoidal waveform injection case which consists of a chordwise velocity distribution shape that is a quarter sinus wave where maximum injection velocity is the same as the uniform velocity, reverse triangular waveform injection case where injection velocities were reversed with respect to triangular waveform case, two cases consisting of angled injections having both +15° and -15° with respect to the flapping axis of the wing. The effect of tube walls on the jet injection was neglected for all cases, therefore for the last case, in order to simulate pipe flow, a case is provided with uniform injection velocity.

In that way, regardless of the solution method, a parametric study was performed. Considering each case, non-dimensional 3-axis velocity components, turbulent kinetic energy, vorticity magnitude, pressure, lift and drag values were computed and having the exactly same cases as an experimental study for 8° angle of attack, a comparison of aerodynamic data series was presented.

As results, it's observed that, vortex core locations were shifted upwards and away from the tip region. Increasing the turbulence level of the tip flow by tip injection, inherently the pressure difference became larger, however as the vortices ascend, tip loss decreases. In that way, a significant increase in the lift was observed while drag values are slightly increased, as well.

Keywords: CFD, active tip vortex control, tip injection

ÖZ

AKTİF KANAT UCU GİRDABI KONTROLÜ İÇİN SAĞLANAN KANAT UCU ENJEKSİYONUNUN PARAMETRİK OLARAK İNCELENMESİ

Dedekargınoğlu, Rıza Can
Yüksek Lisans, Havacılık ve Uzay Mühendisliği Bölümü
Tez Yöneticisi :Asst. Prof. Dr. Oğuz Uzol

Aralık 2010, 79 sayfa

Uç girdabı, kanatta taşıma kuvvetini oluşturan alt ve üst yüzeyler arasındaki basınç farkı sonucu kanat uçunda akışın yüksek basınçtan alçak basınca doğru sızmasıyla ortaya çıkan, kanat ucundaki taşıma kuvvetini azaltan akış olayıdır. Havacılık araçlarında girdap yapılarının kontrolü ve uç kayıplarının azaltılması hakkında uygulanan metotlar sunulmuştur.

Bu çalışmada, kanat ucundan sağlanacak hava enjeksiyonun uç girdabına olan etkisi sayısal olarak incelenmiştir. NACA0015 profiline sahip, kanat-açıklık oranı 3 olan bir kanat modellenmiş ve ana akışın Reynolds sayısı 67000 olarak belirlenmiştir. Enjeksiyonun uç girdabına ve ard akış bölgesine olan etkisinin incelenmesi için, kanatta veter boyunca 10 adet özdeş delikten enjeksiyon sağlanmıştır.

Çalışma düzeneği, boyutları 1.6 m (boy), 0.6 m (genişlik) ve 0.6 m (yükseklik) olan bir rüzgar tüneli ve tünel duvarlarından birine sabitlenmiş halde duran kanattan oluşmaktadır. Kanadın veteri 0.1 m, boyu ise 0.3 m'dir. Sabit 10 m/sn hıza sahip ana akış mevcuttur.

Düzeneğin bilgisayarda modellenmesi ve ağ yapılarının oluşturulması ticari yazılımlar ile sağlanmıştır. Sistemin teknik çiziminde Rhinoceros, yüzey ağ yapılarında ANSYS Gambit, kanadı çevreleyen sıkılaştırılmış ağ yapısı için ANSYS T-Grid kullanılmış, geriye kalan hacim ağ yapısının tamamlanması için yeniden ANSYS Gambit kullanılmıştır. FLUENT'te k-ω SST türbülans modeli kullanılarak akış çözülmüştür.

Sırayla 4°, 8° ve 12° hücum açısı için, enjeksiyonsuz, her delikten eşit hızda ve düzenli akışa sahip tek tip enjeksiyon, hücum kenarı ucunda enjeksiyonsuz firar kenarında tek tip enjeksiyon hızına sahip üçgen-dalga tipi enjeksiyon olmak üzere 3 adet senaryo çözülmüştür. Bunların dışında 8° hücum açısında önceki sonuçlarla kıyaslama yapmak amacıyla 5 adet senaryo daha hazırlanmıştır. Firar kenarı ucunda tek tip enjeksiyon hızına sahip hücum kenarında ise enjeksiyonsuz sinüs dalgası formunda hız profiline sahip enjeksiyon sağlanan sinüs dalgası tipi enjeksiyon, hücum kenarı ucunda tek tip enjeksiyon hızına sahip firar kenarında ise enjeksiyonsuz ters üçgen-dalga tipi enjeksiyon ile üçgen ve ters üçgen profiller arasında karşılaştırma yapılmış, kanat çırpma eksenine göre +15° ve -15°'de sağlanan enjeksiyonlar ile ise açılı enjeksiyonun girdap yapılarına olan etkisi açısız senaryolarla ve literatür çalışmalarıyla kıyaslanmıştır. Önceki senaryolarda enjeksiyon tüpü içerisindeki akışın tüp çıkışındaki hız dağılımına etkisi ihmal edildiğinden, son senaryo olarak tüp duvarları içinde ağ yapısı oluşturulmuş ve tek tip akış senaryosunda karşılaştırma yapılmıştır. Her durum için birimsiz olarak 3 eksende hız değişkenleri, türbülans kinetik enerji, girdap magnitüdü parametreleri, ayrıca taşıma ve sürükleme kuvvetlerindeki değişimler birbirleriyle ve deneysel sonuçlarla karşılaştırılmış; aerodinamik bir veri tabanı oluşturulmuştur.

Sonuç olarak, girdap özü konumunun irtifa kazandığı ve kanat uç bölgesinin dışına atıldığı gözlemlenmiştir. Uç enjeksiyonu ile türbülans seviyesi artırılan uç akışında, girdap çevresindeki basınç farkı da artmıştır. Her ne kadar girdap yapısı kuvvetlense de, girdap kanat ucundan uzaklaştığından, uç kaybının azaldığı, buna bağlı olarak kanat taşıma kuvvetinin arttığı, sürükleme kuvvetinin de daha az oranda olsa da arttığı gözlemlenmiştir.

Anahtar Kelimeler: hesaplamalı akışkanlar dinamiği, aktif kanat ucu girdabı kontrolü, kanat ucu enjeksiyonu

To non-humans,

ACKNOWLEDGMENTS

I would like to express my gratitude to Oğuz Uzol, who accepted me as one of his graduate students -even though I have lost a year trying to decide which subject to study- for his supervision and guidance. Studying an interesting subject like this one was his own idea and I literally jumped on it. Having worked on both experimental and computational side of exploring tip vortex phenomenon, I can say that, it was both challenging (considering each case) and entertaining (seeing how tip vortices change with tip injection for a variety of angles of attack).

Secondly, I would like to thank Emre Gürdamar for his efforts while generating the complex grid system. I would not be finishing this work without his help.

Last but not least, I'm thankful for the great music of Mike Patton and his crazy people, Kings of Convenience, Porcupine Tree, John Williams and Pink Floyd. Their songs kept me company during long nights while writing down the thesis.

TABLE OF CONTENTS

LIST OF TABLES

TABLES

LIST OF FIGURES

FIGURES

CHAPTER 1

INTRODUCTION

When a lifting surface, e.g. an airfoil shaped structure, faced with the flow coming towards to it; inherently it splits the flow into two. Due to the shape (camber) of the airfoil and the relative flow angle (figure 1.1), part of the flow that is passing through airfoil suction side (the upper part) tends to accelerate. According to Bernoulli's Principle for inviscid flow, "an increase in the speed of the fluid occurs simultaneously with a decrease in pressure or a decrease in the fluid's potential energy". In this case, pressure of the flow that is passing through pressure side is greater than the pressure at suction side. That difference generates a force, namely lift.

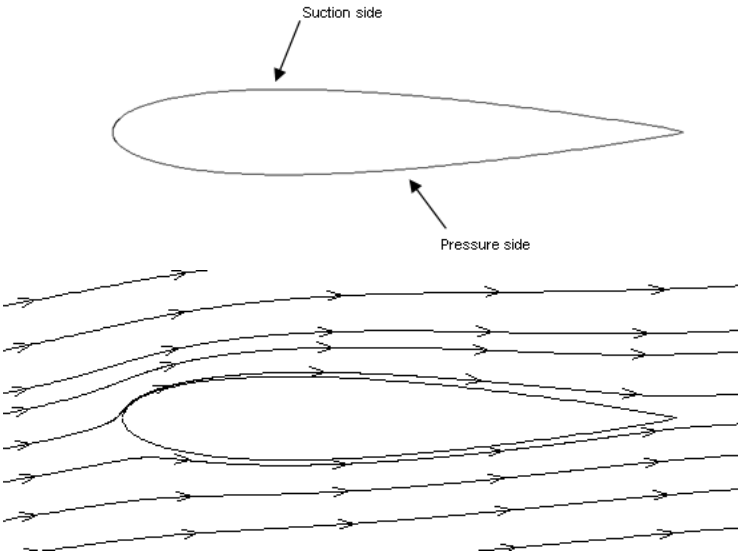

Figure 1.1: NACA 0015 airfoil and streamtraces, @ 6° angle of attack.

Tip vortices are also generated by that pressure difference, which is a side effect of lift (and it can be associated with induced drag). At the tip region of the lifting surface, airflow actually **leaks** from high-pressure-side (pressure side) to low-pressure-side (suction side) and

follows wake trajectory with a circular shape of flow pattern, reducing the pressure difference and lift (figure 1.2).

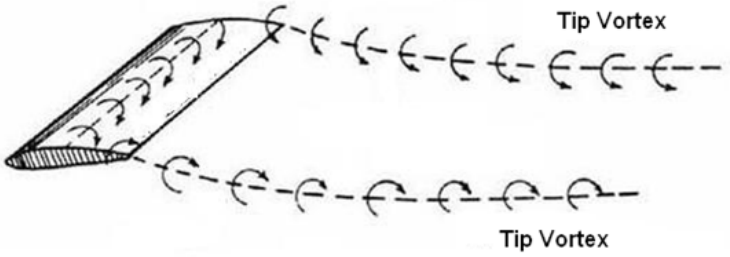

Figure 1.2: Tip vortex in 3D

As well as being three dimensional, vortex structures have low-pressure characteristics because of high spinning velocity of the core and have high turbulence intensity. Primary and secondary vortices and interactions between both are making tip vortex a highly complex phenomenon.

Tip vortices basically lead to a momentum loss at the very tip of the wing, and longer the chord length, vortex structures that are developed become larger. Thus, making the aspect ratio of a wing larger, lessen the effects of tip vortices, as seen on long distance jets for higher fuel efficiency.

Tip vortices are crucial due to their effects on aircrafts; for airplanes it increases loss of lift and so landing and take-off distances, considering that it decreases the efficient wing planform area. Tip vortices strongly influence airport traffic, as trailing vortices of larger aircrafts may lead to dramatic consequences for lighter aircrafts; even vortex structure of large jets can be as big as the entire light aircraft. For helicopters, tip vortex emerged from one blade increases the disturbance of flow on the path line; blade vortex interactions occur and eventually it may cause blade failure. Again for rotating turbomachinery, the formation of larger tip vortices is directly proportional to the width of the blade tip gap, which diminishes the efficiency of rotating part. Aircrafts that has low-aspect-ratio wing, e.g. UAVs, are more severely affected by wing tip vortices as larger amount of lift loss is occurred; using the . Considering the importance, it is essential to study on that particular subject in order to predict the characteristics and introduce control techniques for higher efficiency.

There are several studies that have performed to minimize effects of tip vortices, based on flow control mechanisms. Basically, they can be classified into two as passive and active flow control systems. Passive control systems consist of non-moving devices or tip extensions in order to reduce the effect, such as winglets and flaps (figure 1.3). Winglets are often employed for large airliners for minimum fuel consumption, by allowing the entire wing span generating lift. However beneficial the passive systems are, they become disadvantageous as being not adaptable for varying flight and flow conditions. Conversely, active systems are adjustable and they maintain the stability for whole flight envelope; yet those systems are inherently more complicated and expensive. Onboard blowing & suction systems, ejection nozzles, synthetic jet flows, electrostatic & plasma systems and acoustic interaction methods are some examples for active control systems.

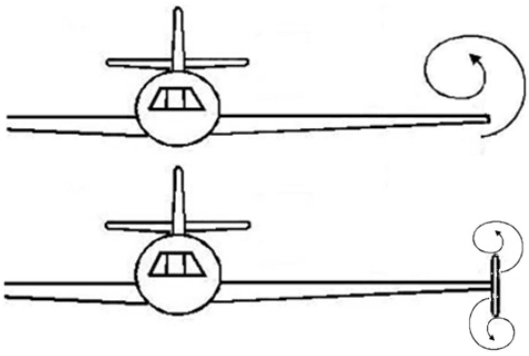

Figure 1.3: Tip vortex patterns

1.1 Literature Survey

Tip vortex control mechanisms subject is widely studied in recent years. As results, controlling the wing tip vortices, forces and moments on wing control surfaces can be increased, drag force and noise can be reduced (Gursul et al. [2]). Activation of solid surfaces (e.g. activated Gurney flaps along the wingspan, Matalanis et al. [3], or active trailing edge tabs, Panagakos and Lee [7], or wing tip flaps, Greenblatt et al. [11]) is one way of controlling tip vortices, while wing tip injection mechanisms that are less complicated comparing to mechanical surface activation methods are more popular and frequently studied. Tip flow that is injected perpendicular or angled to the free stream flow is proved to alter strength, location and core structure of vortices (Margaris and Gursul [19]). In general, steady and pulsed injection methods were used in tip vortex control studies (e.g. Tavella et al. [25], Heyes and Smith [20], Coton et al. [14], Karthikeyan and Baeder [18,12], Margaris and Gursul [6]). In those studies basic principle is, maintaining a positive mass flow to airflow, however, zero-mass-flow type synthetic jets are used in order to control tip vortices, as well

(Vasilescu and Dancila [21], Margaris and Gursul [8]). Computational studies in order to determine effects of suction and injection have shown an increase in lift (suction near trailing edge) and decrease in skin friction, respectively (Shojaefard et al. [13]). Observation of wing tip vortex dependence with angle of attack with FLUENT software (May [15]) and LES (Large Eddy Simulation) for tip vortex around an airfoil (Cai [9]) are some numerical study examples. Studies on MAVs (micro aerial vehicles) show that performance of aircrafts with low-aspect-ratio wings drastically decrease by tip losses (Viieru et al. [16]). Tip vortex control has a critical importance for turbomachinery flows, too. Tip vortices that are dominating blade tip flows, are restricting pressurizing and depressurizing capabilities of compressors and turbines, hence decreasing component efficiencies as well as distorting the stability (Smith [27], Wisler [26], Cumpsty [24]). Therefore, control of tip leakage and tip vortices is a major topic on studies related to turbomachinery flows (Bae et al. [17], Lu et al. [10], Nie et al. [4], Geng et al. [5]).

In conclusion, tip vortices, the inevitable consequence of lift generation, are one of the phenomena that have highest aerodynamic complexity. Controlling the tip vortices with tip injection is especially a beneficent method for engineering systems like wind turbines, helicopters and UAV's, i.e. for UAV applications tip injection is not only an artificial lift increment device by increasing the effective wing area but also a substitute for control surfaces; servo systems may be replaced with lighter air compression tanks. As technology develops, there will be both experimental and computational possibilities that will enable aerodynamicists to study deeper on this subject.

1.2 Objectives

In this thesis, it is intended to present the effect of tip injection to the tip vortices, as a computational study. For a wing that has NACA0015 profile with an aspect ratio of 3 with 4°, 8° and 12° angle of attack configurations, cases with several different injection scenarios were simulated, that are:

- 4° angle of attack configuration:
  - No injection
  - Uniform injection, 85 m/s injection velocity from each hole
  - Triangular waveform injection, 0 m/s injection velocity at leading edge, 85 m/s injection velocity at trailing edge, from corresponding holes.
- 8° angle of attack configuration, first three cases are the same with previous configuration:

  - No injection
  - Uniform injection, 85 m/s injection velocity from each hole
  - Triangular waveform injection, 0 m/s injection velocity at leading edge, 85 m/s injection velocity at trailing edge from corresponding holes, constant velocity increment for each hole.
  - Sinusoidal waveform injection, 0 m/s injection velocity at leading edge, 85 m/s injection velocity at trailing edge, yet, the shape of the velocity distribution over the chord is a quarter sinus wave.
  - Inverse triangular waveform injection, reversed version of the triangular waveform injection case, where the maximum injection is at leading edge and zero injection is at trailing edge.
  - +15° angled uniform injection, where the injection has a tendency to act like a positive angled wing tip.
  - -15° angled uniform injection, vice versa.
  - Uniform injection with fully developed flow, where the effect of tube walls on the jet injection was included for all cases, in order to simulate the pipe flow.
- 12° angle of attack configuration, same cases with 4° version:
  - No injection
  - Uniform injection, 85 m/s injection velocity from each hole
  - Triangular waveform injection, 0 m/s injection velocity at leading edge, 85 m/s injection velocity at trailing edge, from corresponding holes.

As results, the change in the location and structure of the tip vortices was observed by means of a 3D Navier – Stokes solver, FLUENT. A validation study, which includes the comparison of computational results and experimental data by means of pressure distribution, vortex formation, strength and core location was presented as well.

CHAPTER 2

COMPUTATIONAL SETUP

In order to model the setup and simulate tip flows, several well-known commercial tools were used namely, Rhinoceros, ANSYS Gambit, T-Grid and FLUENT. Computations were conducted on a PC contained an Intel® Xeon® 2.66 GHz processor with 8 cores and 16 GB of RAM. A single run of 3500 iterations lasted for 30 hours.

2.1 Geometrical Details

First of all, wing model and wind tunnel were drawn (figure 2.1) with the Rhinoceros which is a NURBS[1] modeling software, where the dimensions are as follows:

Table 2.1: Setup dimensions

Setup Dimensions	
Wind tunnel length:	1600 mm
Wind tunnel width:	600 mm
Wind tunnel height:	600 mm
Wing chord length:	100 mm
Wingspan:	300 mm

[1] "Non-uniform rational basis spline (NURBS) is a mathematical model commonly used in computer graphics for generating and representing curves and surfaces which offers great flexibility and precision for handling both analytic and freeform shapes." http://en.wikipedia.org/wiki/Non-uniform_rational_B-spline

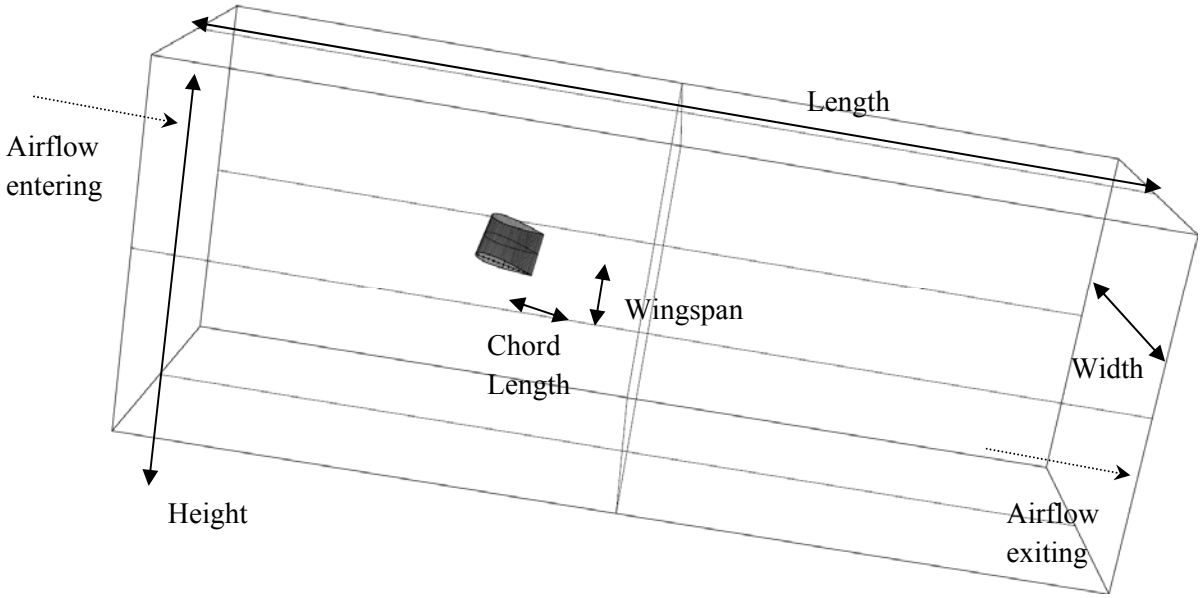

Figure 2.1: Wind tunnel and wing geometry

The wind tunnel is designed to be a rectangular prism with inlet and exit gaps, with a wing that has NACA0015 profile, 0.1 m chord length and 0.3 wingspan dimensions. The wing is located by the left wall of tunnel as a cantilever beam with respect to the observer that is looking from inlet to exit. There are 10 identical injection tubes located along chord-wise on the wing which are 2.40mm in diameter each. Locations of the holes were determined to be in accordance with the experimental setup. The distance between leading edge and center of the first hole is 5mm whereas it's 14 mm between trailing edge and center of the last hole. The distances between centers of the consecutive holes are 9 mm each. Tip shape is squared-off type, and there are no tip extensions. Geometrical details are shown below on figure 2.2.

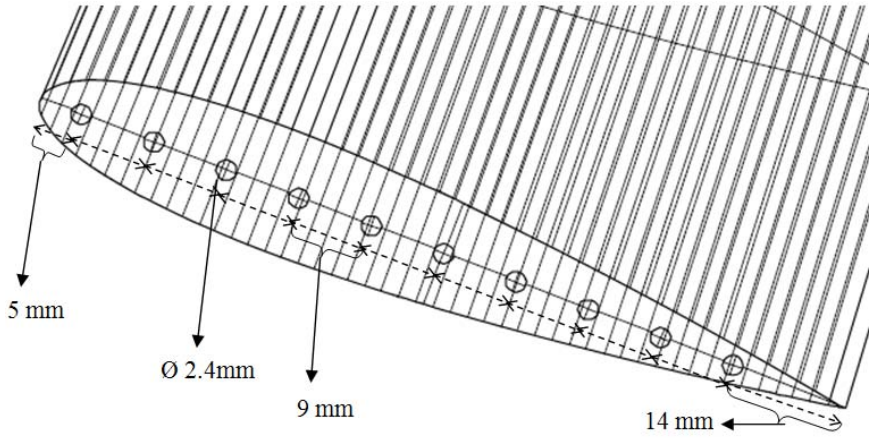

Figure 2.2: Dimensions of holes

2.2 Mesh Generation

After the system was modeled, grid generation started. First of all, all the surface grids are built with unstructured mesh, by using Gambit. For higher resolution, critical spots, edges and faces are fine meshed, yet it gets coarser gradually (figure 2.3 & 2.4). Mesh sizes are the largest at the wind tunnel walls, where wing and jet velocity inlet surfaces have the finest mesh structure.

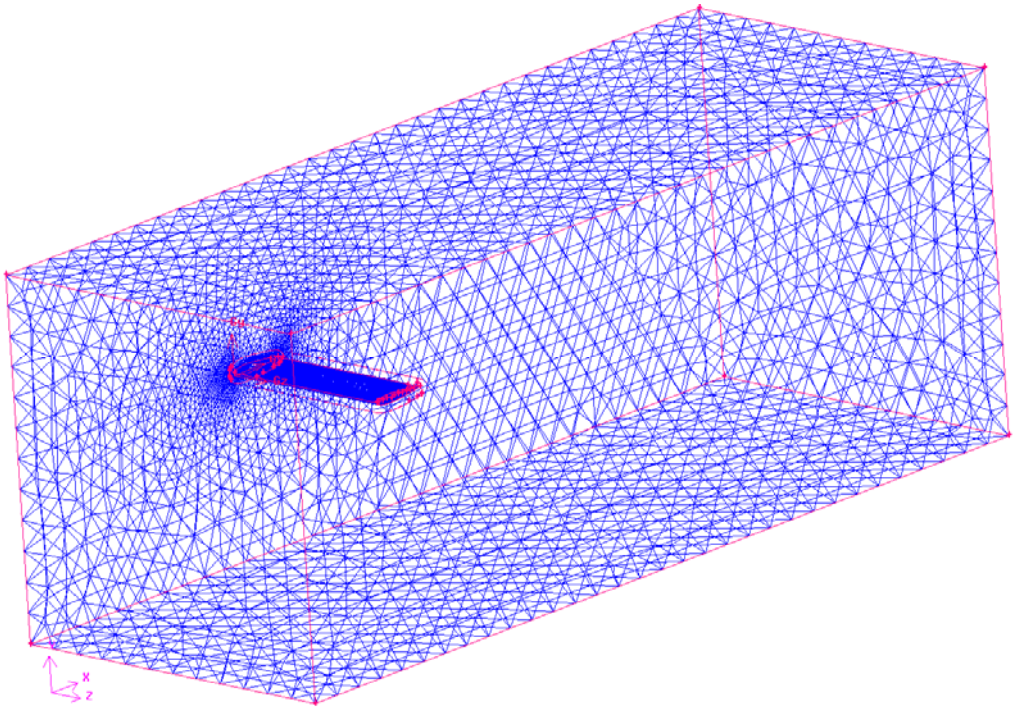

Figure 2.3: Surface mesh generation

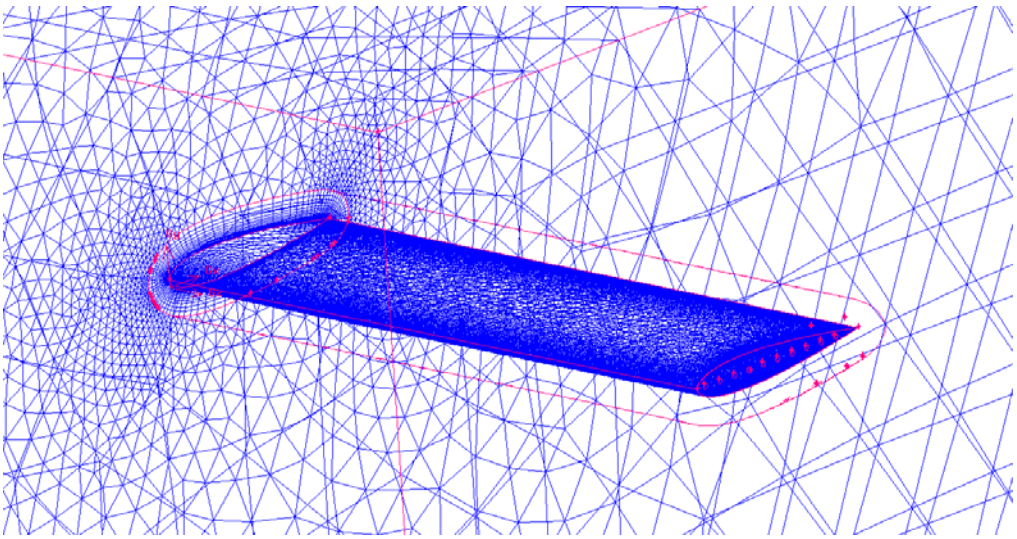

Figure 2.4: Close up look to wing surface mesh

After surface mesh is generated, in order to create a border pattern and visualize boundary layer flow, a viscous mesh of a prism cap was decided to be employed; which is generated using unstructured mesh on T-Grid, considering the complex structure of airflow over the wing (figure 2.5). The spacing normal to the solid surface required to yield 1 grid point in the laminar sublayer value was computed as 0.000276 m as the first height [28]; 28 prism layers were constructed for the viscous cap.

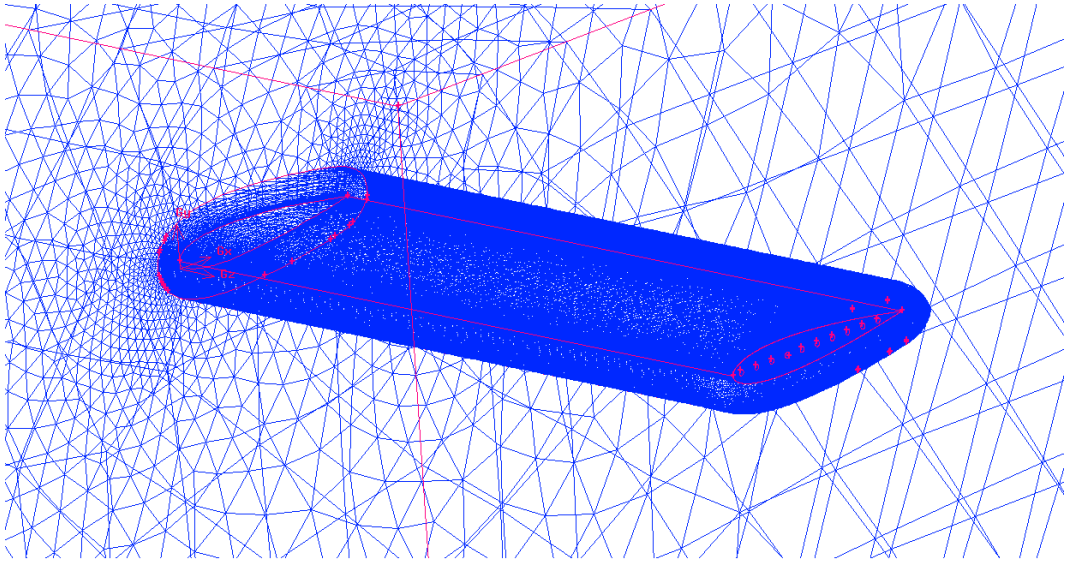

Figure 2.5: Prism cap

In order to increase the resolution especially at the tip and trailing wake, two rectangular planes which are defined as “size functions”, were located at those regions. Fine grid was generated on the planes and the mesh size gets larger through the far field while the volume mesh is built up. One of the planes was extended along the trailing edge in the direction of mainstream, in order to be able to predict trailing vortices in wake region correctly where the other rectangular plane is placed right at the tip of the wing and extended through injection direction, to observe the interactions between mainstream and tip flow properly (figure 2.6).

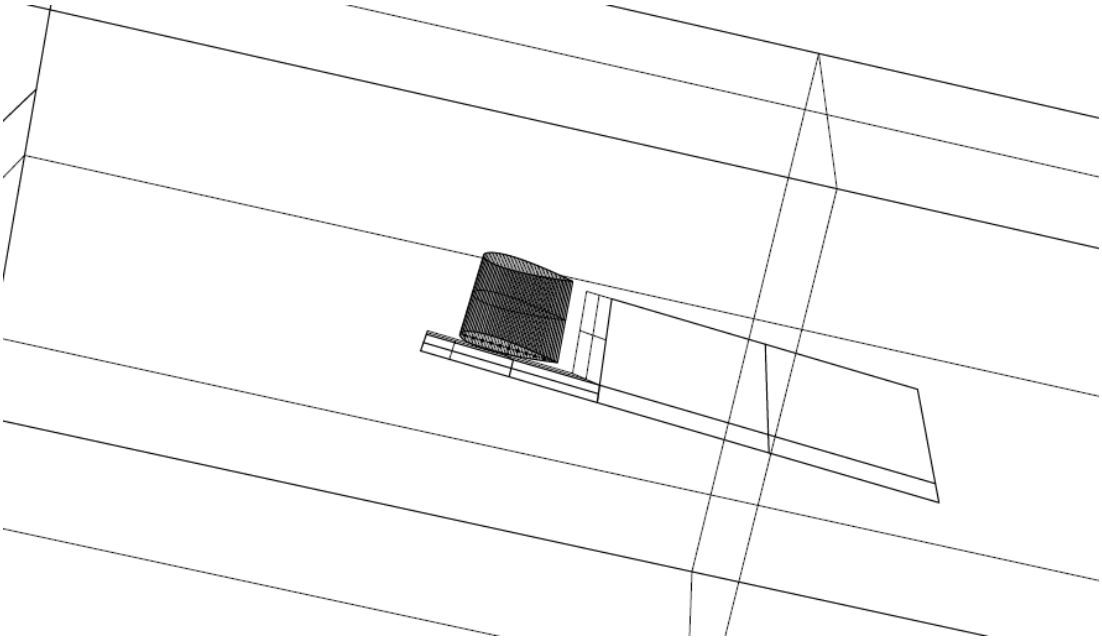

Figure 2.6: Planar size functions

After all the surface meshes were completed and size functions were assigned to the planar surfaces, generation of volumetric mesh has started. Volume mesh was made by employing ANSYS Gambit once more. Using the rectangular planes and viscous cap as the starting surfaces where the grid is the finest, whole volume mesh inside the wind tunnel was constructed accordingly. In total, the grid system was generated consisting of 2062656 prism elements. Furthermore, in order to validate the quality of the mesh, planar cross sections of volumetric grid system by means of three axes are provided and presented below (figure 2.7, 2.8, 2.9).

For the sake of computational time and memory requirements and considering the diameter of tubes, there was no volume mesh assigned inside the tubes. Tubes were considered to be closed at the tip and were treated as surfaces that have velocity exit boundary condition; however it is essential to validate this model and compare with fully developed tube flow (FDF). For one case, i.e. uniform injection with 8° angle of attack configuration, a validation case was prepared with additional tubular grid where the total number of cells increased from $2x10^6$ to $3.5x10^6$. Minor differences were observed in the results after the comparison of both cases, revealing that there is no need for a correction factor.

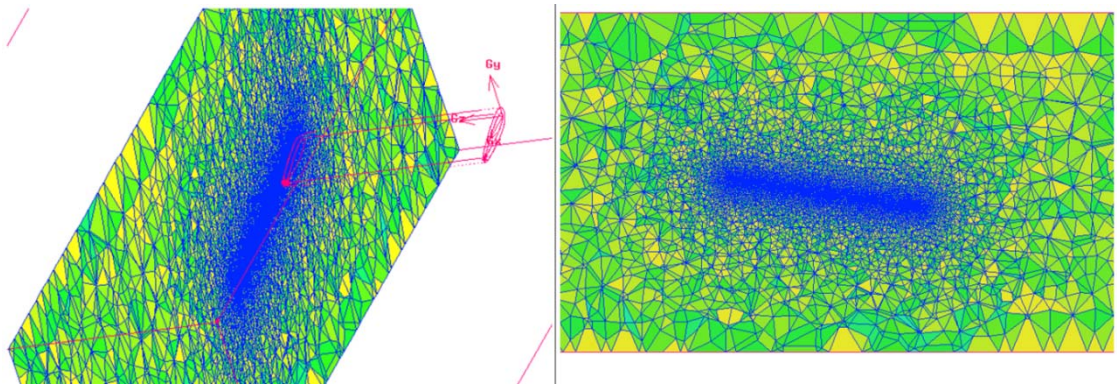

Figure 2.7: Cross section of volume mesh on XY plane

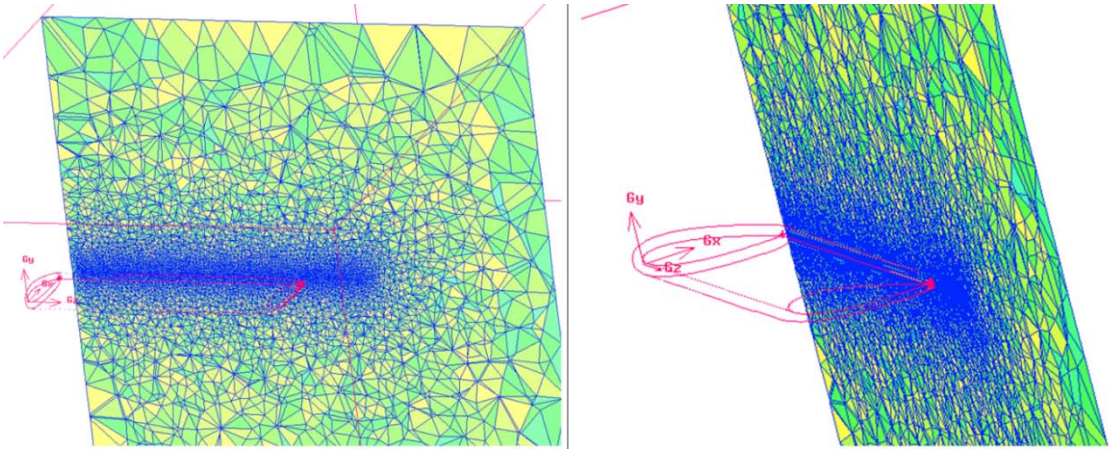

Figure 2.8: Cross section of volume mesh on YZ plane

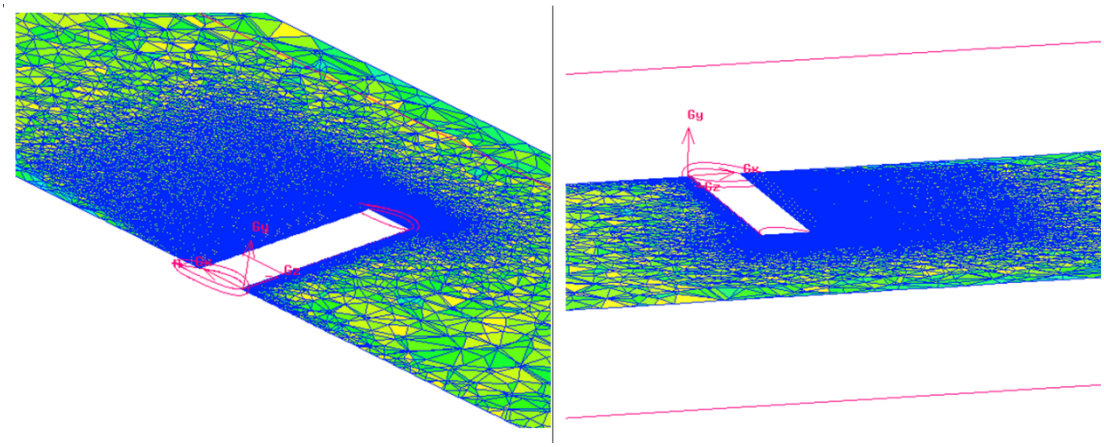

Figure 2.9: Cross section of volume mesh on XZ plane

2.3 FLUENT Settings

FLUENT, which a complete computational fluid dynamics software package, is a tool that solves the governing equations (for mass, momentum, energy, and additional scalars) separately or segregated from each other in order to obtain the fluxes of various quantities through the domain in complex geometries using the discretized control-volume based technique. Integral based governing equations are converted to algebraic equations for the whole meshed domain and then solved numerically. All governing equations are applied to individual cells that are in the domain of computation, yielding discrete equations that conserve each quantity on a control-volume basis. After the initialization of the system with respect to the desired variable, iterations start and procedure ceases right after the convergence criteria are met (figure 2.10). FLUENT settings showing the options chosen in generating the discretization and model flow for this case are as follows (table 2.2).

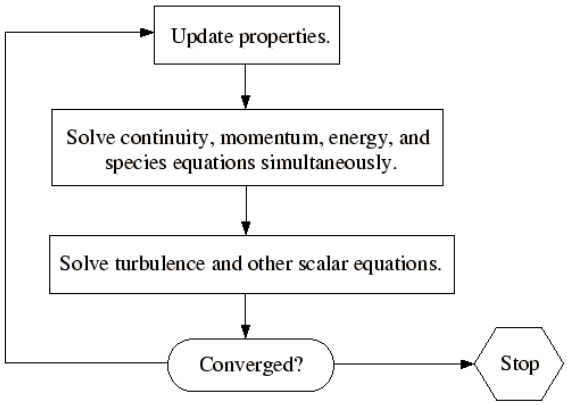

Figure 2.10: FLUENT procedure flowchart [29]

Table 2.2: FLUENT settings

FLUENT Settings	
Model	
Precision	Single
Solver	Density Based
Formulation	Implicit
Space	3D
Time	Steady
Gradient Option	Green-Gauss Node Based
Viscous Model	SST k-ω
Solution Controls / Discretization	
Flow	Second Order Upwind
Turbulent Kinetic Energy	First Order Upwind
Specific Dissipation Rate	First Order Upwind

2.4 Reynolds-Averaged Approach and Turbulence Modeling

Navier-Stokes equations, derived from application of Newton's second of motion to fluid motion, use the assumption that fluid stress is the sum of a diffusing viscous term that is proportional to the velocity gradient, in addition to a pressure term and describe the motion of fluid substances accordingly. Yet the numerical solution of the Navier-Stokes equations for turbulent flow is quite challenging, considering crucially varying mixing-length scales in the turbulent flow increasing the computational time to some uneconomical scale.

Reynolds averaging idea proposed by Osborn Reynolds, i.e. Reynolds decomposition, is mathematically separating the average and fluctuating parts of a quantity. A quantity such as a velocity value that can be decomposed into time average, which is a steady component and perturbations as follows:

$$u(x,y,z,t) = \overline{u(x,y,z)} + u'(x,y,z,t)$$

The time averaged part is denoted with $\bar{u}$ whereas u' part represents fluctuations where the time average is equal to zero according to the Reynolds operators, i.e. mathematical operators for averaging a parameter over a group of action.

RANS (Reynolds Averaged Navier-Stokes) equations, i.e. averaging of Navier-Stokes equations by means of Reynolds decomposition approach, represent transport equations for mean quantities only, considering all the scales of turbulence being modeled. Using mean flow variables significantly decreases the computational time and effort, especially when the mean flow is steady; reaching a steady-state solution will be obtained economically considering that governing equations are free of time derivates. Reynolds operators constitute the rule of thumb while deriving RANS equations; the equations are as follows in tensor notation.

$$\frac{\partial \bar{u}_i}{\partial x_i} = 0$$

$$\rho \frac{\partial \bar{u}_j \bar{u}_i}{\partial x_j} = \rho \bar{f}_i + \frac{\partial}{\partial x_j}\left[-\bar{p}\delta_{ij} + 2\mu \bar{S}_{ij} - \rho \overline{u_i' u_j'}\right]$$

Where u_i is the i^{th} velocity component, x_i is i^{th} the axial component, ρ is density, f_i is a vector representing external forces, δ_{ij} is Kronecker delta, μ is dynamic viscosity, $\bar{S}_{ij}$ is the mean rate of strain tensor.

Left hand side of the equation denotes the change in mean momentum of the fluid particle according to the unsteadiness in the mean flow and convection by it. At the right hand side, the mean body force, the isotropic stress of the mean pressure field, viscous stresses and Reynolds stress ($\rho\overline{u_i'u_j'}$) is present. Being a nonlinear term, in order to solve Reynolds stress and close RANS equations, additional models, namely turbulence models, are required. The Reynolds-averaged approach uses models such as Spalart-Allmaras, $k-\epsilon$ and its variants, $k-\omega$ and its variants, and the RSM (Reynolds stress model), where k is turbulent kinetic energy, ϵ is turbulent dissipation and ω is specific dissipation, determining the scale of turbulence.

There's no single turbulence model that is universally accepted for all kind of numerical cases. Certain considerations must be taken into account before choosing the right turbulence model such as: the physics of the flow, solutions practiced for predecessors of the same class of problems, time and computational resource restrictions and required precision level.

Considering the computational power and complexity of the case, SST (Shear Stress Transport) $k-\omega$ was chosen to be the most appropriate turbulence model. SST $k-\omega$ which is a refined version of standard $k-\omega$, was developed by Menter [22], where advantages of both $k-\omega$ and $k-\epsilon$ models come up, by the usage of SST formulation. First of all, the use of $k-\omega$ formulation in the subparts of the boundary layer enables the model functioning all the way through the wall and viscous sublayer; in that way SST $k-\omega$ became useful as a low Reynolds number model without any extra damping functions. Moreover, SST formulation also shows $k-\epsilon$ behavior in the free stream, thus it prevents from the problem of $k-\omega$ being extremely sensitive to the inlet free stream turbulence properties. These features make SST $k-\omega$ model more precise and trust worthy for a wider range of flows (e.g., adverse pressure gradient flows, airfoils, transonic shock waves) [29].

2.5 Boundary Conditions

Definition of boundary conditions on FLUENT is straight forward. Considering the uniform velocity of 10 *m/s* of main flow which was introduced as air, inlet face was assigned with velocity inlet boundary condition. Using the gauge pressure for the entire domain, it was decided to assign pressure outlet to exit face with 0 *Pa*. Surface that the wing is attached was considered to be symmetry boundary condition, such that variations of all quantities perpendicular to this surface is zero. Rest of the wind tunnel walls was given wall boundary condition, as well as wing surfaces. Components and corresponding boundary conditions are presented as follows (figure 2.11):

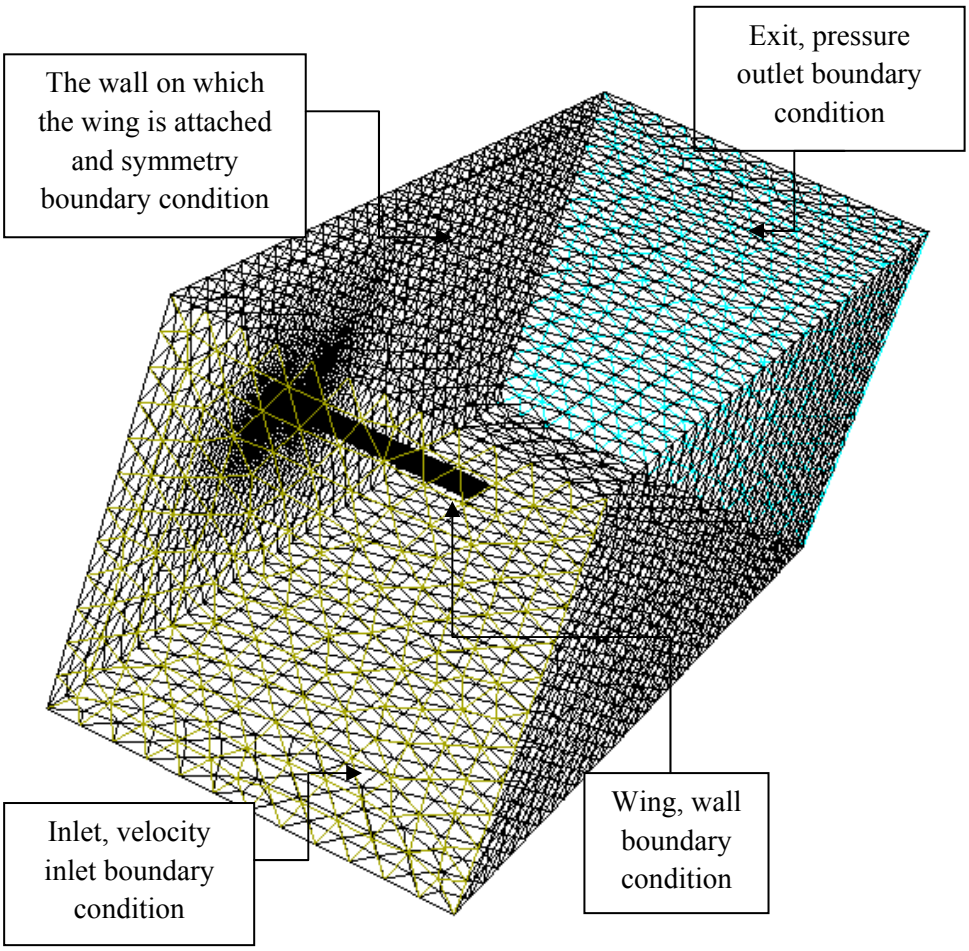

Figure 2.11: Grid topology and boundary conditions

There are 3 different boundary conditions given to the tubes. Two of them are assigned to the exit surfaces of tubes, velocity inlet and wall boundary conditions (figure 2.12), while they were treated as velocity inlet walls instead of developing tube flow. Secondly, in order to visualize the case with fully-developed flow (FDF), inside of the tubes were meshed (figure 2.13), and boundary conditions provided accordingly. In that way, comparison of the same injection case was conducted by means of different tube flow.

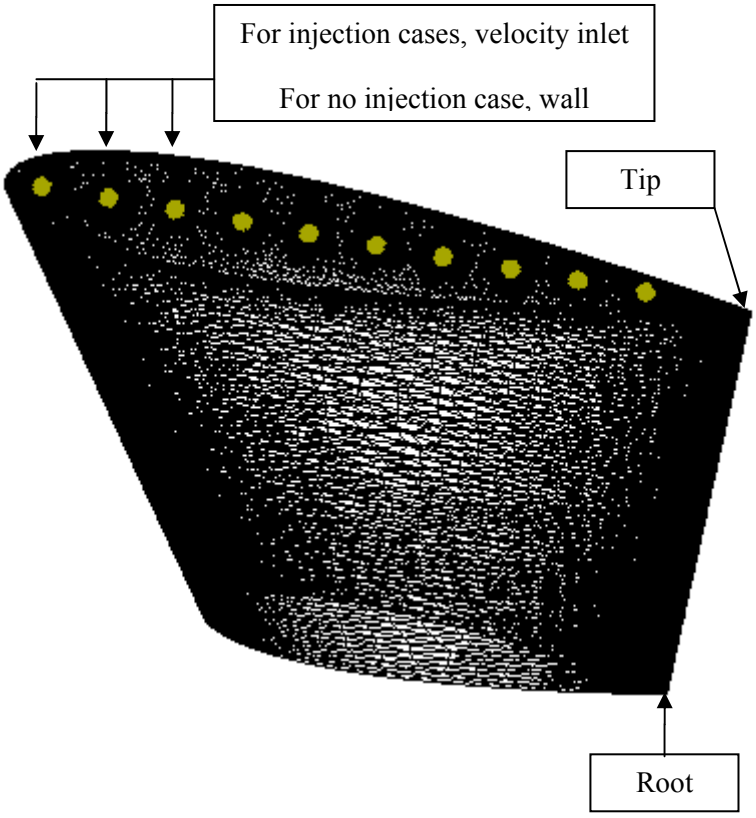

Figure 2.12: Tube exit boundary conditions

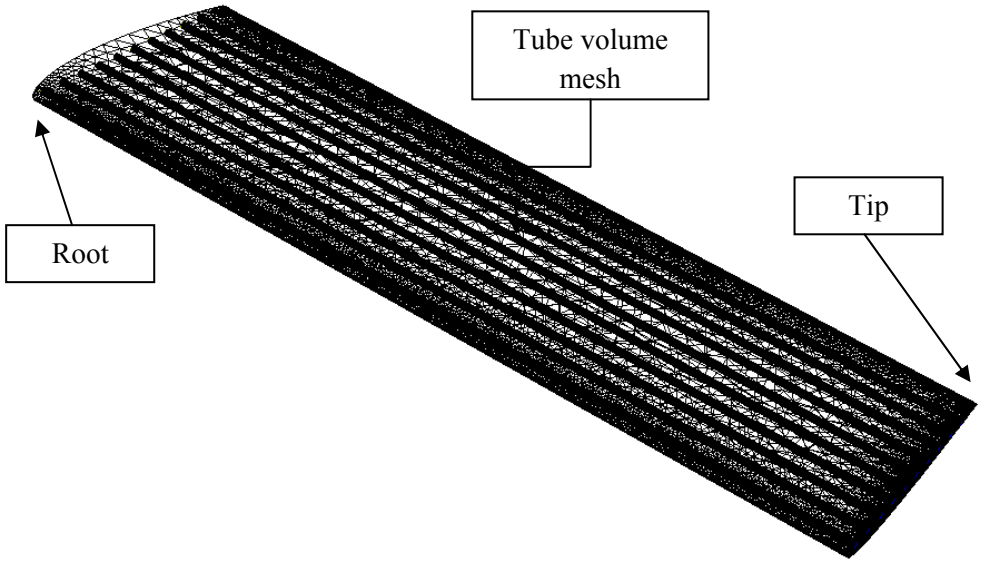

Figure 2.13: Tube volume mesh

2.6 Convergence

The simulation run lasted 3500 iterations at least, due to the convergence characteristics of the particular case; the lift coefficient and the drag coefficient were monitored and residuals of lift coefficient are plotted in figures below (figure 2.14, 2.15, 2.16). Especially for 4° angle of attack cases, residuals have certain fluctuating behavior; however they tend to attenuate by the end of the simulation. Percent variation in lift coefficient was $1x10^{-3}$ and in drag coefficient was $2x10^{-3}$

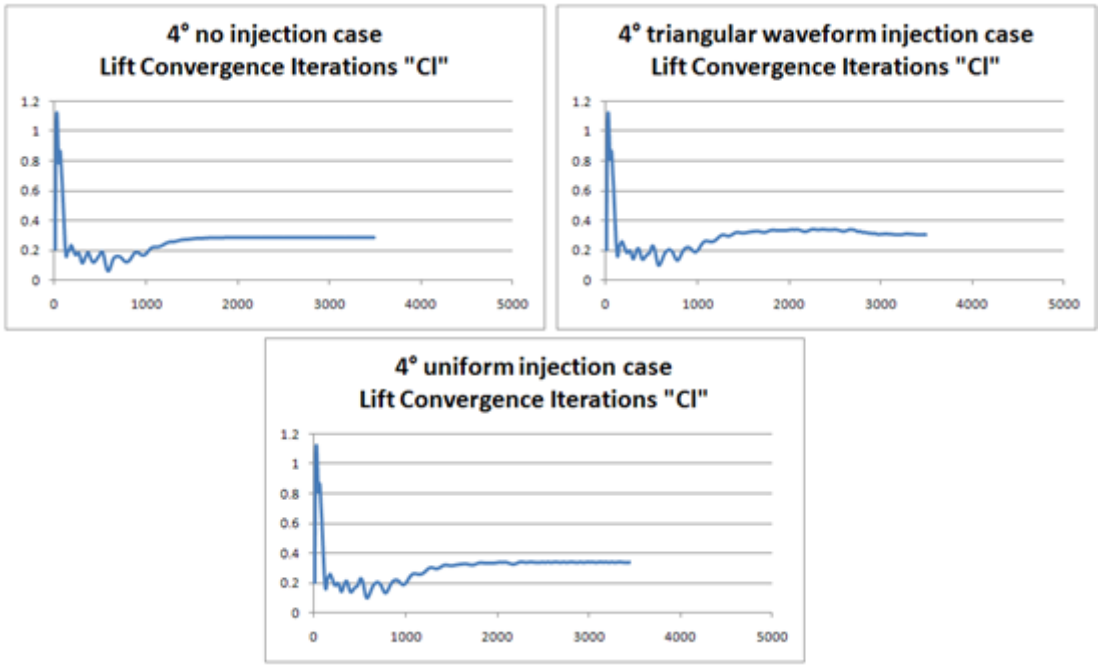

Figure 2.14: Lift coefficient residual plots for 4° angle of attack configurations

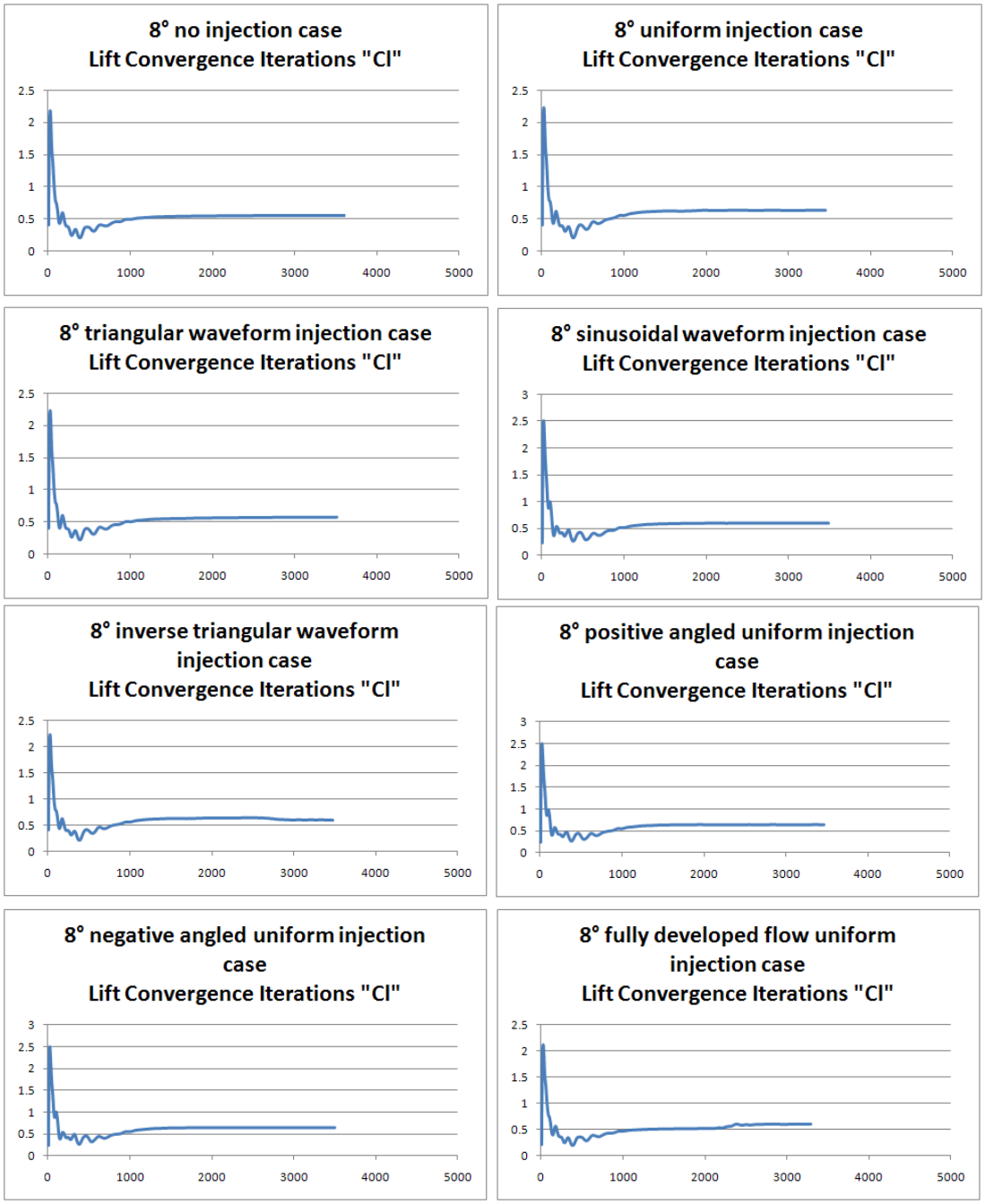

Figure 2.15: Lift coefficient residual plots for 8° angle of attack configurations

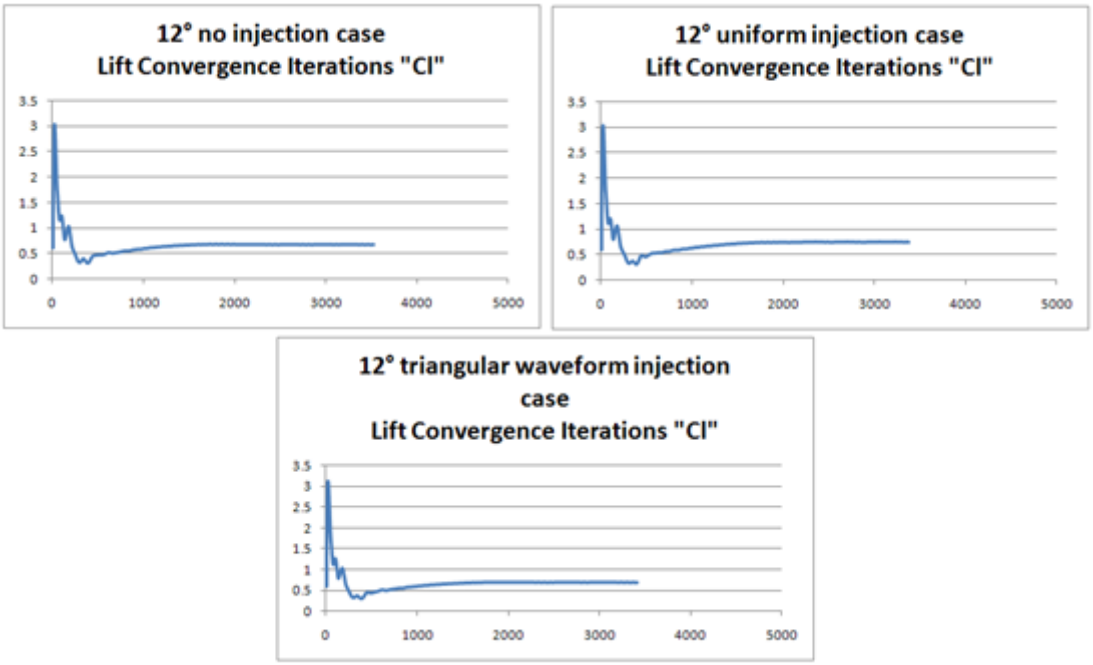

Figure 2.16: Lift coefficient residual plots for 12° angle of attack configurations

2.7 Flow Solution and Injection Scenarios

Solutions were prepared with 3 different angles of attack of the wing, 4°, 8° and 12° and 3 different injection cases, no injection, uniform injection and triangular waveform injection respectively. There are 5 more cases introduced for wing configuration of 8° angle of attack, that are, sinus waveform injection, inverse triangular waveform, 2 angled uniform injection and uniform injection that includes the fully developed flow (FDF) (figure 2.17). Fluid flow is modeled as a low Reynolds number flow, i.e. 67000. Injection velocities are determined by using jet momentum coefficient factor, C_μ [23].

$$C_\mu = \frac{\dot{m}_j U_j}{\frac{1}{2}\rho_\infty U_\infty^2 S}$$

Where $\dot{m}_j$ is the mass flow rate of jet injection per hole and U_j is jet velocity, the denominator part consists of dynamic pressure and planform area of the wing.

According to the study of Mercan et al. [1], it's shown that the effect of tip injection on tip vortices increases with increasing injection velocity; yet it diminishes after a certain velocity value. Therefore, 85 m/s injection velocity, leading to a C_μ value of 0.22 was chosen to be the maximum injection velocity, in order to visualize the net effect properly and to be in accordance with experiments, as well. Injection velocity profiles for different cases are presented in table 2.3.

Table 2.3: Jet momentum coefficients and injection velocities with respect to each hole

				Leading Edge				Injection Holes					Trailing Edge
	Injection Cases	C_μ	Speed (m/s)	no.1	no.2	no.3	no.4	no.5	no.6	no.7	no.8	no.9	no.10
1	Uniform	0.220	Injection	85,0	85,0	85,0	85,0	85,0	85,0	85,0	85,0	85,0	85,0
			Airflow	10,0	10,0	10,0	10,0	10,0	10,0	10,0	10,0	10,0	10,0
2	Triangular Waveform	0.054	Injection	0,0	9,4	18,9	28,3	37,8	47,2	56,7	66,1	75,6	85,0
			Airflow	10,0	10,0	10,0	10,0	10,0	10,0	10,0	10,0	10,0	10,0
3	No	0.000	Injection	0,0	0,0	0,0	0,0	0,0	0,0	0,0	0,0	0,0	0,0
			Airflow	10,0	10,0	10,0	10,0	10,0	10,0	10,0	10,0	10,0	10,0
4	Sinus waveform	0.084	Injection	0,0	14,8	29,1	42,5	54,6	65,1	73,6	79,9	83,7	85,0
			Airflow	10,0	10,0	10,0	10,0	10,0	10,0	10,0	10,0	10,0	10,0
5	Inverse Tr. Waveform	0.054	Injection	85,0	75,6	66,1	56,7	47,2	37,8	28,3	18,9	9,4	0,0
			Airflow	10,0	10,0	10,0	10,0	10,0	10,0	10,0	10,0	10,0	10,0
6	Uniform w/ (FDF)[2]	0.215	Injection	85,0	85,0	85,0	85,0	85,0	85,0	85,0	85,0	85,0	85,0
			Airflow	10,0	10,0	10,0	10,0	10,0	10,0	10,0	10,0	10,0	10,0
7	Uniform +15° ang.	0.220	Injection	85,0	85,0	85,0	85,0	85,0	85,0	85,0	85,0	85,0	85,0
			Airflow	10,0	10,0	10,0	10,0	10,0	10,0	10,0	10,0	10,0	10,0
8	Uniform -15° ang.	0.220	Injection	85,0	85,0	85,0	85,0	85,0	85,0	85,0	85,0	85,0	85,0
			Airflow	10,0	10,0	10,0	10,0	10,0	10,0	10,0	10,0	10,0	10,0

[2] While computing cμ of uniform injection with FDF, mean velocity and density distribution at the tip were taken into consideration. Tubular flow exits with a slightly lower density value, making cμ = 0.215.

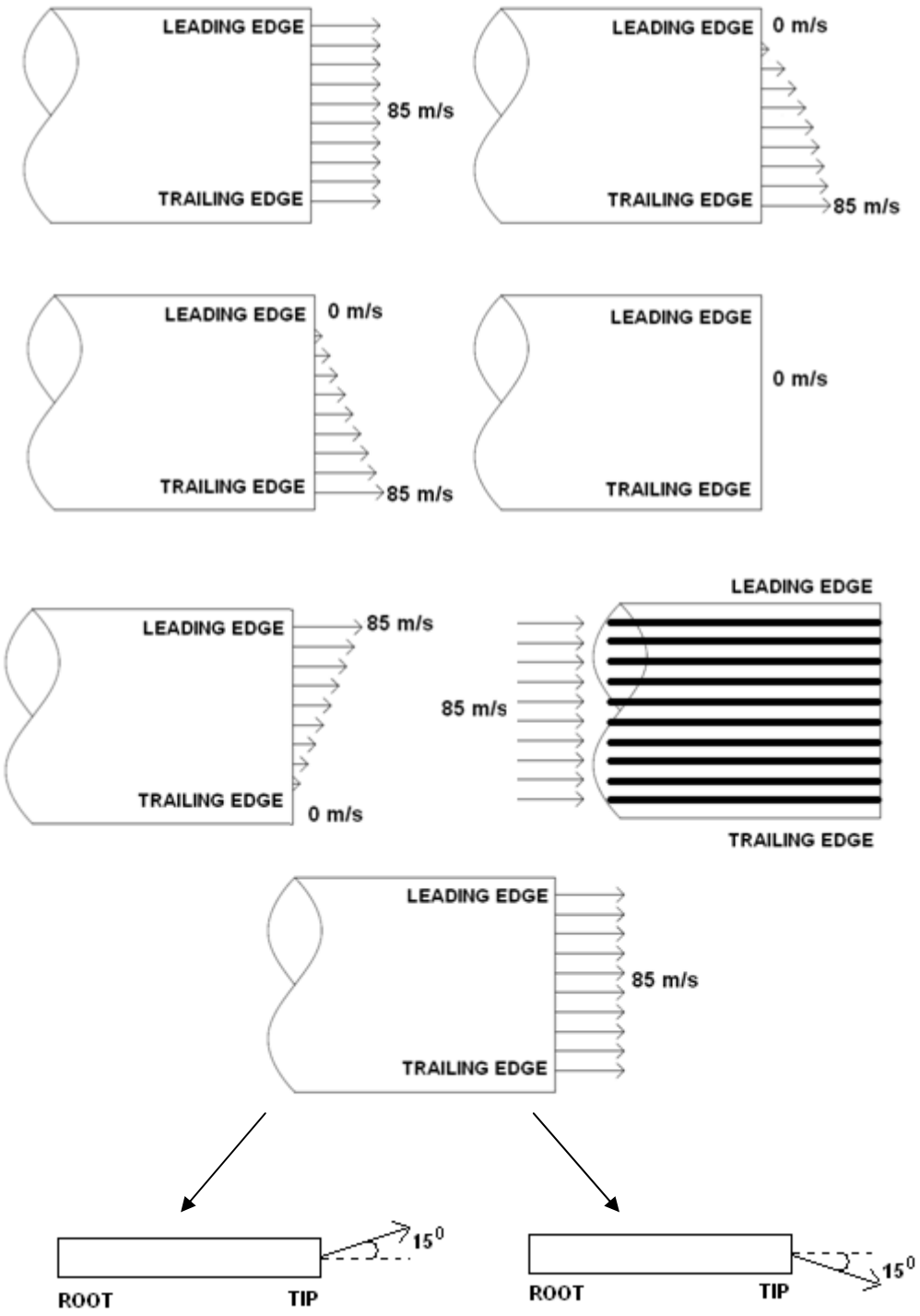

Figure 2.17: Injection Scenarios: first row from left to right: uniform injection, sinus waveform injection, second row from left to right: triangular waveform injection and no injection, third row from left to right: inverse triangular waveform injection, uniform injection with fully developed tube flow (FDF), fourth row from left to right: positive angled uniform injection, negative angled uniform injection.

CHAPTER 3

RESULTS & DISCUSSIONS

Solutions were prepared for three different angle of attack configurations and for 3 different injection cases as well as 5 additional cases for 8° angle of attack case, which are:

- 4° angle of attack configuration:
  - No injection
  - Uniform injection,
  - Triangular waveform injection,
- 8° angle of attack configuration,
  - No injection
  - Uniform injection,
  - Triangular waveform injection,
  - Sinusoidal waveform injection,
  - Inverse triangular waveform injection,
  - +15° angled uniform injection,
  - -15° angled uniform injection,
  - Uniform injection with fully developed flow,
- 12° angle of attack configuration,
  - No injection
  - Uniform injection,
  - Triangular waveform injection.

After the outputs were obtained, a parametric comparison between aerodynamic variables was conducted. Results were generated by comparing dimensionless parameters, velocity values, U (x-direction), V (y-direction) and W (z-direction) (figure 3.1) as well as turbulent kinetic energy, vorticity magnitude and pressure coefficient. Lift and drag values (both forces and coefficients) with respect to angles of attack for each case is presented, as well.

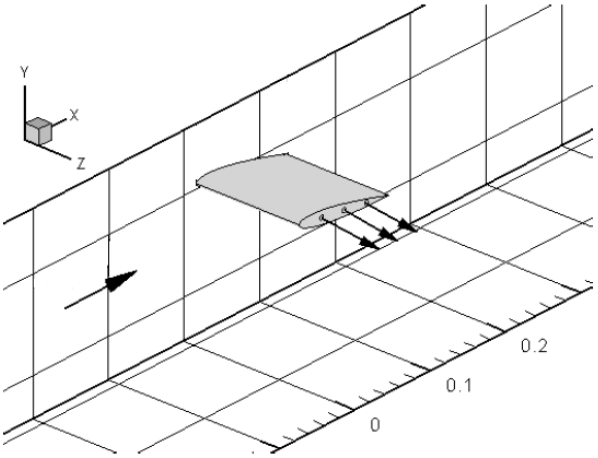

Figure 3.1: Directional definitions, airflow is in +x direction, jet injection is in +z axis

3.1 Definition of the outputs:

There are 4 specific planar stations where the outputs were plotted that are; 0.5 chord, mid chord location of the wing, where the aerodynamics forces on the wing can clearly be seen; 1 chord, which denotes the location of the trailing edge, where the separation characteristics can be observed; 2 chords, the same station were the experimental data were collected and finally 3 chords, an appropriate station to investigate wake flow (figure 3.2).

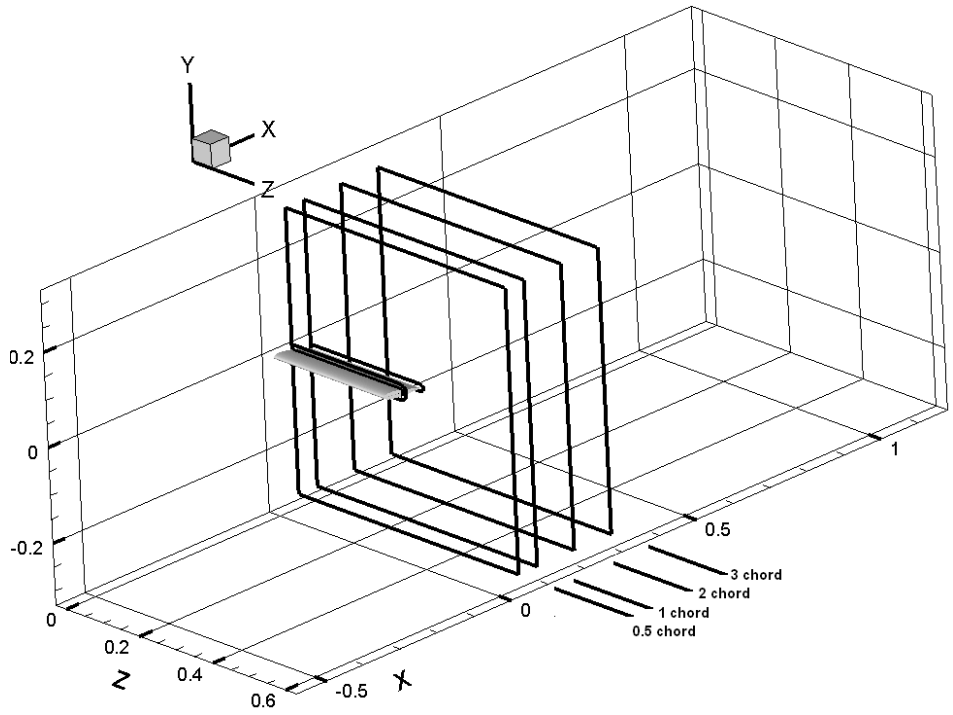

Figure 3.2: Output stations on the domain

Outputs were compared by means of variables that basically define vortex formation, shape and vortex core location on the domain. Velocity parameters that are in all three axes and turbulent kinetic energy were non-dimensionalized with respect to freestream velocity that is 10 *m/s*. Vorticity magnitude and pressure coefficient variables are formulated below.

$$U_N = \frac{U}{U_\infty} \ , V_N = \frac{V}{U_\infty} \ , W_N = \frac{W}{U_\infty}$$

Where U_∞ is the freestream velocity, where subscript N denotes non-dimensional variable.

$$TKE = k = \frac{1}{2}\left(\overline{(u')^2} + \overline{(v')^2} + \overline{(w')^2}\right)$$

$$k_N = \frac{k}{U_\infty^2}$$

Where prime variables are fluctuating velocity components, as Reynolds decomposition suggests. Vorticity magnitude parameter was defined using all three velocity components by simply computing the curl of velocity and taking the magnitude of the vector, resulting equation is as follows. While computing pressure coefficient, considering the pressure of the domain was defined as gauge pressure, total pressure output was directly divided to dynamic pressure.

$$Vorticity\ Magnitude = \sqrt{\left(\frac{\partial w}{\partial y} - \frac{\partial v}{\partial z}\right)^2 + \left(\frac{\partial u}{\partial z} - \frac{\partial w}{\partial x}\right)^2 + \left(\frac{\partial v}{\partial x} - \frac{\partial u}{\partial y}\right)^2}$$

$$C_P = \frac{P - P_\infty}{\frac{1}{2}\rho_\infty V_\infty^2}$$

Post-processing was conducted by using Tecplot. Contours of aforementioned variables are presented with respect to the observer that is looking from the exit section of the wind tunnel. Non-dimensional U, V, W velocities, turbulent kinetic energy, vorticity magnitude and pressure coefficient contour were plotted, respectively.

3.2 Computational Outputs

Results are plotted at x= 0.5 c (mid chord), x= 1.0 c (trailing edge), x= 2.0 c and x= 3.0 c stations. Entire wind tunnel section is shown at the plots and observer is looking from the exit of the wind tunnel. Data order is as follows: injection cases for 4° are followed by 8° angle of attack configuration and finally 12° angle of attack scenarios at the very end of corresponding section.

3.2.1 Dimensionless U-velocity

At x= 1.0 c station (2nd row figures, figure 3.4) for 4° angle of attack cases, vortex centers are quite close to each other for uniform injection and triangular waveform injection cases while flow is leaving the wing surfaces smoothly in no injection case with no trail of high spinning characteristics. High velocity zone of uniform injection case is stronger than it is in triangular waveform case considering the change in the jet momentum coefficient. There are two positive velocity fields prominent at wake region, surrounding the negative velocity field. Considering the strength of the tip injection, injections seem to, literally, “cut” the tip flow into two, constituting two vortex patterns. That strange phenomenon was investigated thoroughly by drawing the streamlines on one of the contours in order to decide whether there’s a secondary counter rotating vortex or not (figure 3.3).

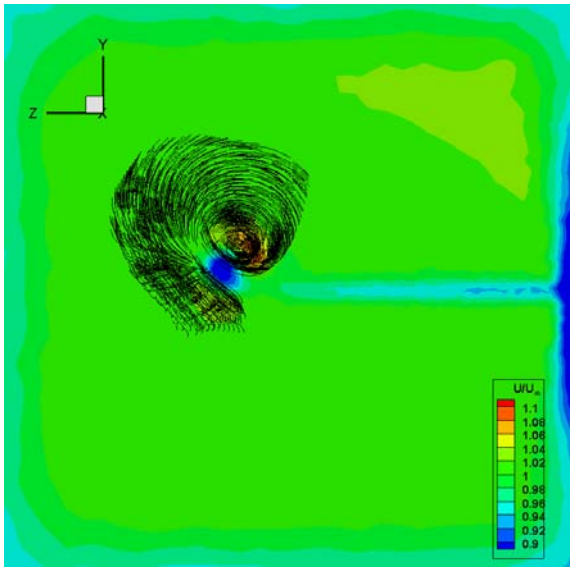

Figure 3.3: Streamlines, dimensionless U velocity, 4 angle of attack case with uniform injection at station x= 2 c

The secondary high velocity field turned out to be a zone created by the injection itself. Injected flow bends the tip vortex form the middle and forms a croissant shaped flux, which finally makes a single vortex pattern.

For the same cases and the same stations at 8° angle of attack scenarios, separations are larger and vortices are stronger than 4° angle of attack case (figure 3.5, 3.6, 3.7). Vortex dissipation in the wake is lower due to higher turbulence intensity; yet again corresponding cases at both 4° and 8° angle of attack configurations showed similar characteristics. Sinusoidal waveform injection, which is one of the additional cases, has a slightly higher C_μ value than triangular injection case; therefore turbulent behavior of the tip flow is higher than in triangular injection case. Inverse triangular injection, on the other hand, made the slightest change compared to other injection types by means of vortex formation. As expected, case where fully developed flow is included to uniform injection is almost the same with the case without tubular flow. Further discussion about the difference between two cases are presented at following graphs, in terms of location of the vortex core, lift and drag coefficient values. Vortex formation at the cases with +15° and -15° angled uniform injection differs in strength and core location; not surprisingly, injection with positive inclination throws the vortex further and higher, however in -15° angled case velocity gradients are larger at the core, vortex is visible with high core strength even at x= 0.3 c station. Separation increases and vortex size enlarges at cases with 12° angle of attack configuration (figure 3.8). Moreover, flow disturbance in root section is apparent, due to large angle of attack. Compared to 4° and 8° angle of attack cases, low pressure characteristics at triangular injection is clearly more dominant than at uniform injection case, this time. This change is probably due to the loss of integrity in injection, especially for uniform injection case. Vortices do not dissipate easily, proving that turbulence level is increased in tip flow.

Secondly, in order to visualize the effect of the injection on the wake flow, dimensionless U velocity distribution at x=2c station, at the tip plane were presented (figure 3.9, 3.10). On both of the figures, injection cases with same momentum coefficient value were compared. On the figure with lower cμ, i.e figure 3.9, lower velocity zone of triangular waveform case has elevated in +y axis, while U velocity that belongs to inverse triangular waveform case has shown unexpected behavior. Sudden increase in the velocity at the wake is mainly due to the fact that tip injection is inversed, however further consideration is essential on that particular case. Moreover, on figure 3.10, the change in the injection angle basically creates high velocity zones at different +y values (maxima), as well as changing the location of the low velocity zones accordingly (minima).

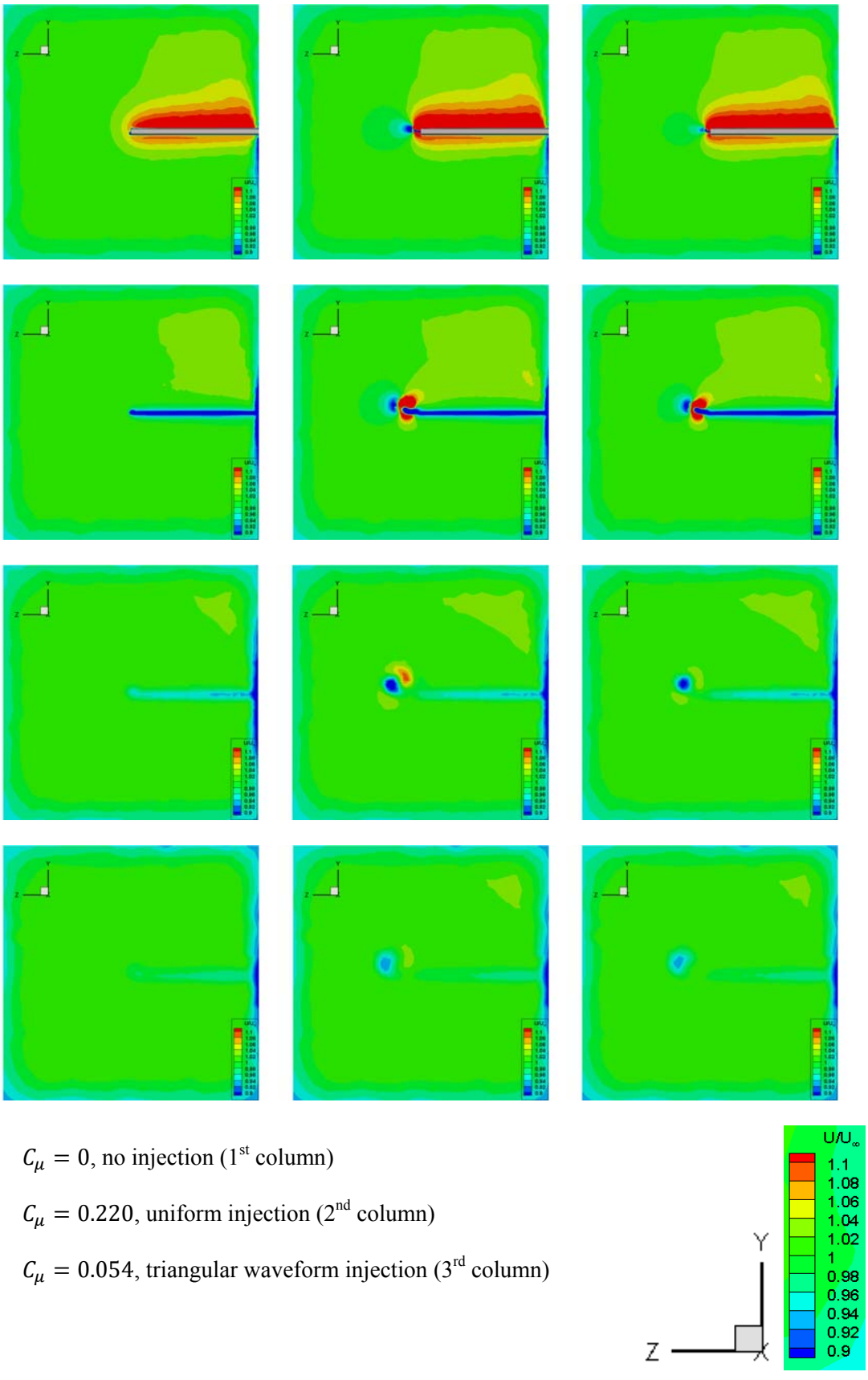

Figure 3.4: Dimensionless U velocities for no injection (left column), uniform injection (middle column) and triangular waveform injection (right column) cases at 4° angle of attack of 4 different stations starting from leading edge, which are located at 0.5 chord (1st row), 1 chord (2nd row), 2 chord (3rd row), 3 chord (4th row), back view.

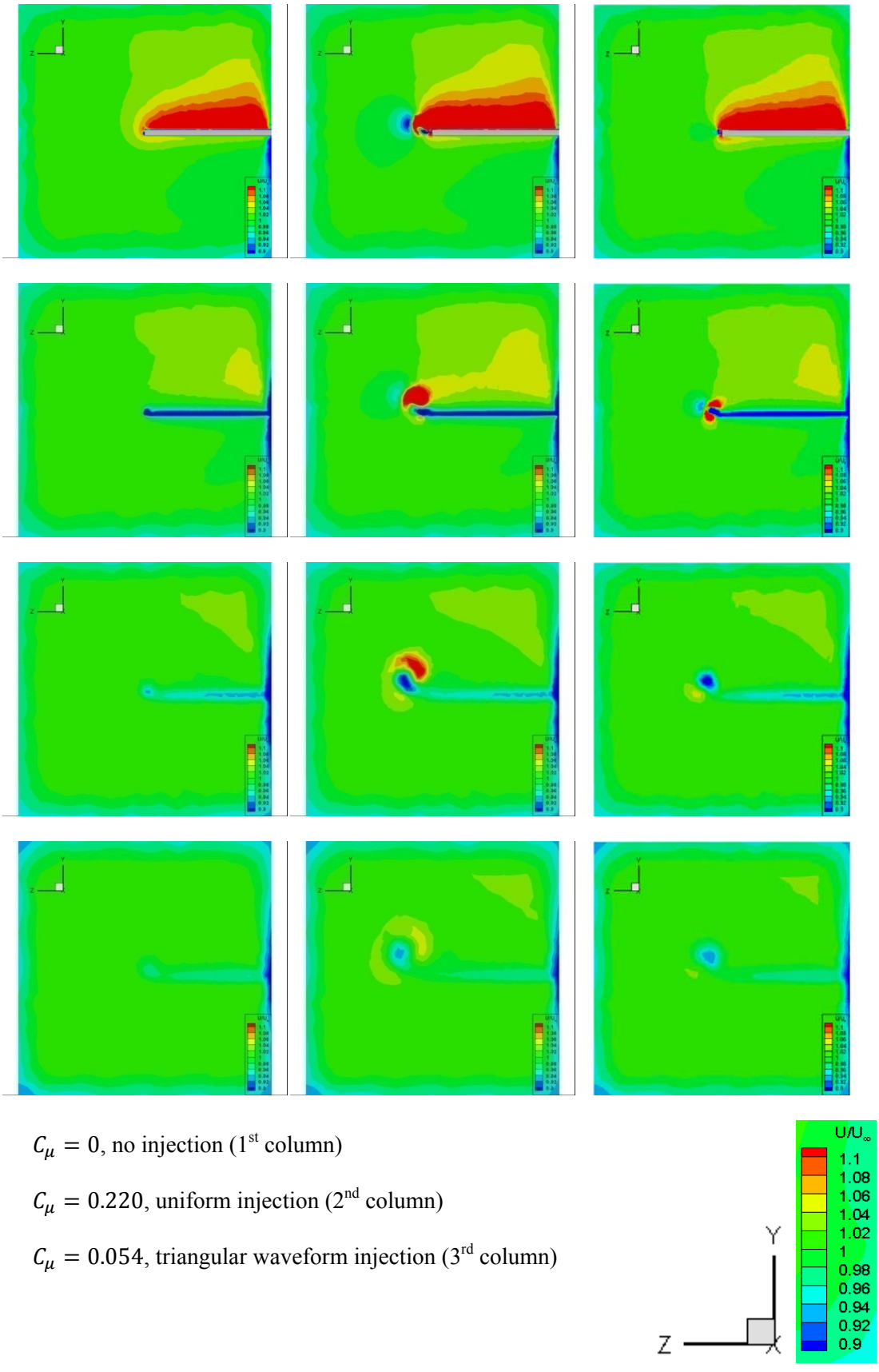

Figure 3.5: Dimensionless U velocities for no injection (left column), uniform injection (middle column) and triangular waveform injection (right column) cases at 8° angle of attack of 4 different stations starting from leading edge, which are located at 0.5 chord (1st row), 1 chord (2nd row), 2 chord (3rd row), 3 chord (4th row).

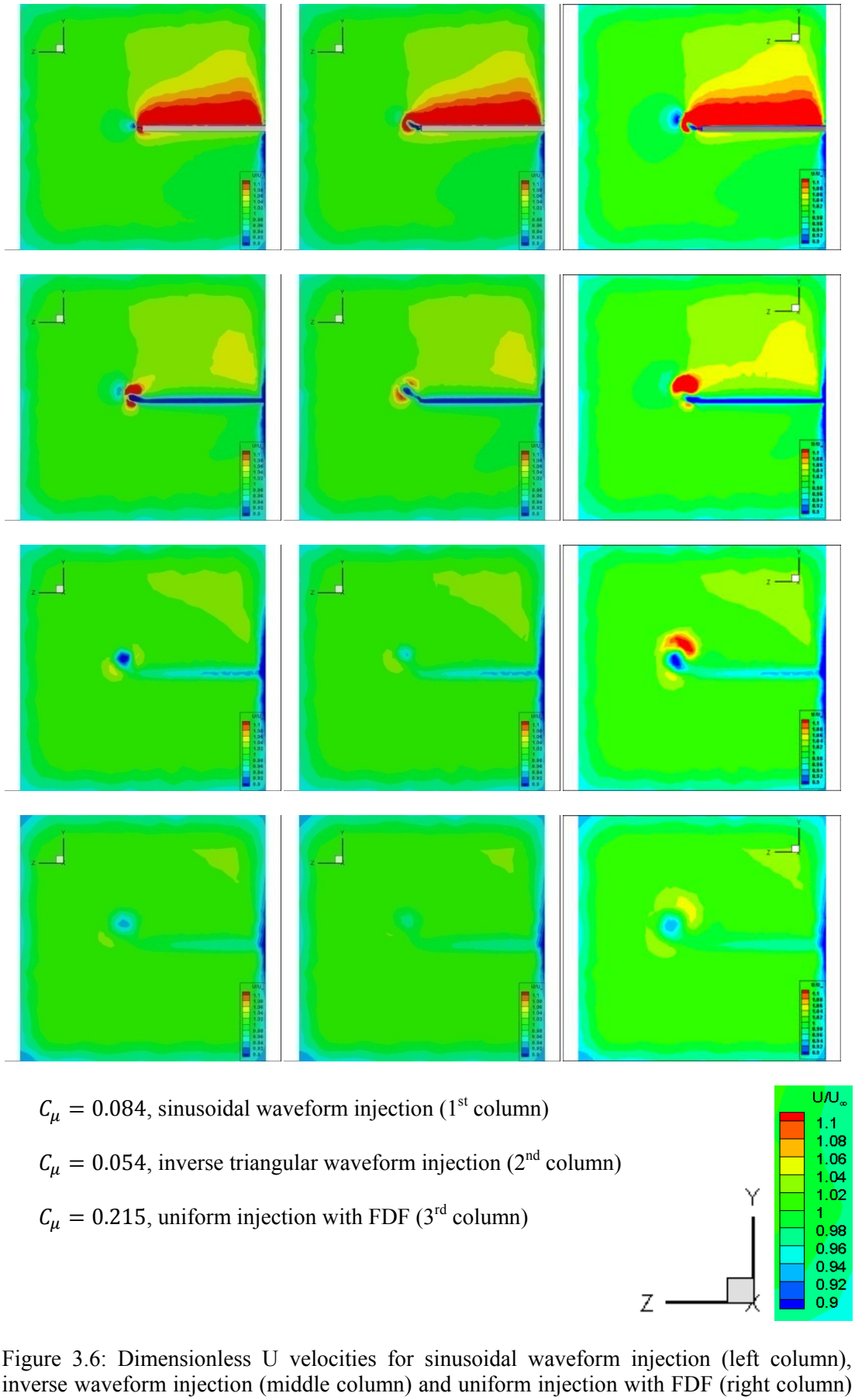

Figure 3.6: Dimensionless U velocities for sinusoidal waveform injection (left column), inverse waveform injection (middle column) and uniform injection with FDF (right column) cases at 8° angle of attack of 4 different stations starting from leading edge, which are located at 0.5 chord (1st row), 1 chord (2nd row), 2 chord (3rd row), 3 chord (4th row).

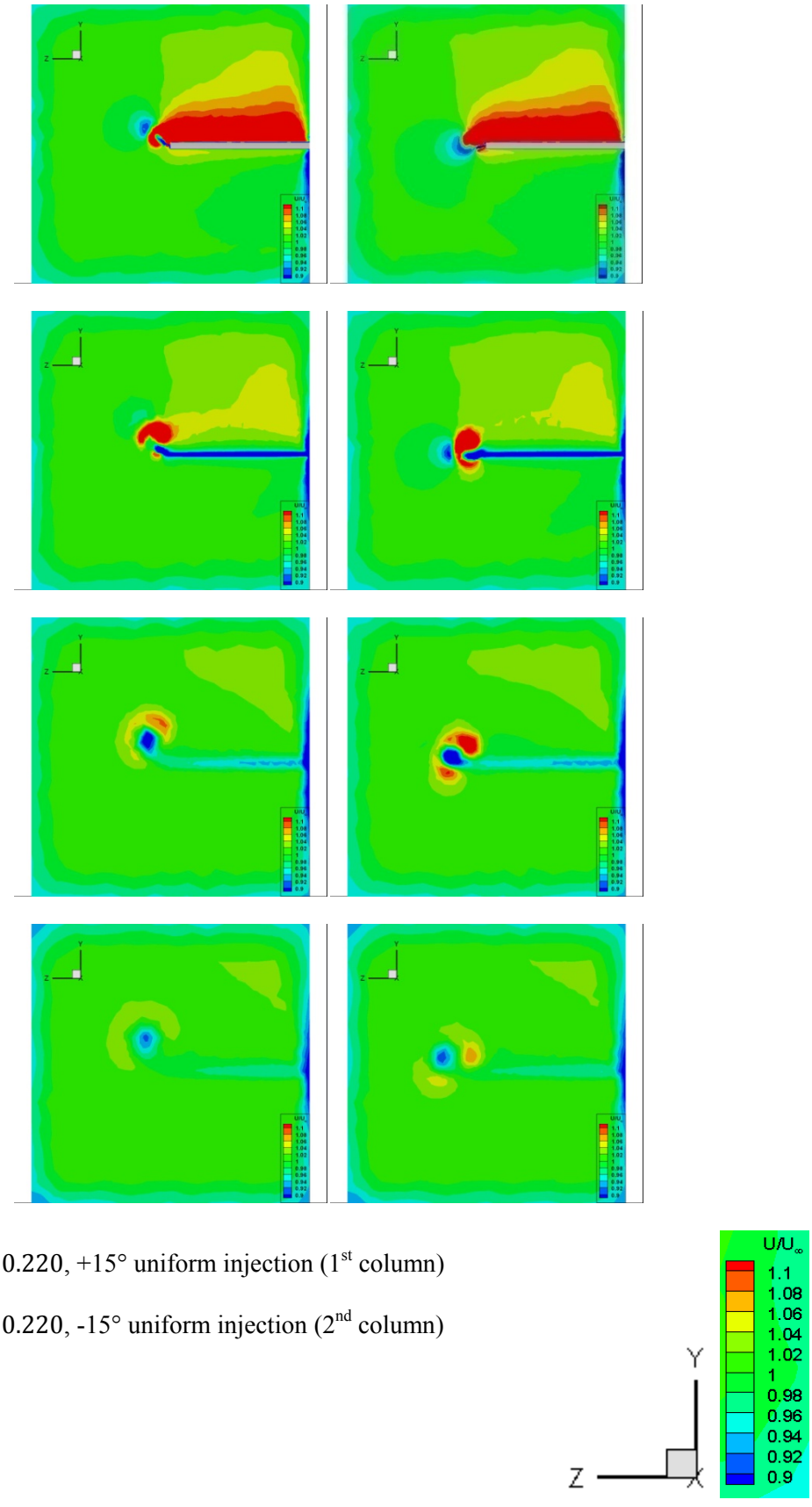

Figure 3.7: Dimensionless U velocities for +15° uniform injection (left column) and -15° uniform injection (right column) cases at 8° angle of attack of 4 different stations starting from leading edge, which are located at 0.5 chord (1st row), 1 chord (2nd row), 2 chord (3rd row), 3 chord (4th row).

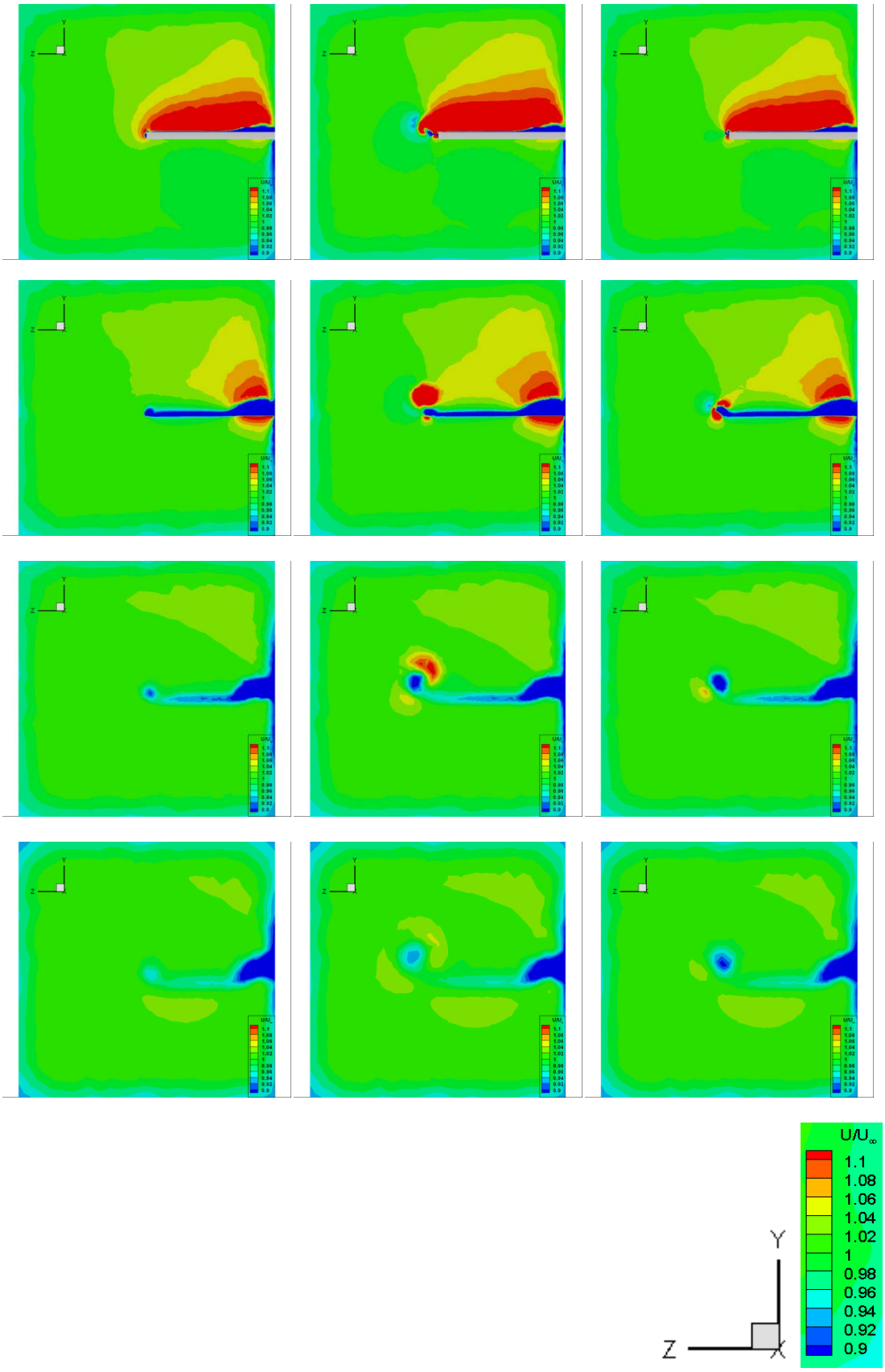

Figure 3.8: Dimensionless U velocities for no injection (left column), uniform injection (middle column) and triangular waveform injection (right column) cases at 12° angle of attack of 4 different stations starting from leading edge, which are located at 0.5 chord (1st row), 1 chord (2nd row), 2 chord (3rd row), 3 chord (4th row).

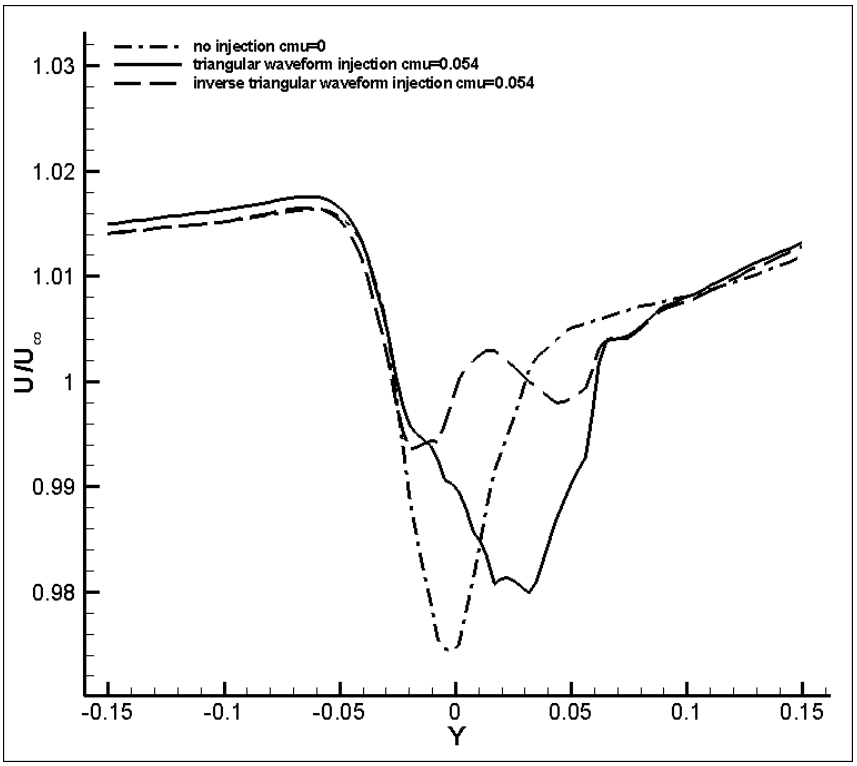

Figure 3.9: comparison of dimensionless U velocity distribution for cμ=0.054, at x=2c station, on the tip plane

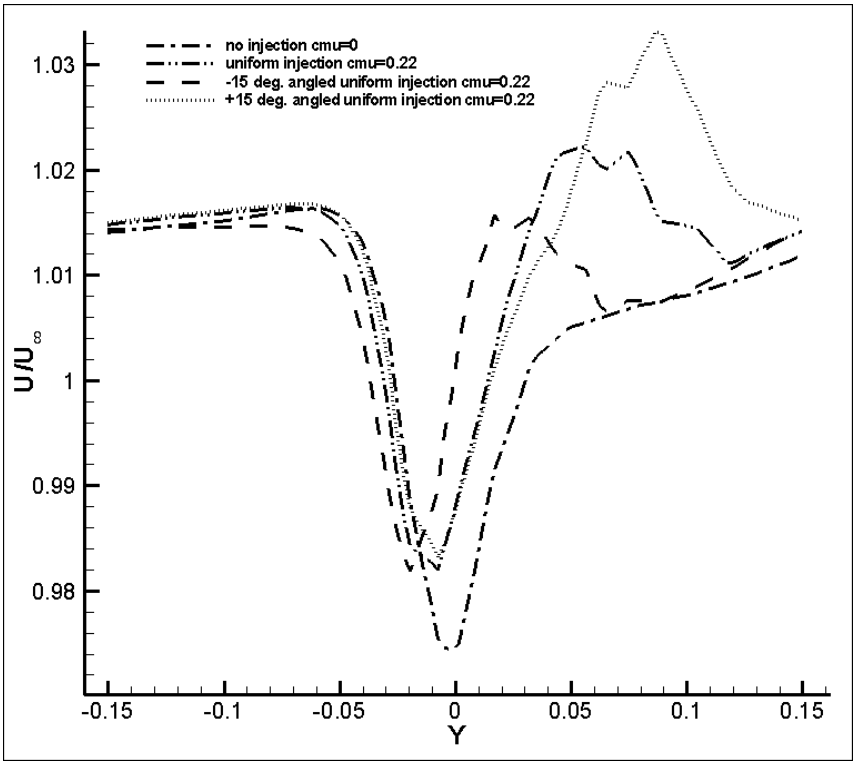

Figure 3.10: comparison of dimensionless U velocity distribution for cμ=0.22, at x=2c station, on the tip plane

3.2.2 Dimensionless V-velocity

Change in the y-direction velocity shows the upwash behavior in the tip, clearly. At 4° angle of attack cases, uniform injection still has the largest velocity gradients and furthermore, two high velocity fields are apparent (figure 3.11). Upper one, which can be identified as the aforementioned vortex pattern, is larger than the secondary field, where there is no rotational behavior, at sections x= 0.5c, x= 1.0c and x=2.0c; however as in triangular injection case at station x= 0.3 c, sizes are equal. Due to the injection, a secondary downwash pattern is observed at the left of positive velocity region, as shown in the U-velocity contours.

As the angle of attack is set to 8° (figure 3.12, 3.13, 3.14), positive velocity field tend to strengthen, yet secondary negative field dissipates in the wake more easily. This difference can be investigated by comparing +15 and -15 angled uniform injection cases as well as 12° angle of attack cases (figure 3.15). It's obvious that as the separation becomes larger, secondary negative flow field tends to vanish.

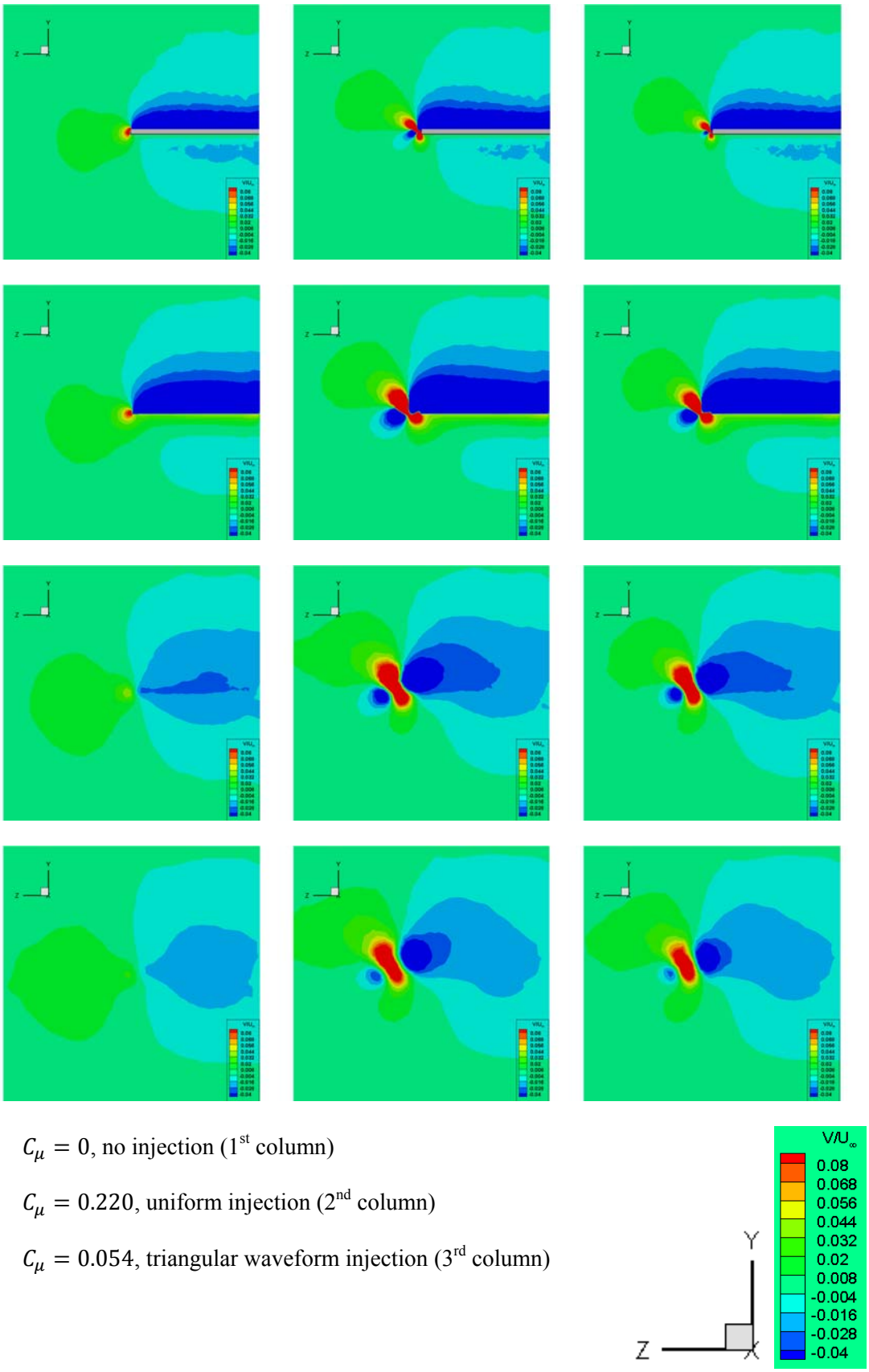

Figure 3.11: Dimensionless V velocities for no injection (left column), uniform injection (middle column) and triangular waveform injection (right column) cases at 4° angle of attack of 4 different stations starting from leading edge, which are located at 0.5 chord (1st row), 1 chord (2nd row), 2 chord (3rd row), 3 chord (4th row).

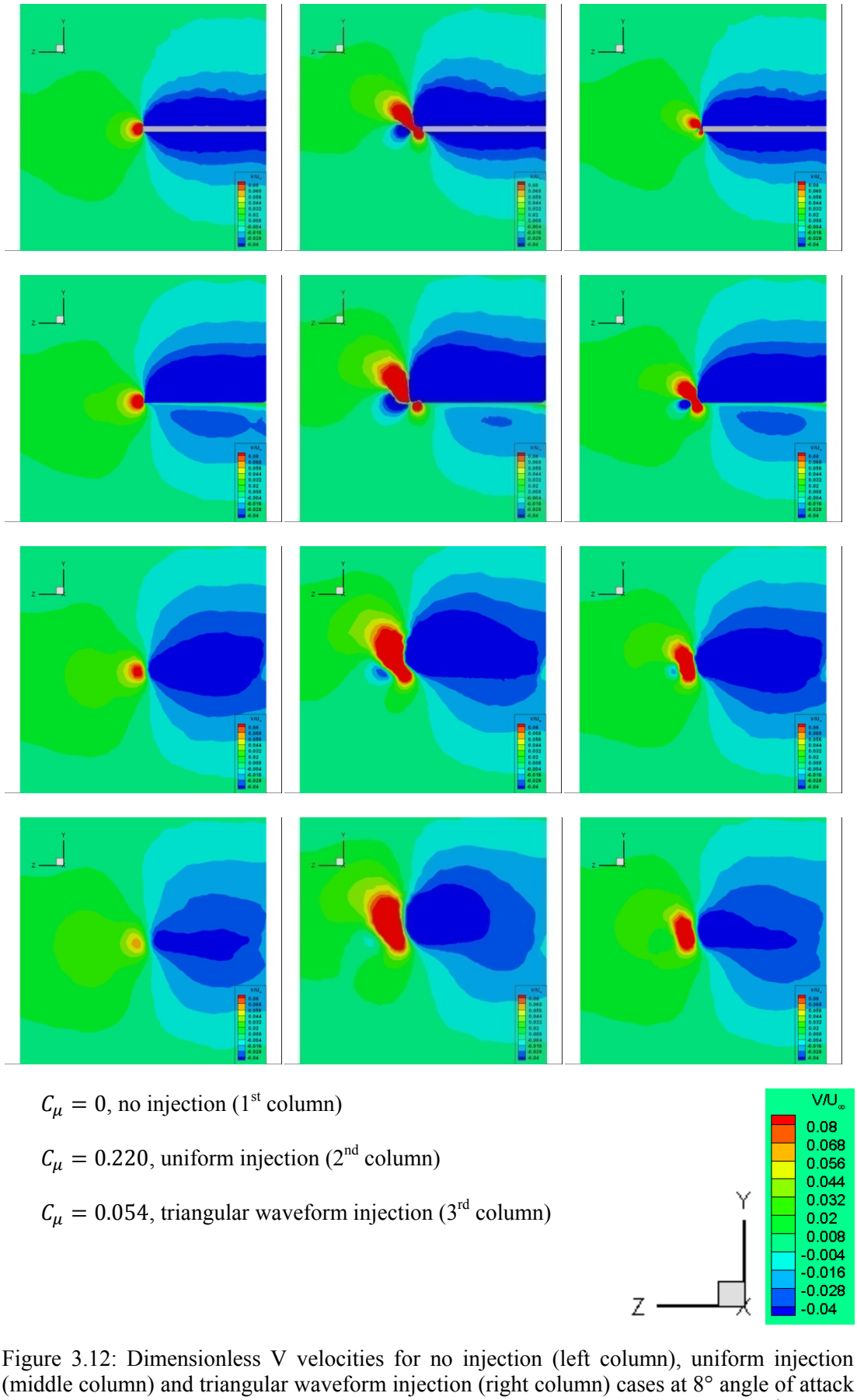

Figure 3.12: Dimensionless V velocities for no injection (left column), uniform injection (middle column) and triangular waveform injection (right column) cases at 8° angle of attack of 4 different stations starting from leading edge, which are located at 0.5 chord (1st row), 1 chord (2nd row), 2 chord (3rd row), 3 chord (4th row).

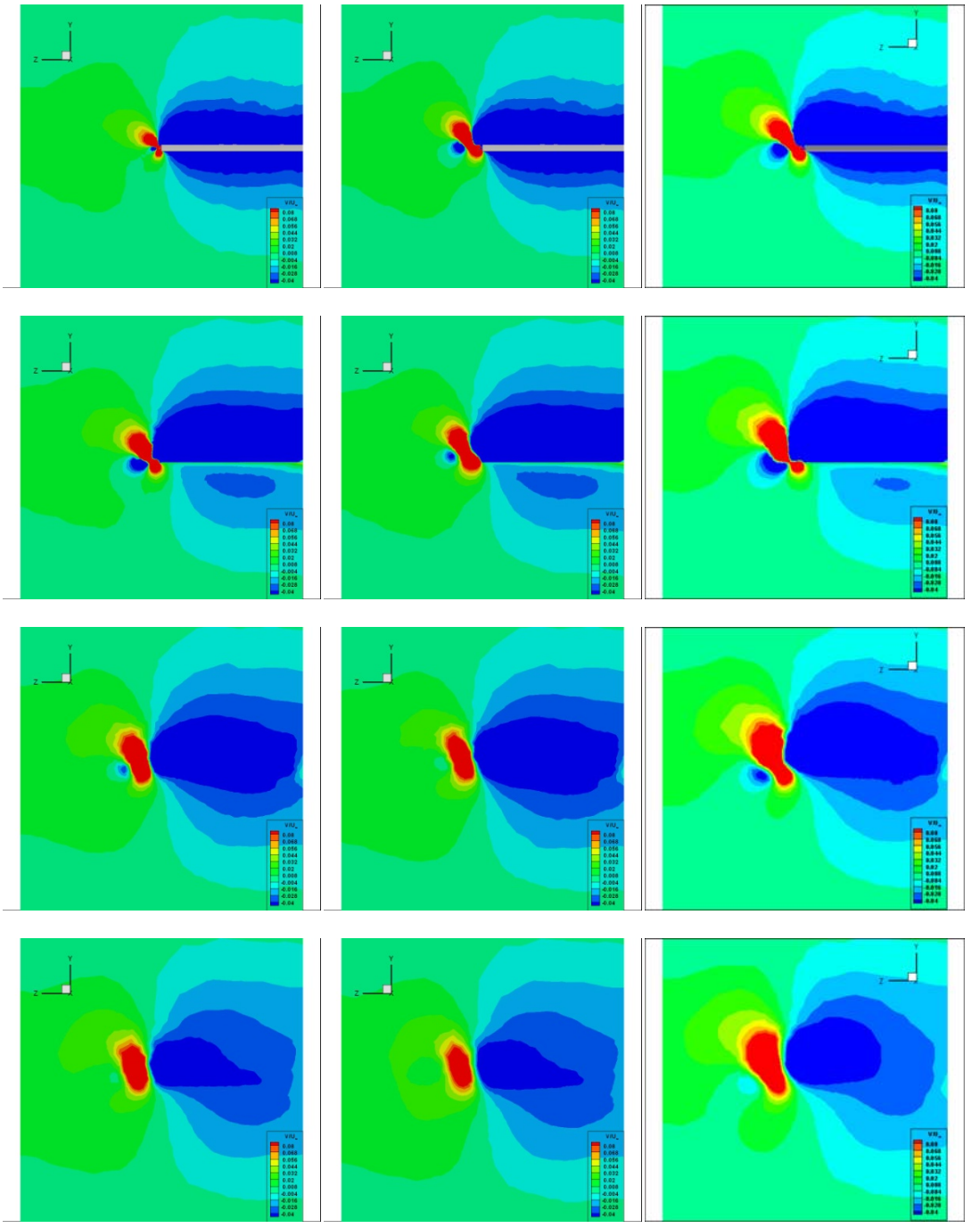

Figure 3.13: Dimensionless V velocities for sinusoidal waveform injection (left column), inverse waveform injection (middle column) and uniform injection with FDF (right column) cases at 8° angle of attack of 4 different stations starting from leading edge, which are located at 0.5 chord (1st row), 1 chord (2nd row), 2 chord (3rd row), 3 chord (4th row).

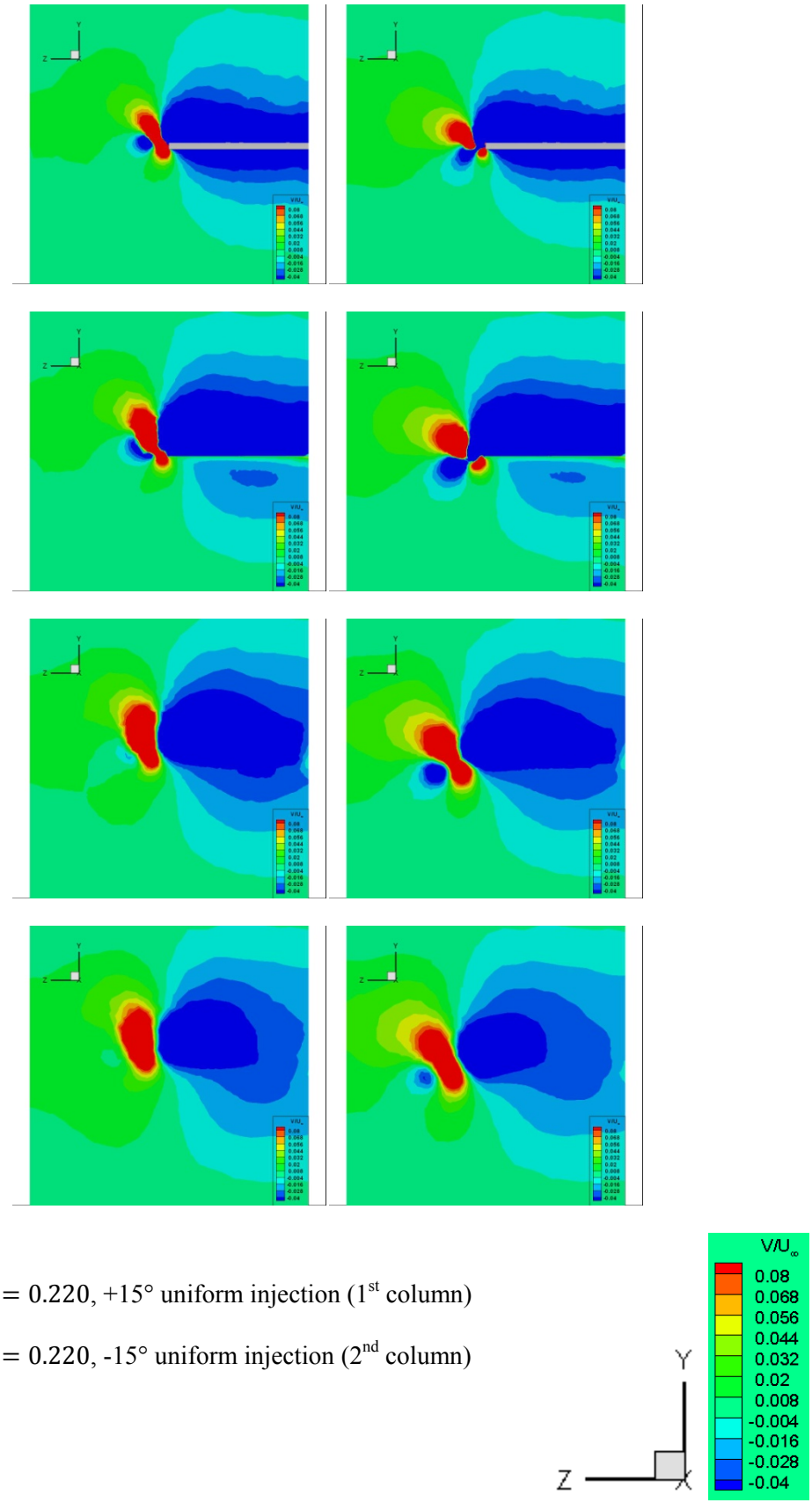

Figure 3.14: Dimensionless V velocities for +15° uniform injection (left column) and -15° uniform injection (right column) cases at 8° angle of attack of 4 different stations starting from leading edge, which are located at 0.5 chord (1st row), 1 chord (2nd row), 2 chord (3rd row), 3 chord (4th row).

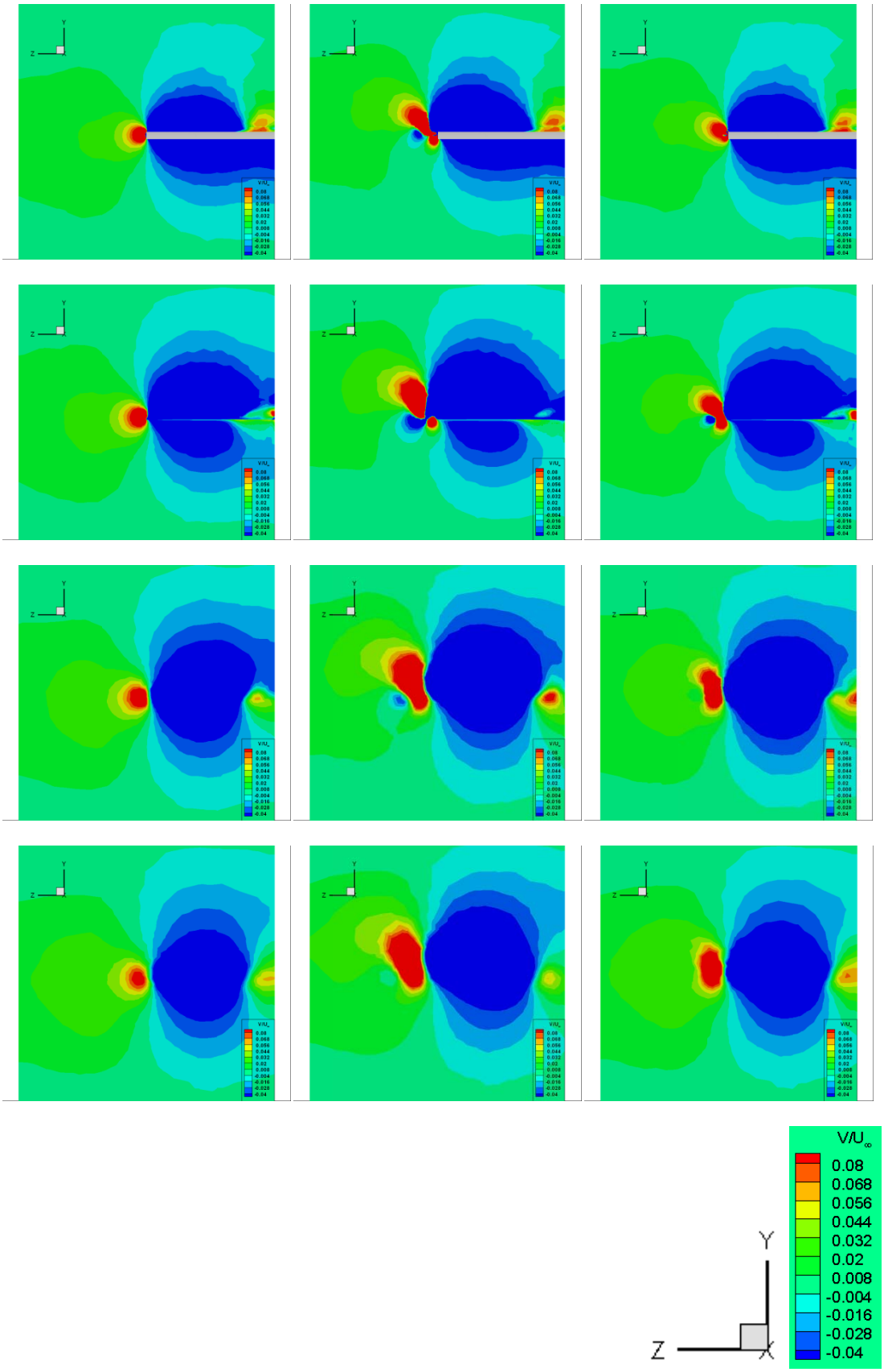

Figure 3.15: Dimensionless V velocities for no injection (left column), uniform injection (middle column) and triangular waveform injection (right column) cases at 12° angle of attack of 4 different stations starting from leading edge, which are located at 0.5 chord (1st row), 1 chord (2nd row), 2 chord (3rd row), 3 chord (4th row).

3.2.3 Dimensionless W-velocity

These contours contain the same directional velocity components with injection velocity. At no injection cases (regardless of the angle of attack), at the tip, leakage from pressure side to suction side is plotted. Yet again for cases with injection, a weaker secondary negative field exists. Injection strength is the largest with uniform injection and the largest negative velocities are seen on the uniform injection cases. Especially at station x= 1.0 c, high positive velocity flow at the pressure side which tend to flee to suction side is apparent; however, injection prevents this escape, creating a larger vortex pattern in a zone that further and higher from the tip. As the angle of attack gets larger, inherently, separation and turbulence intensity increases. At 8° angle of attack cases (figure 3.17, 3.18, 3.19), triangular waveform injection type seems insufficient in increasing the effective wing area. Sinusoidal and inverse triangular injections show better performance in terms of detaching the negative flow field at the tip; moreover +15° angled injection is more successful than -15° angled uniform injection scenario in moving the vortices away from the tip. At 12° angle of attack cases (figure 3.20), high velocity fields are apparent both at the tip and root. Strength of the secondary negative velocity field decreases compared to lower angle of attack cases, at downstream sections.

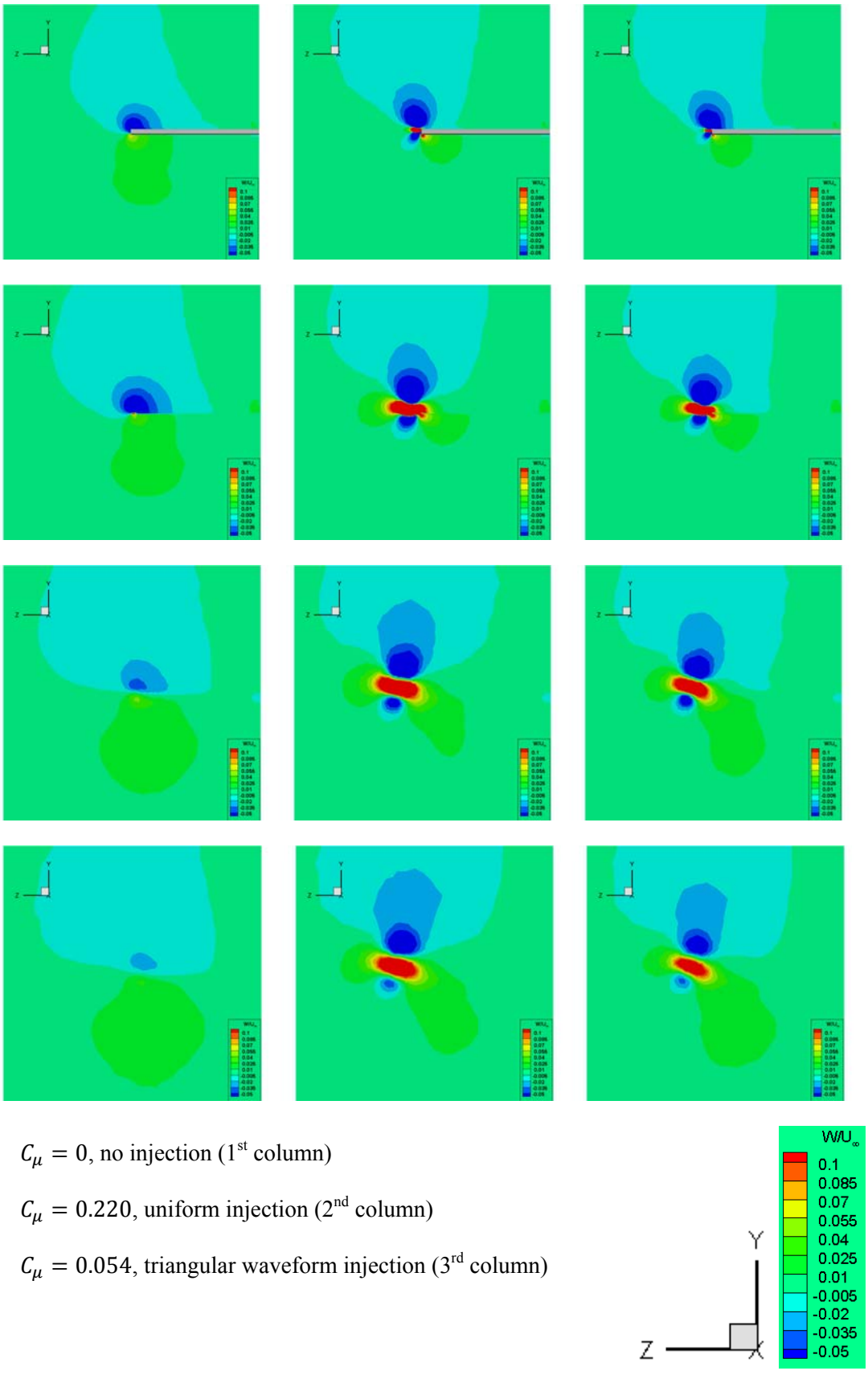

Figure 3.16: Dimensionless W velocities for no injection (left column), uniform injection (middle column) and triangular waveform injection (right column) cases at 4° angle of attack of 4 different stations starting from leading edge, which are located at 0.5 chord (1st row), 1 chord (2nd row), 2 chord (3rd row), 3 chord (4th row).

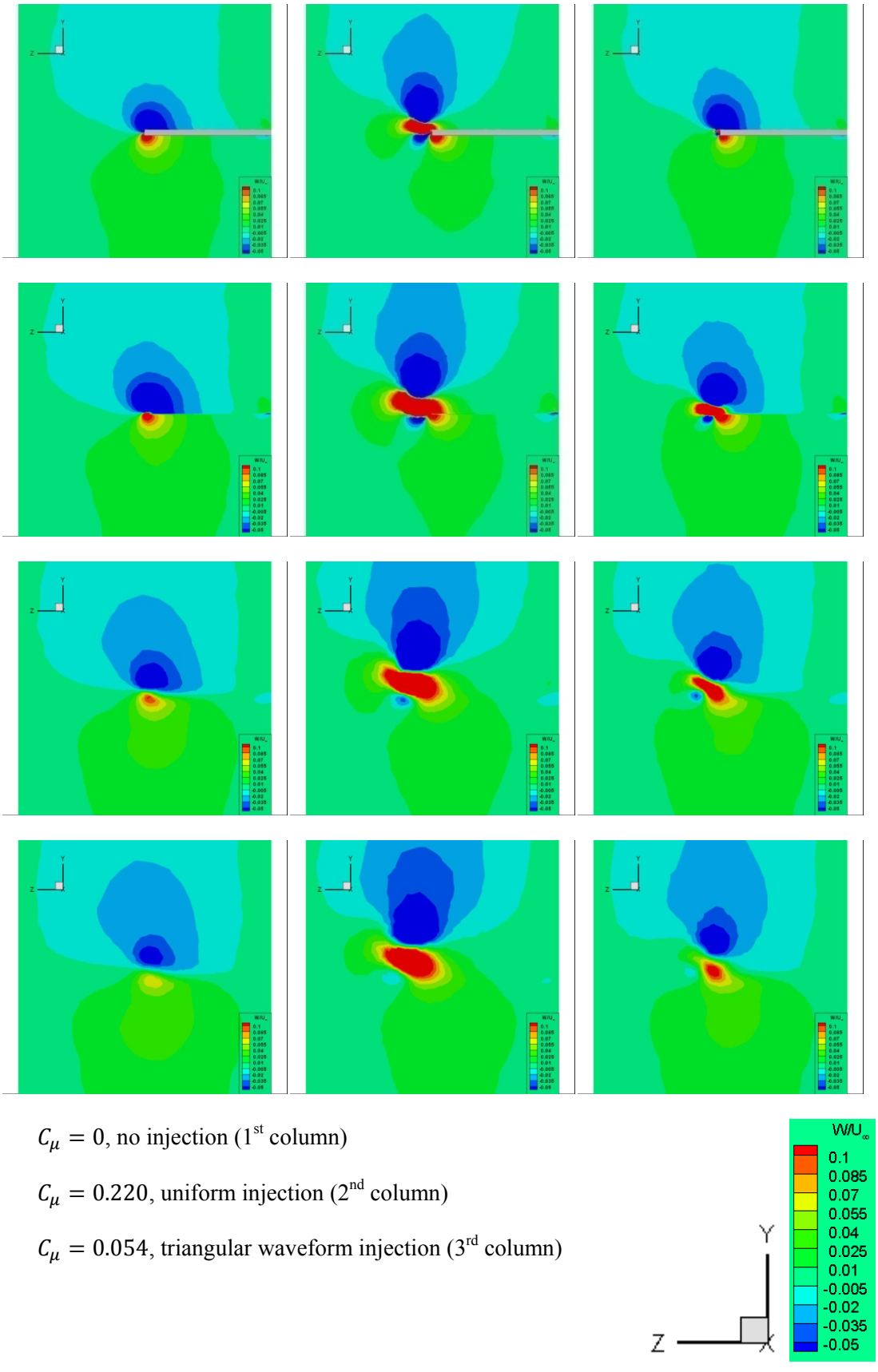

$C_\mu = 0$, no injection (1st column)

$C_\mu = 0.220$, uniform injection (2nd column)

$C_\mu = 0.054$, triangular waveform injection (3rd column)

Figure 3.17: Dimensionless W velocities for no injection (left column), uniform injection (middle column) and triangular waveform injection (right column) cases at 8° angle of attack of 4 different stations starting from leading edge, which are located at 0.5 chord (1st row), 1 chord (2nd row), 2 chord (3rd row), 3 chord (4th row).

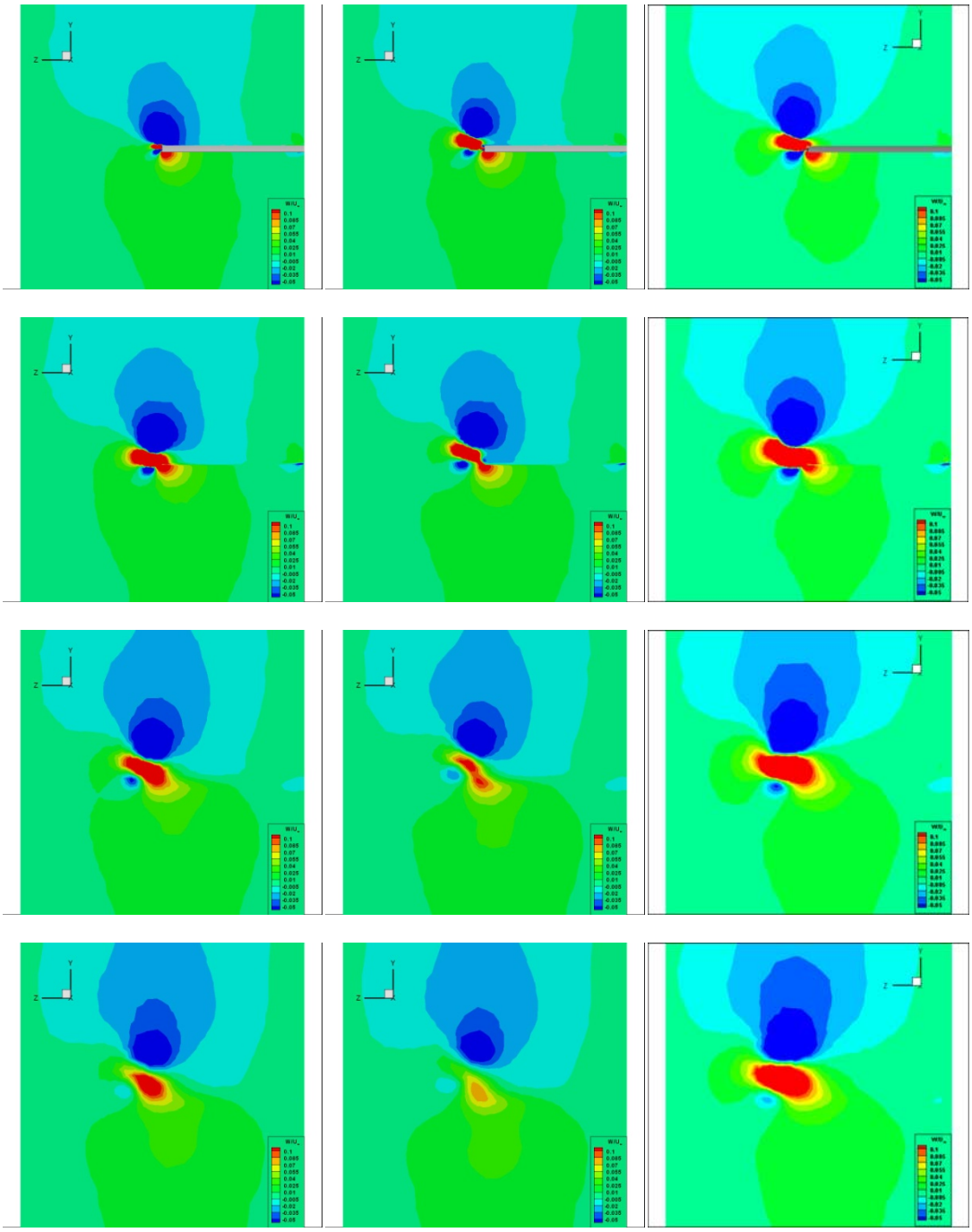

Figure 3.18: Dimensionless W velocities for sinusoidal waveform injection (left column), inverse waveform injection (middle column) and uniform injection with FDF (right column) cases at 8° angle of attack of 4 different stations starting from leading edge, which are located at 0.5 chord (1st row), 1 chord (2nd row), 2 chord (3rd row), 3 chord (4th row).

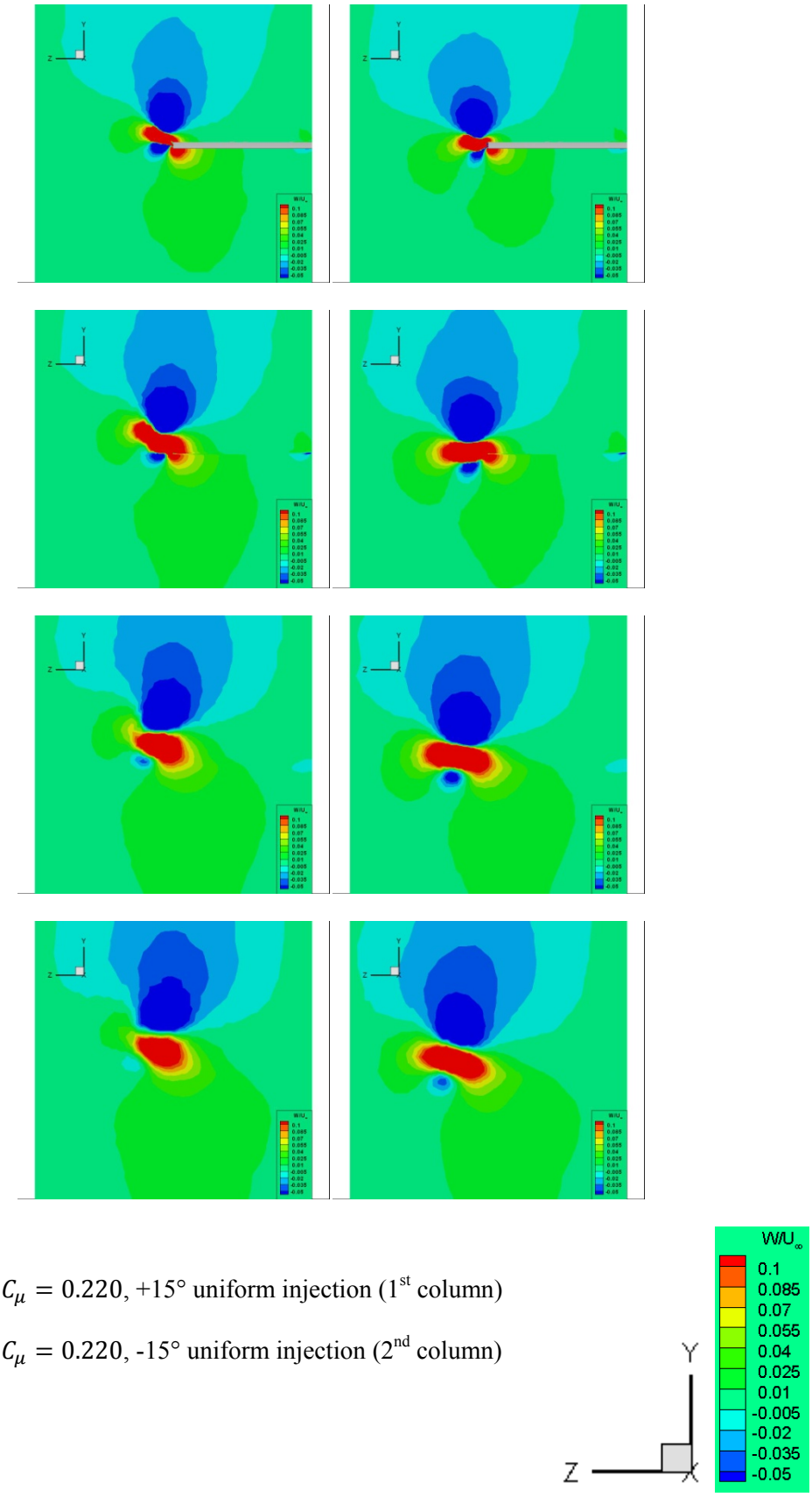

Figure 3.19: Dimensionless W velocities for +15° uniform injection (left column) and -15° uniform injection (right column) cases at 8° angle of attack of 4 different stations starting from leading edge, which are located at 0.5 chord (1st row), 1 chord (2nd row), 2 chord (3rd row), 3 chord (4th row).

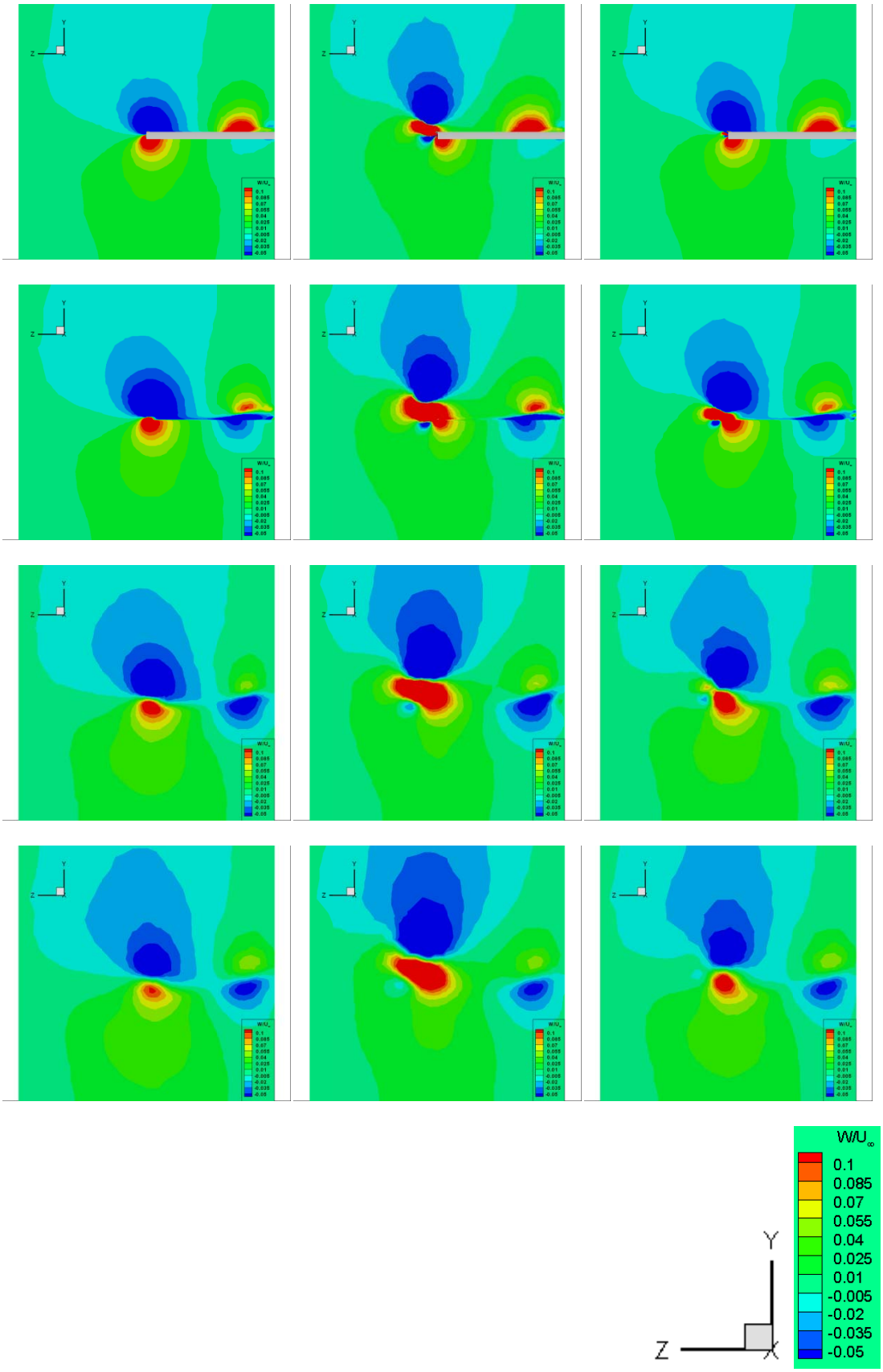

Figure 3.20: Dimensionless W velocities for no injection (left column), uniform injection (middle column) and triangular waveform injection (right column) cases at 12° angle of attack of 4 different stations starting from leading edge, which are located at 0.5 chord (1st row), 1 chord (2nd row), 2 chord (3rd row), 3 chord (4th row).

3.2.4 Dimensionless Turbulent Kinetic Energy (k):

Turbulent kinetic energy basically consists of the total kinetic energy of fluctuating velocity components. It is a good practice to plot turbulent kinetic energy as it shows zones with high turbulence intensity in the domain. Cases with no injection has low level of turbulence compared to cases with injection and it's even not visible on the plots considering the range and level of the variable is the same for all. On the figure 3.21 below, range is rearranged for a no injection case in order to observe the tip leakage.

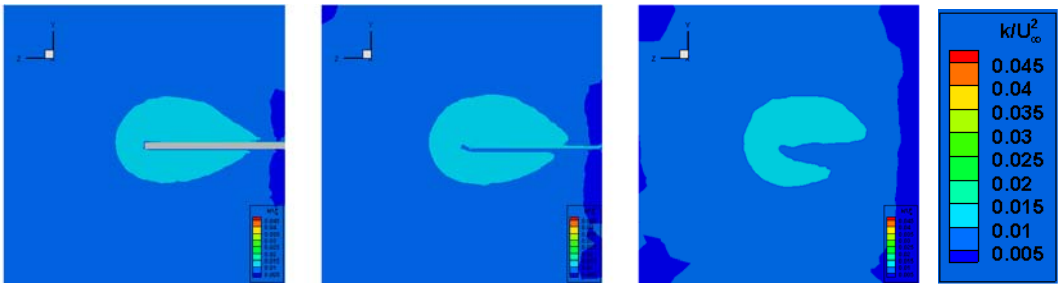

Figure 3.21: Dimensionless turbulence kinetic energy for no injection case at 8° angle of attack of 3 different stations starting from leading edge, which are located at 0.5 chord (left), 1 chord (middle), 2 chord (right).

Zones with highly turbulent flow are mostly due to the injection considering the high velocity. Comparing all the cases with each other, uniform injection creates the largest turbulent zone at the tip and wake region (figure 3.22, 3.23, 3.24, 3.25). Moreover, flow with high energy tends to ascend, forming a candle-light-like high energy contour. This is due to the tendency of the tip flow to bend and move from pressure side to suction side. A dramatic increase in the turbulent kinetic energy is seen at 12° angle of attack cases (figure 3.26) at the root section, as well.

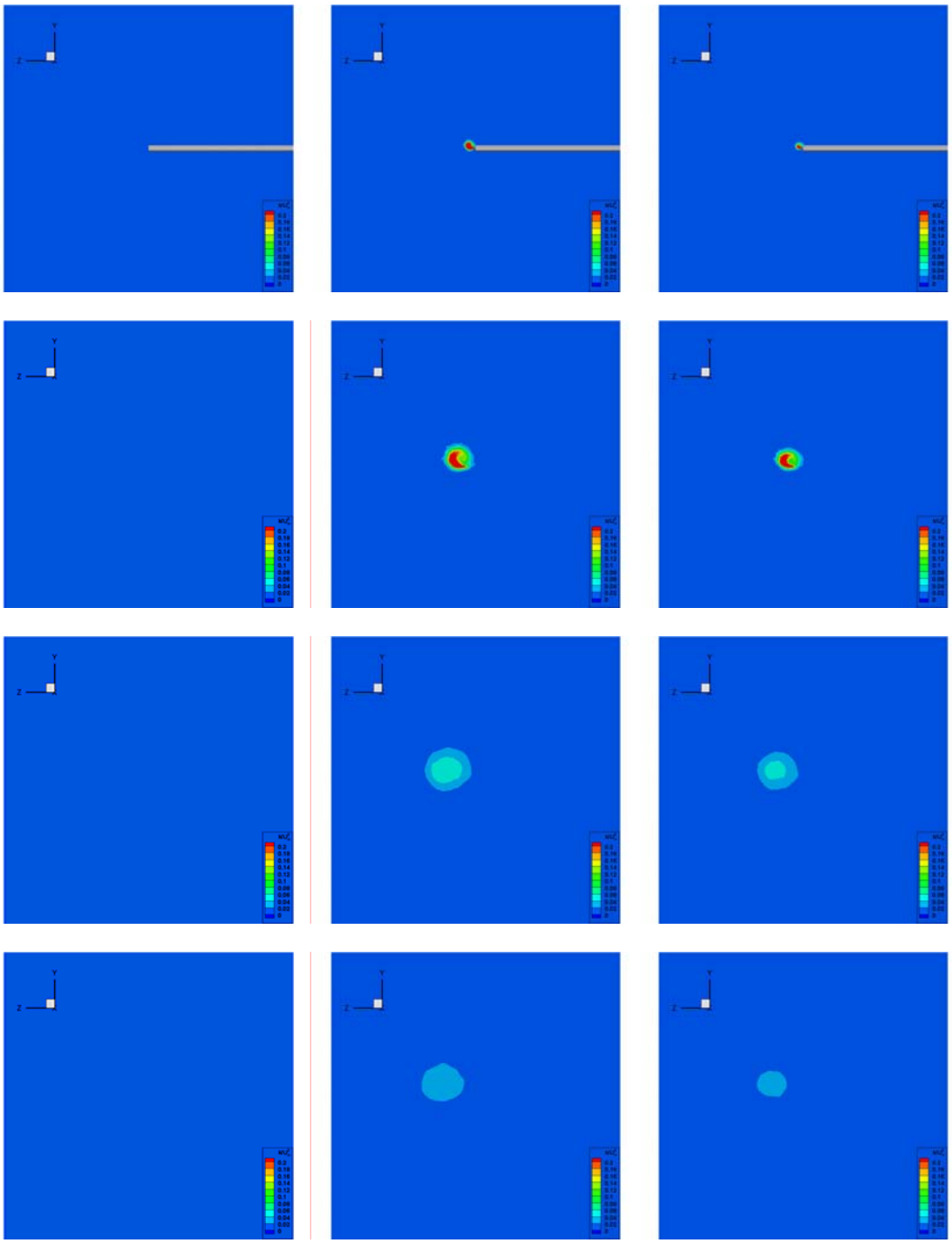

$C_\mu = 0$, no injection (1st column)

$C_\mu = 0.220$, uniform injection (2nd column)

$C_\mu = 0.054$, triangular waveform injection (3rd column)

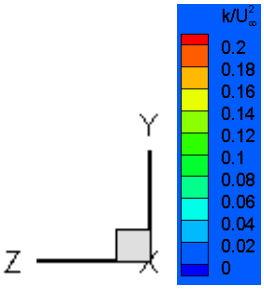

Figure 3.22: Dimensionless turbulence kinetic energy for no injection (left column), uniform injection (middle column) and triangular waveform injection (right column) cases at 4° angle of attack of 4 different stations starting from leading edge, which are located at 0.5 chord (1st row), 1 chord (2nd row), 2 chord (3rd row), 3 chord (4th row).

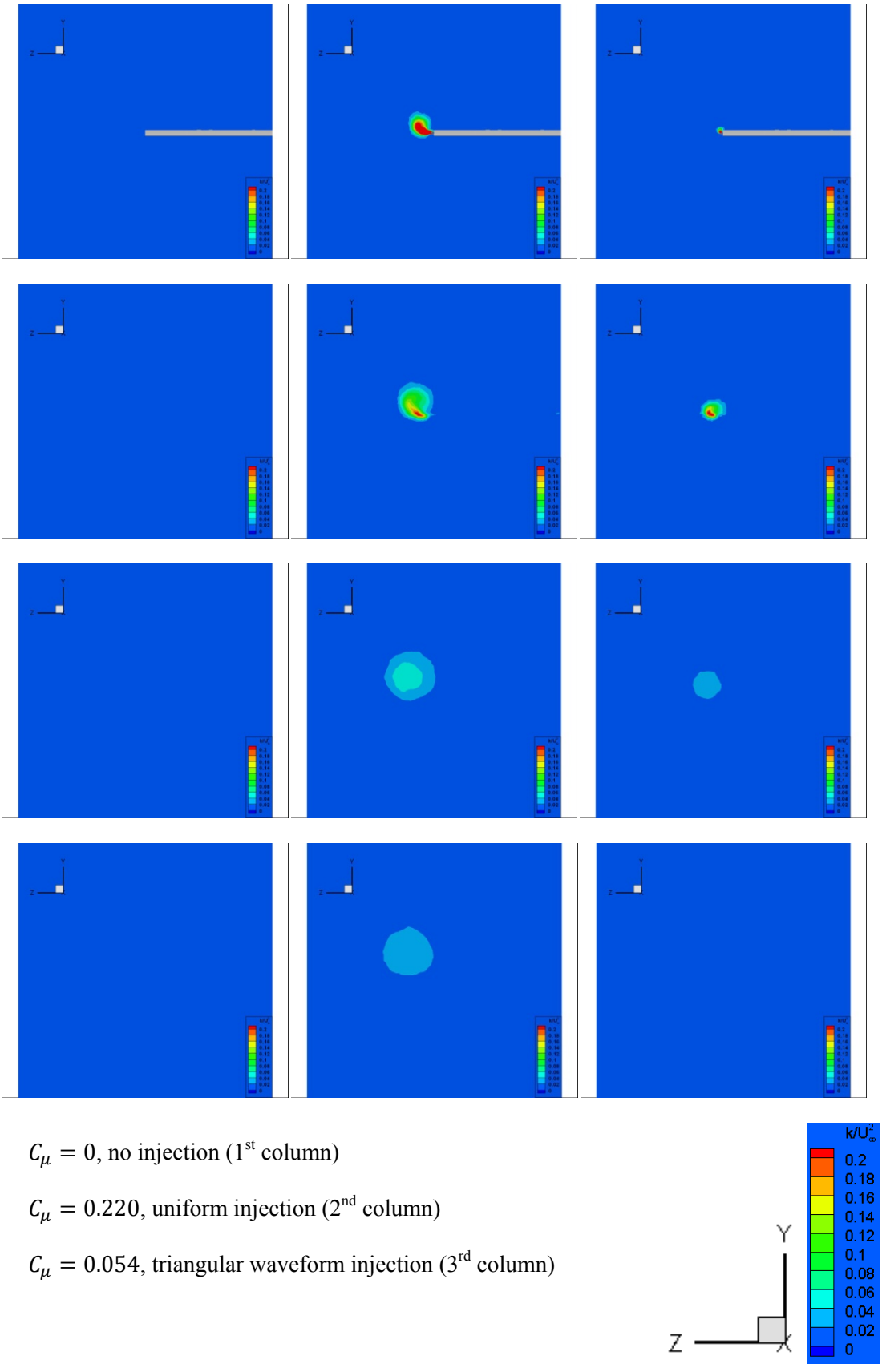

Figure 3.23: Dimensionless turbulence kinetic energy for no injection (left column), uniform injection (middle column) and triangular waveform injection (right column) cases at 8° angle of attack of 4 different stations starting from leading edge, which are located at 0.5 chord (1st row), 1 chord (2nd row), 2 chord (3rd row), 3 chord (4th row).

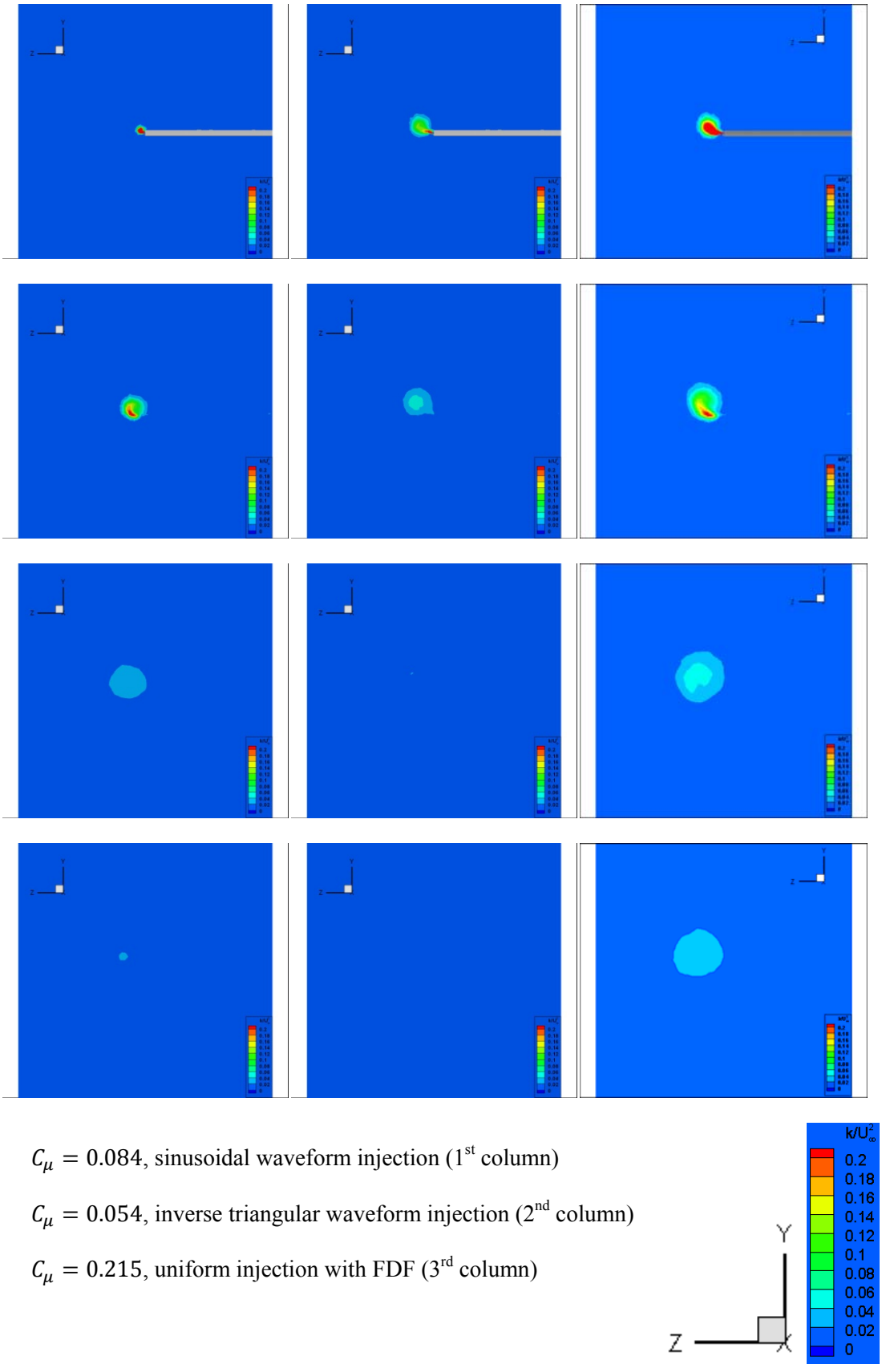

Figure 3.24: Dimensionless turbulence kinetic energy for sinusoidal waveform injection (left column), inverse waveform injection (middle column) and uniform injection with FDF (right column) cases at 8° angle of attack of 4 different stations starting from leading edge, which are located at 0.5 chord (1st row), 1 chord (2nd row), 2 chord (3rd row), 3 chord (4th row).

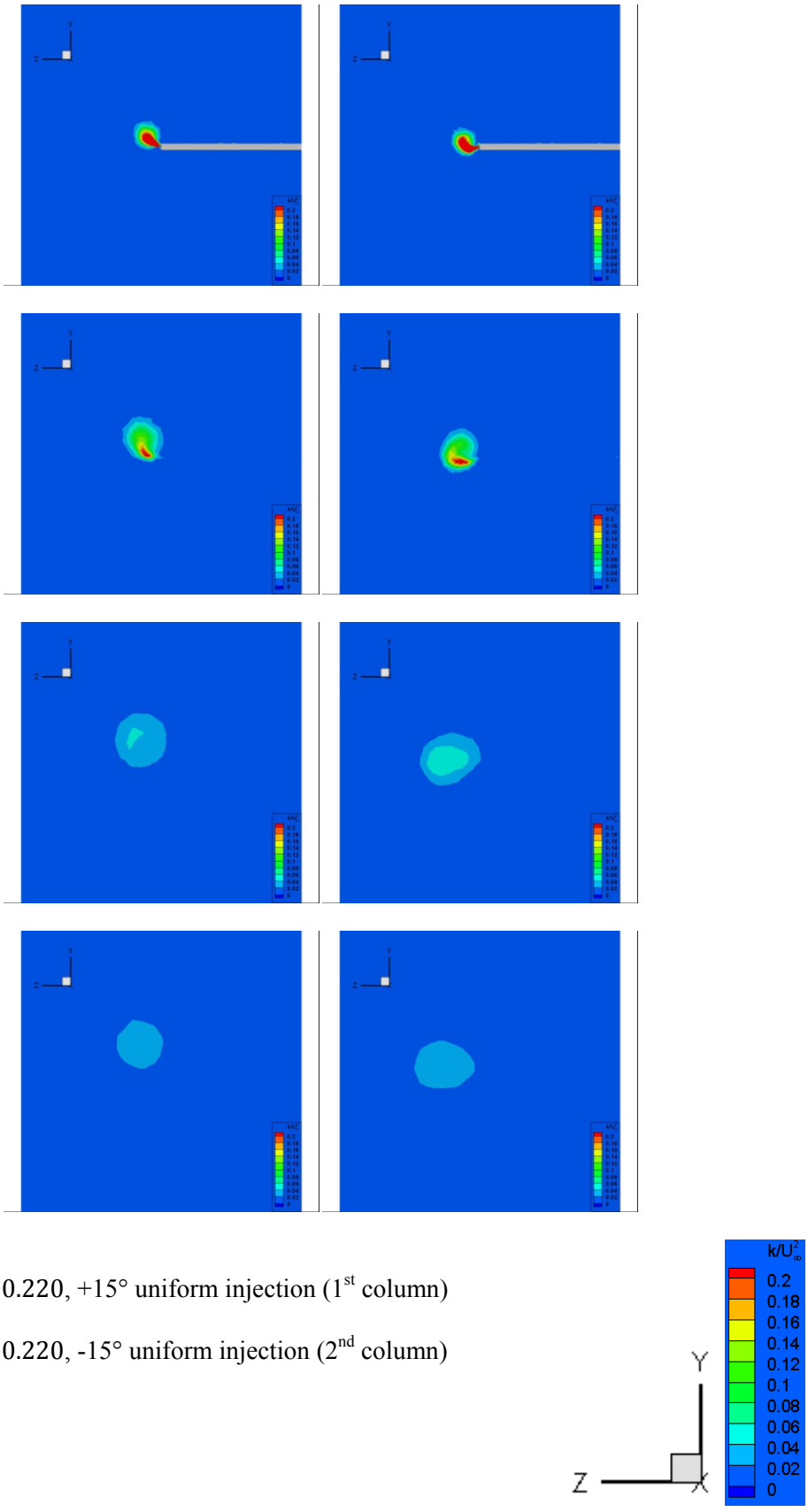

Figure 3.25: Dimensionless turbulence kinetic energy for +15° uniform injection (left column) and -15° uniform injection (right column) cases at 8° angle of attack of 4 different stations starting from leading edge, which are located at 0.5 chord (1st row), 1 chord (2nd row), 2 chord (3rd row), 3 chord (4th row).

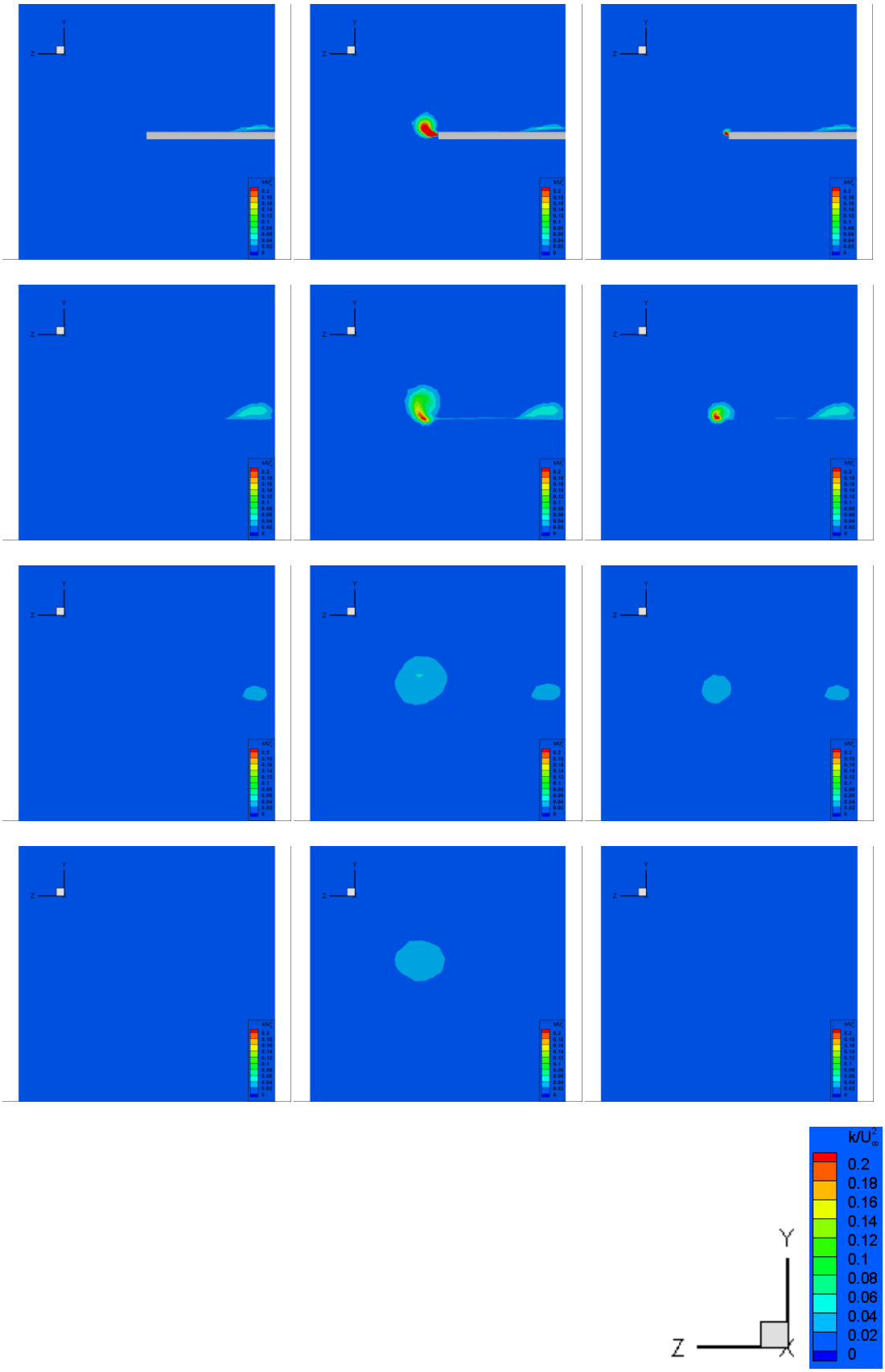

Figure 3.26: Dimensionless turbulence kinetic energy for no injection (left column), uniform injection (middle column) and triangular waveform injection (right column) cases at 12° angle of attack of 4 different stations starting from leading edge, which are located at 0.5 chord (1st row), 1 chord (2nd row), 2 chord (3rd row), 3 chord (4th row).

3.2.5 Vorticity Magnitude:

This parameter shows the magnitude of circulation density while the vector field is representing velocity. Moreover, vorticity magnitude certainly determines the location and strength of the vortex patterns.

At 4 angle of attack cases, in no injection case, tip vortex is visible and has integrity while forming a single pattern; however in cases with injection, single vortex is leaving the wing at the trailing edge (x=1.0 c) and decomposes into two zones. Streamlines on the figure 3.27 shows secondary zone do not have rotating characteristics. It has formed due to the injection and gained increase in velocity and energy due to the low pressure field that tip injection caused.

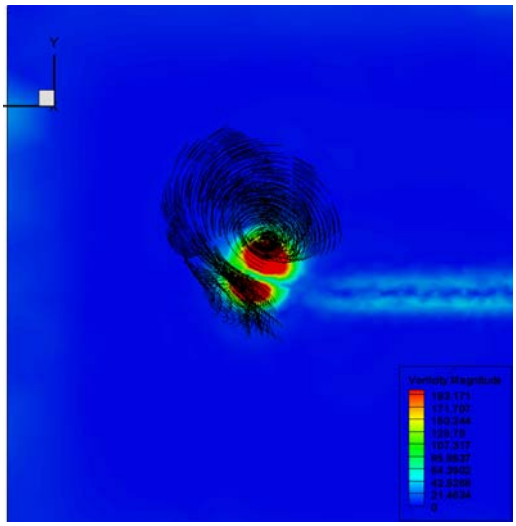

Figure 3.27: Streamlines, vorticity magnitude, 4 angle of attack case with uniform injection at station x= 2 c

At similar cases like triangular waveform, sinusoidal waveform and inverse triangular waveform injection (by means of momentum coefficient), a shift in the location of two tip fields were observed, especially at relatively high angle of attack configurations. The strength of the tip vortex makes the weaker tip injections to bend more easily than in cases with uniform injection (figure 3.26 to 3.30). In that way, injected flow cannot head directly in the +z axis for a long distance and this affects the locations of the fields. This argument can be justified by looking at the case with +15° angled injection, as well (figure 3.29). Considering the positive inclination of injection, two high magnitude fields rotate clockwise and forms an east-west type of direction rather than north-south type, as in the cases with lower momentum coefficient values.

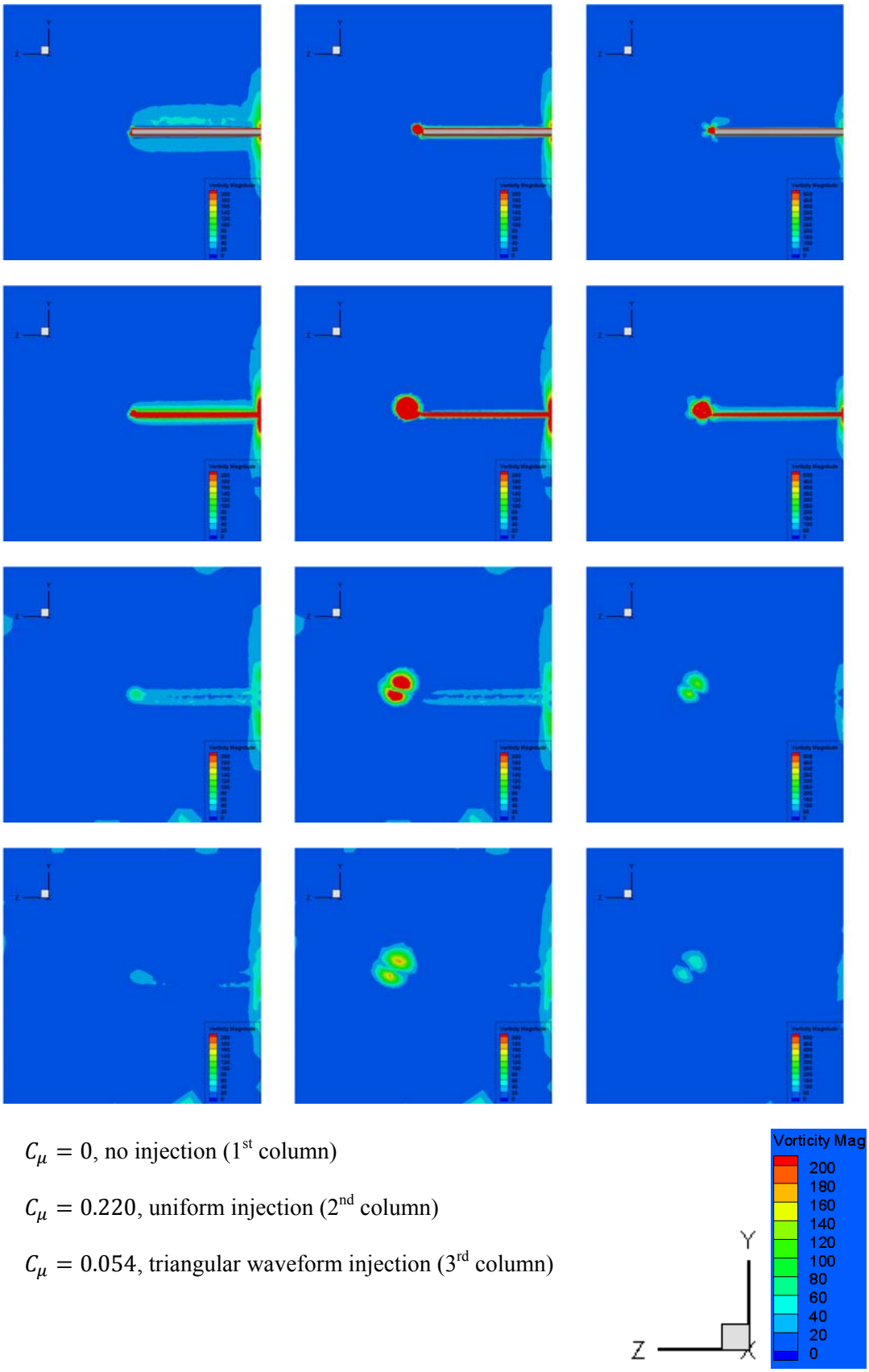

Figure 3.28: Vorticity magnitude for no injection (left column), uniform injection (middle column) and triangular waveform injection (right column) cases at 4° angle of attack of 4 different stations starting from leading edge, which are located at 0.5 chord (1st row), 1 chord (2nd row), 2 chord (3rd row), 3 chord (4th row).

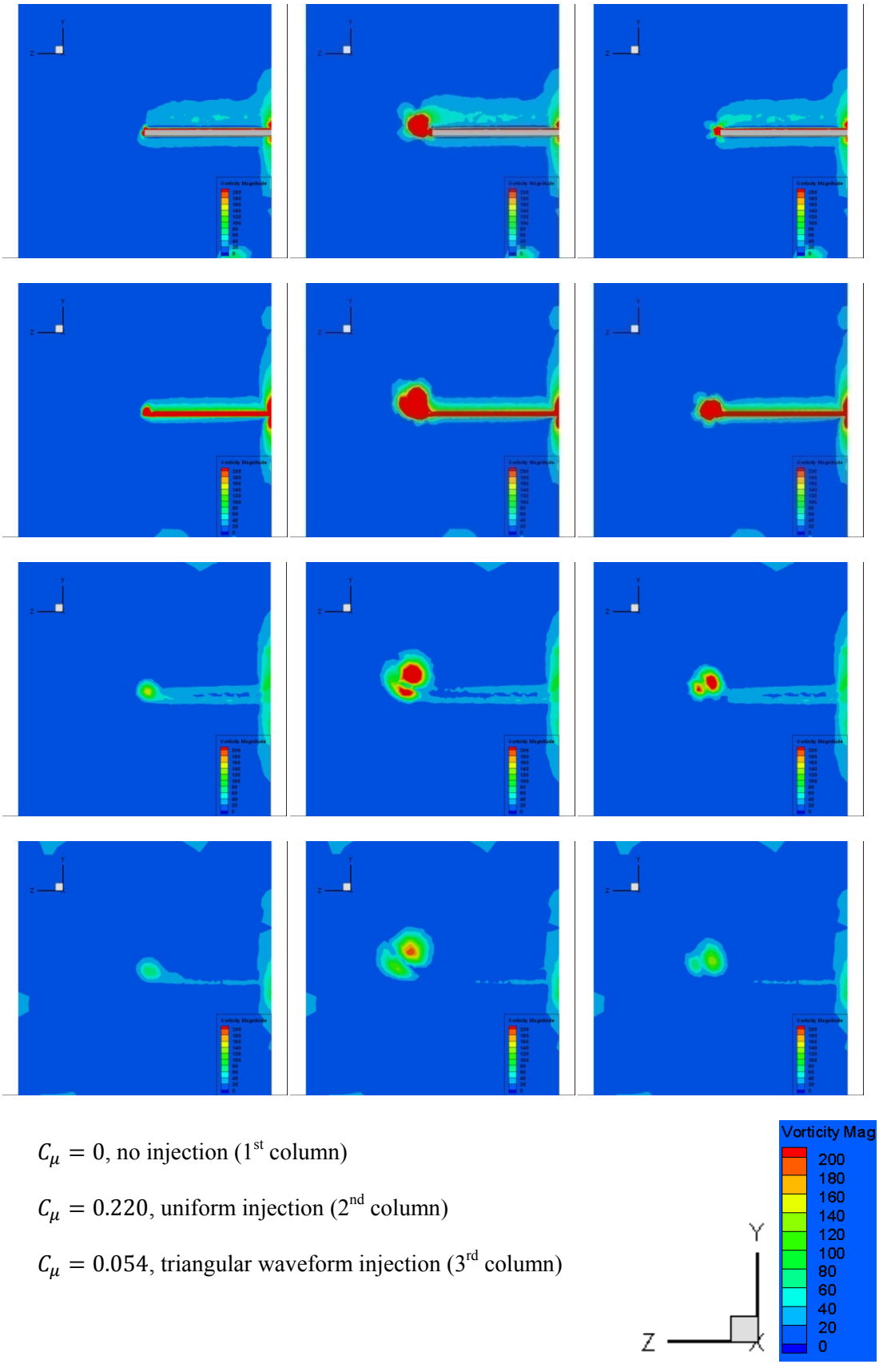

Figure 3.29 Vorticity magnitude for no injection (left column), uniform injection (middle column) and triangular waveform injection (right column) cases at 8° angle of attack of 4 different stations starting from leading edge, which are located at 0.5 chord (1st row), 1 chord (2nd row), 2 chord (3rd row), 3 chord (4th row).

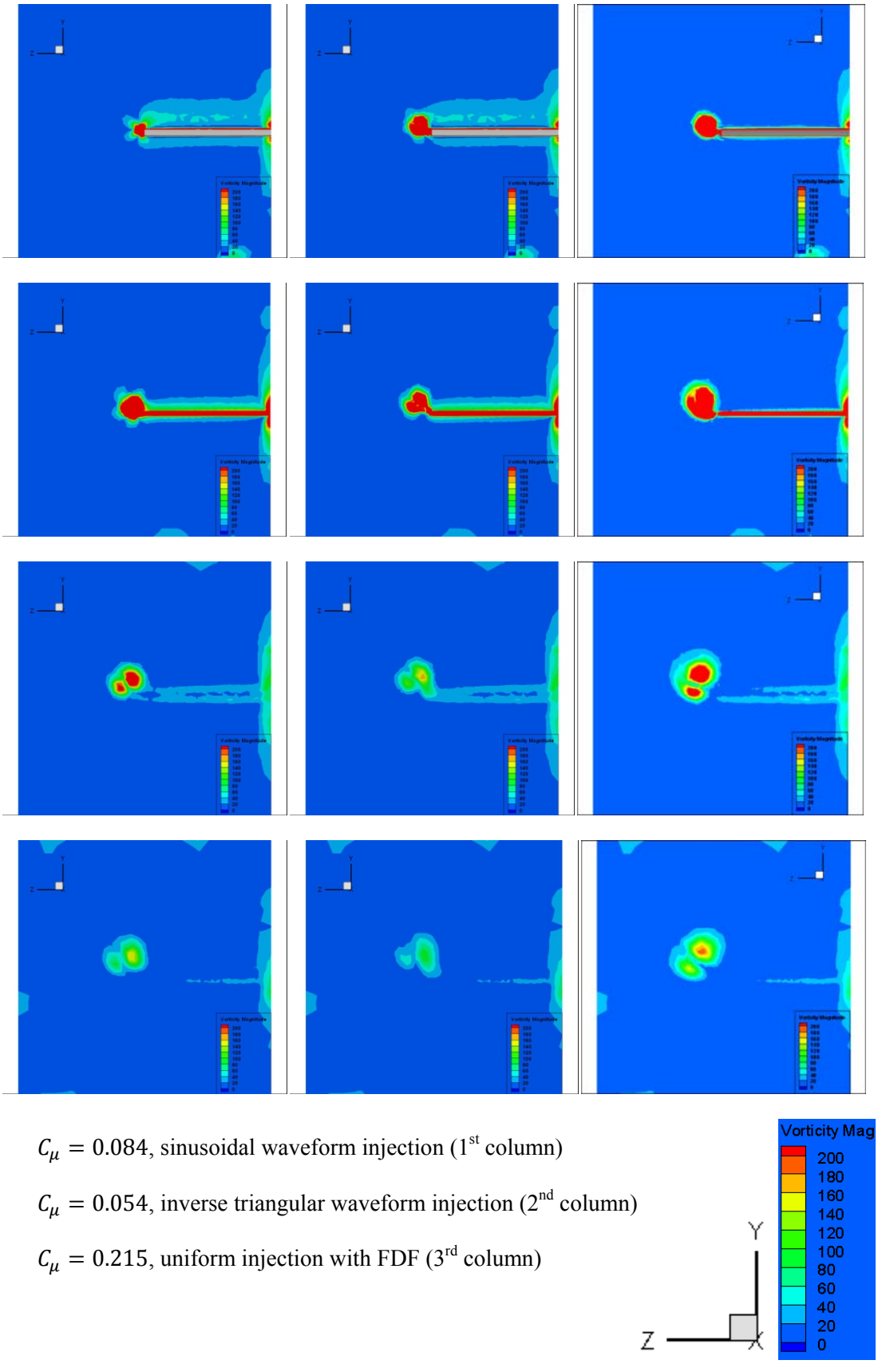

Figure 3.30: Vorticity magnitude for sinusoidal waveform injection (left column), inverse waveform injection (middle column) and uniform injection with FDF (right column) cases at 8° angle of attack of 4 different stations starting from leading edge, which are located at 0.5 chord (1st row), 1 chord (2nd row), 2 chord (3rd row), 3 chord (4th row).

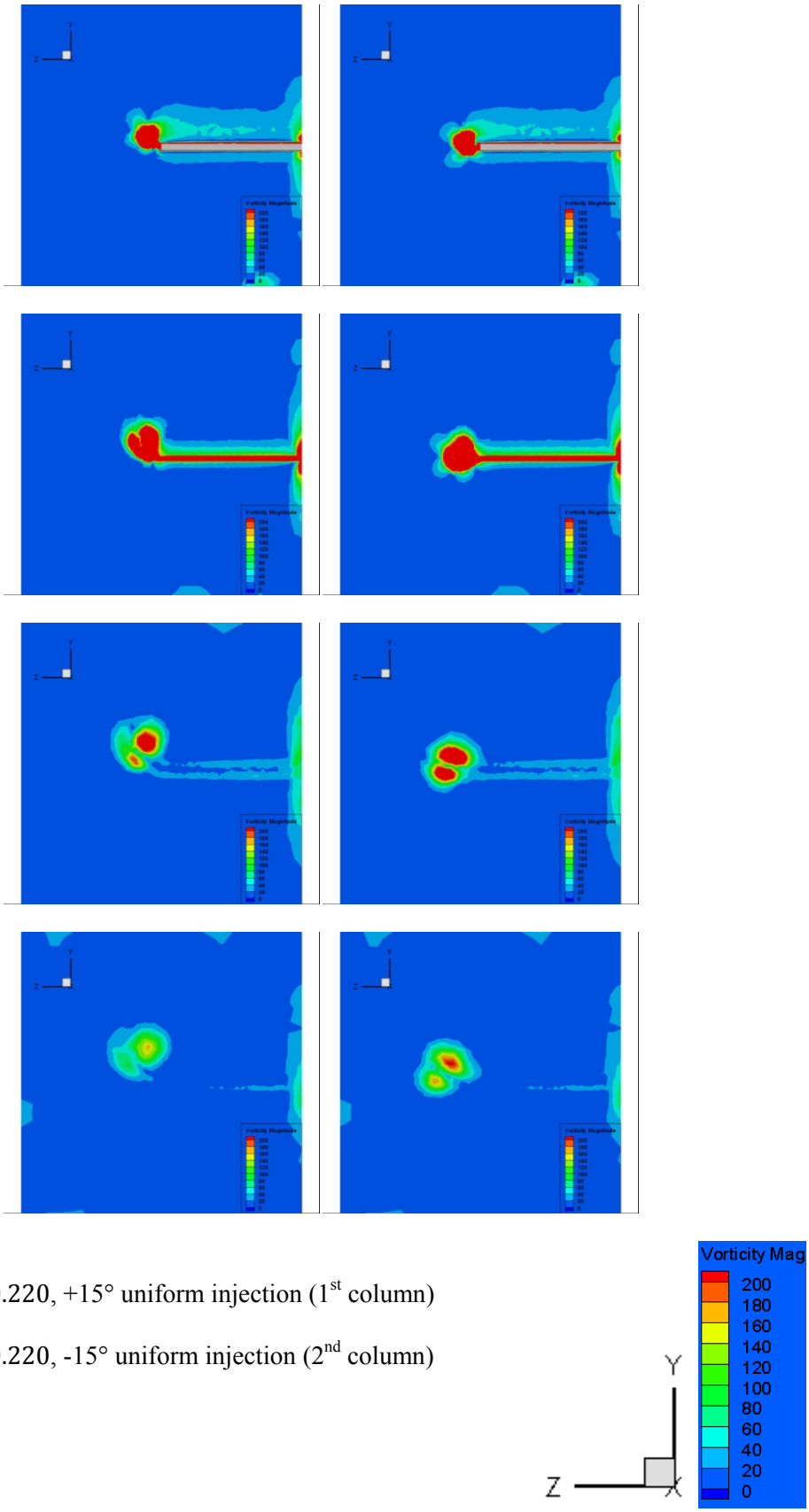

Figure 3.31: Vorticity magnitude for +15° uniform injection (left column) and -15° uniform injection (right column) cases at 8° angle of attack of 4 different stations starting from leading edge, which are located at 0.5 chord (1st row), 1 chord (2nd row), 2 chord (3rd row), 3 chord (4th row).

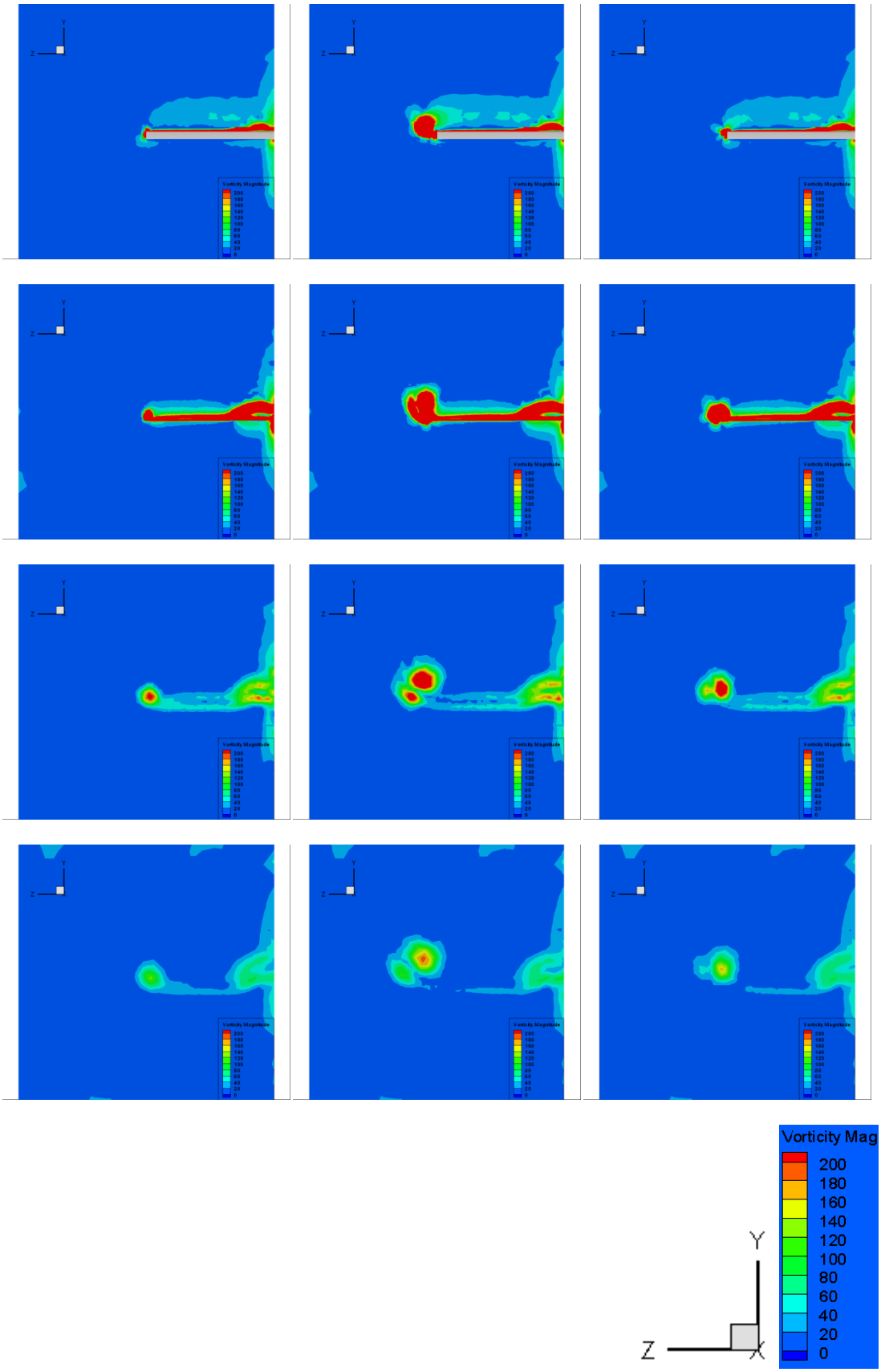

Figure 3.32: Vorticity magnitude for no injection (left column), uniform injection (middle column) and triangular waveform injection (right column) cases at 12° angle of attack of 4 different stations starting from leading edge, which are located at 0.5 chord (1st row), 1 chord (2nd row), 2 chord (3rd row), 3 chord (4th row).

3.2.6 Pressure Coefficient (C_P):

Pressure coefficient plots show the pressure distribution on the wing, tip region and wake in the domain and determine the high and low pressure zones accordingly.

While injections and tip leakage create a low pressure field, a corresponding high pressure field builds up at the left side of it and as the angle of attack increases, growth in the sizes of both zones is observed. Yet again, uniform injection cases create the biggest pressure differences due to high momentum coefficient compared to other cases (figure 3.33 to 3.37). Injection cases with lower momentum coefficient, i.e. triangular waveform, sinusoidal waveform, inverse triangular waveform, and +15° angled uniform injection have a tendency to form a single low pressure field according to the direction of injection.

At 12° angle of attack cases (figure 3.37), pressure differences are at the highest level; especially considering the disturbance in the flow at the root section, which will lead to stall eventually.

Secondly, on figures 3.38 to 3.39, carpet plot of c_P was presented. The intention is observing the change of pressure on the wing surfaces with and without injection. At 50% span plots (figure 3.38), c_P values of cases with relatively smaller cμ show very similar behavior compared to no injection case, however increase in the cμ slightly decreases the pressure coefficient at the suction side of the wing, leading to an increase in lift even at mid span. c_P distribution at 95% span was presented on figure 3.39; showing for both cμ values, overall c_P is decreased significantly on the suction side, proving that especially at the tip region, tip injection methods provides lift increments by increasing the effective wing area.

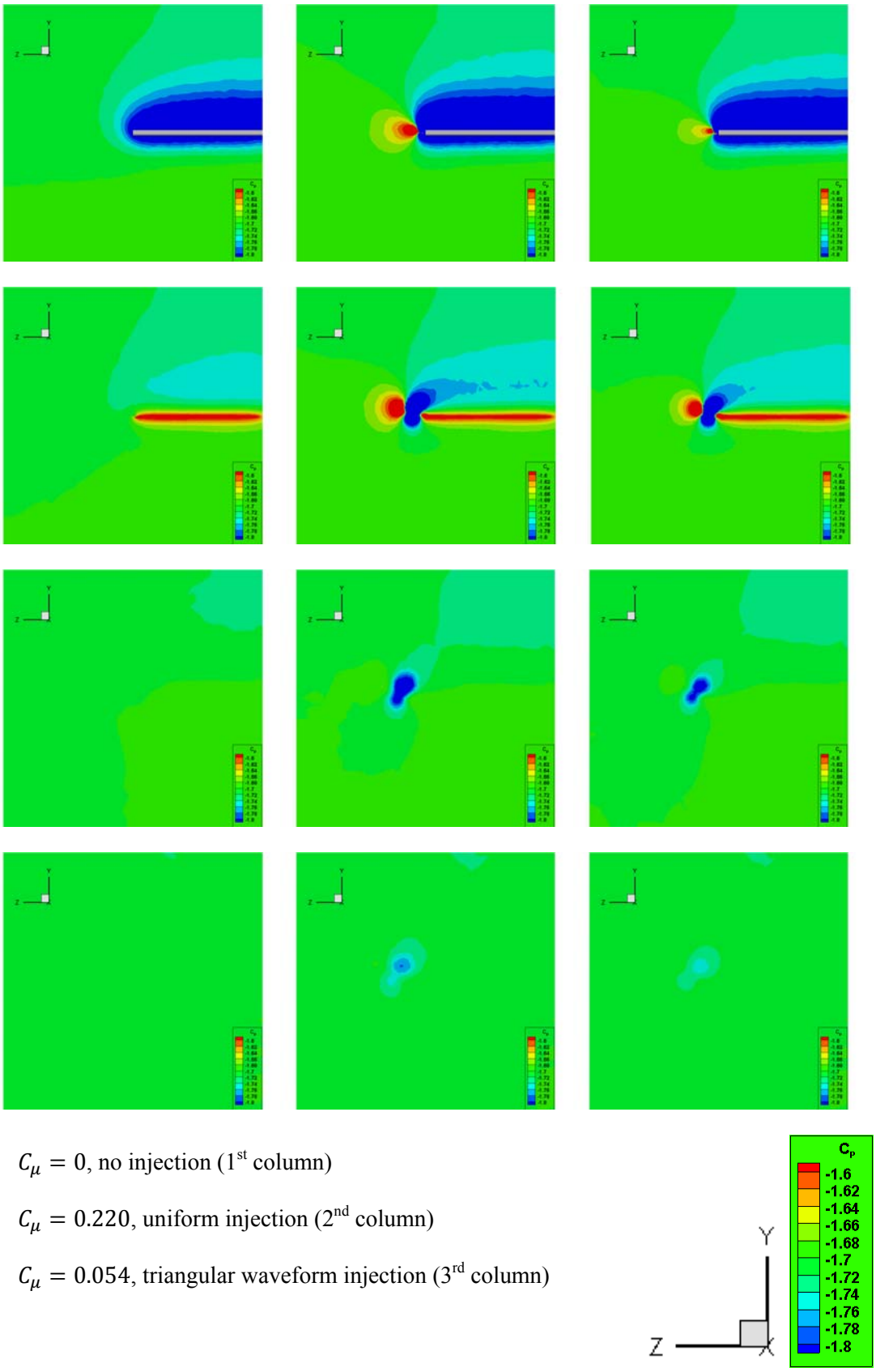

Figure 3.33: Cp for no injection (left column), uniform injection (middle column) and triangular waveform injection (right column) cases at 4° angle of attack of 4 different stations starting from leading edge, which are located at 0.5 chord (1st row), 1 chord (2nd row), 2 chord (3rd row), 3 chord (4th row).

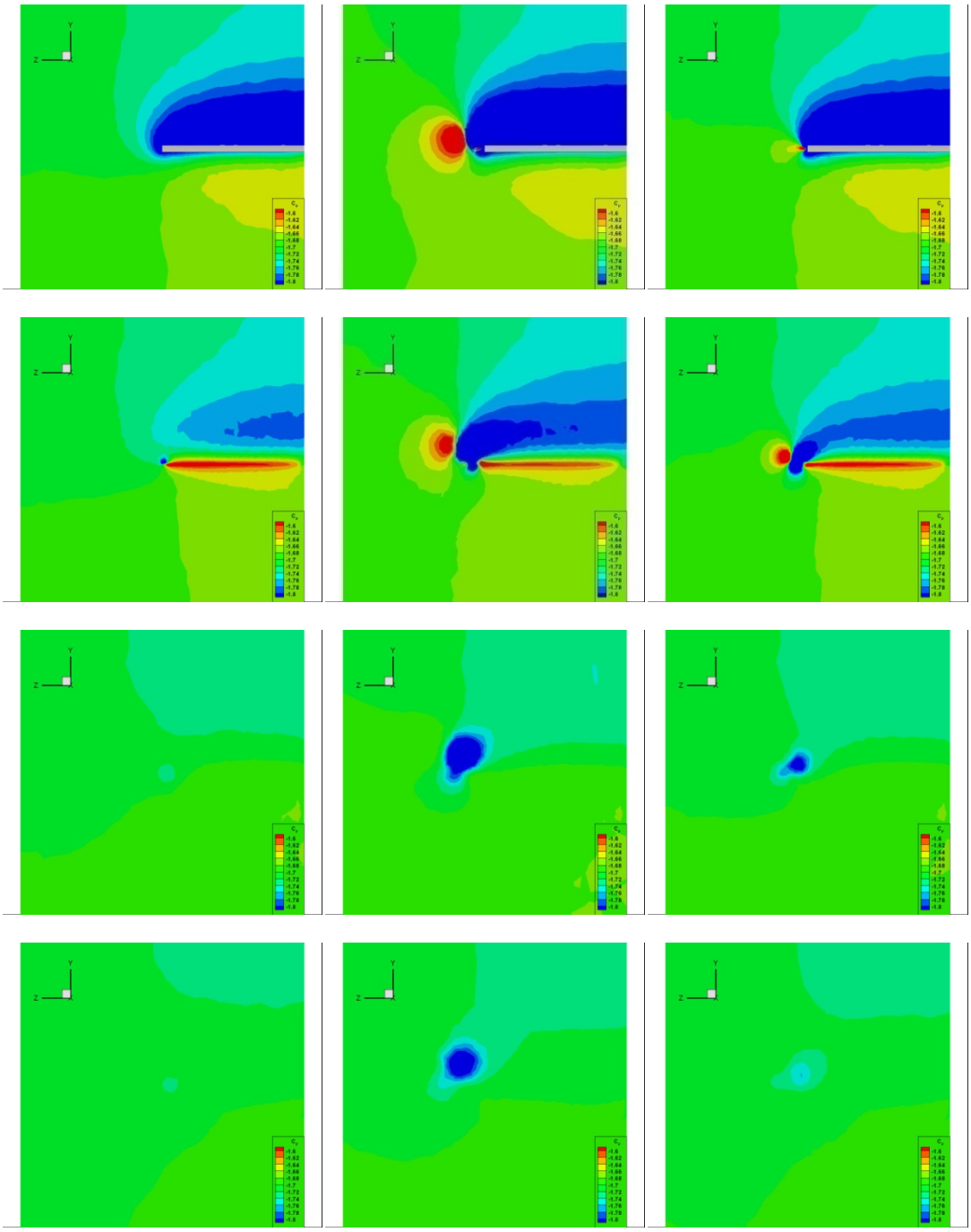

Figure 3.34: Cp for no injection (left column), uniform injection (middle column) and triangular waveform injection (right column) cases at 8° angle of attack of 4 different stations starting from leading edge, which are located at 0.5 chord (1st row), 1 chord (2nd row), 2 chord (3rd row), 3 chord (4th row).

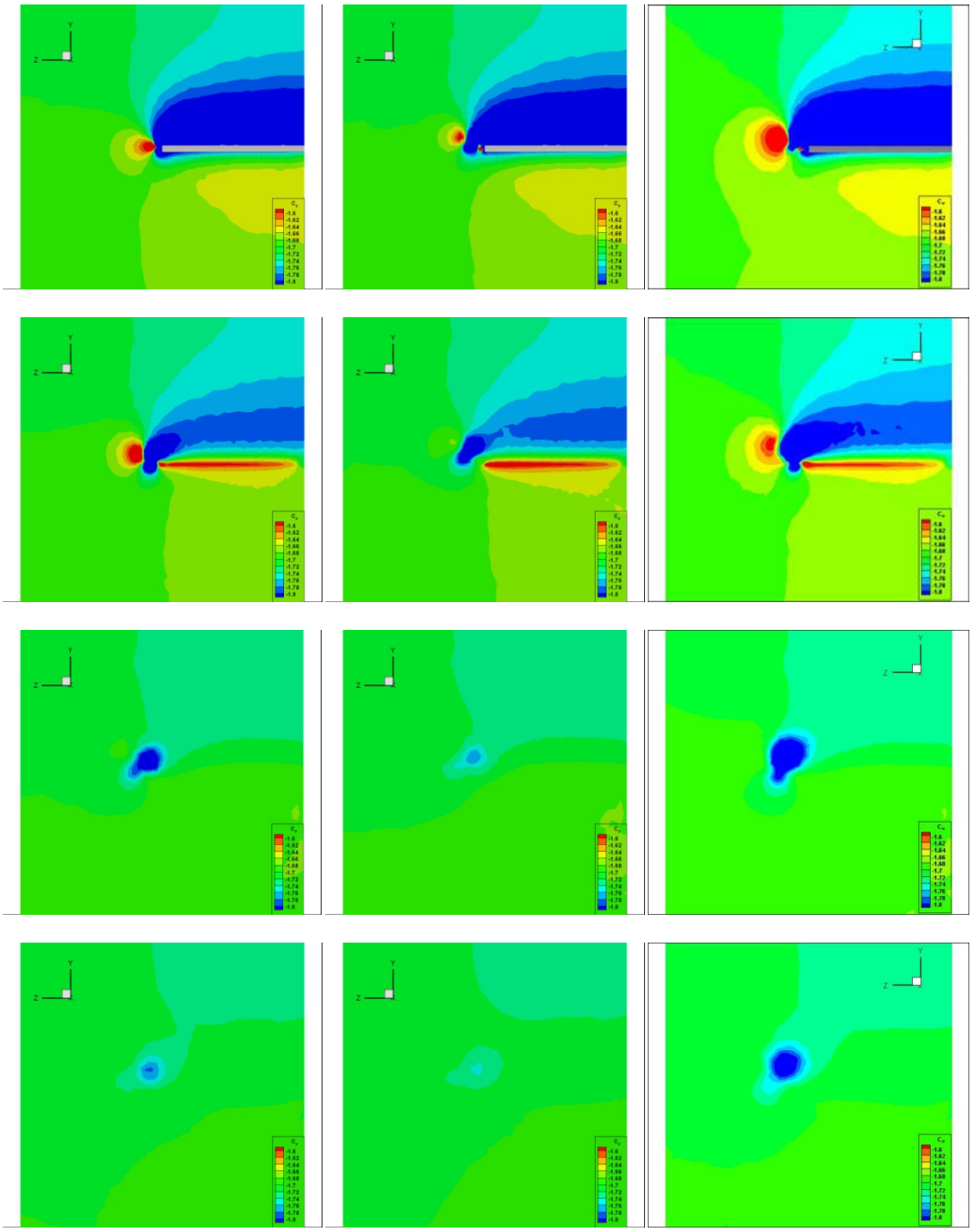

$C_\mu = 0.084$, sinusoidal waveform injection (1st column)

$C_\mu = 0.054$, inverse triangular waveform injection (2nd column)

$C_\mu = 0.215$, uniform injection with FDF (3rd column)

Figure 3.35: Cp for sinusoidal waveform injection (left column), inverse waveform injection (middle column) and uniform injection with FDF (right column) cases at 8° angle of attack of 4 different stations starting from leading edge, which are located at 0.5 chord (1st row), 1 chord (2nd row), 2 chord (3rd row), 3 chord (4th row).

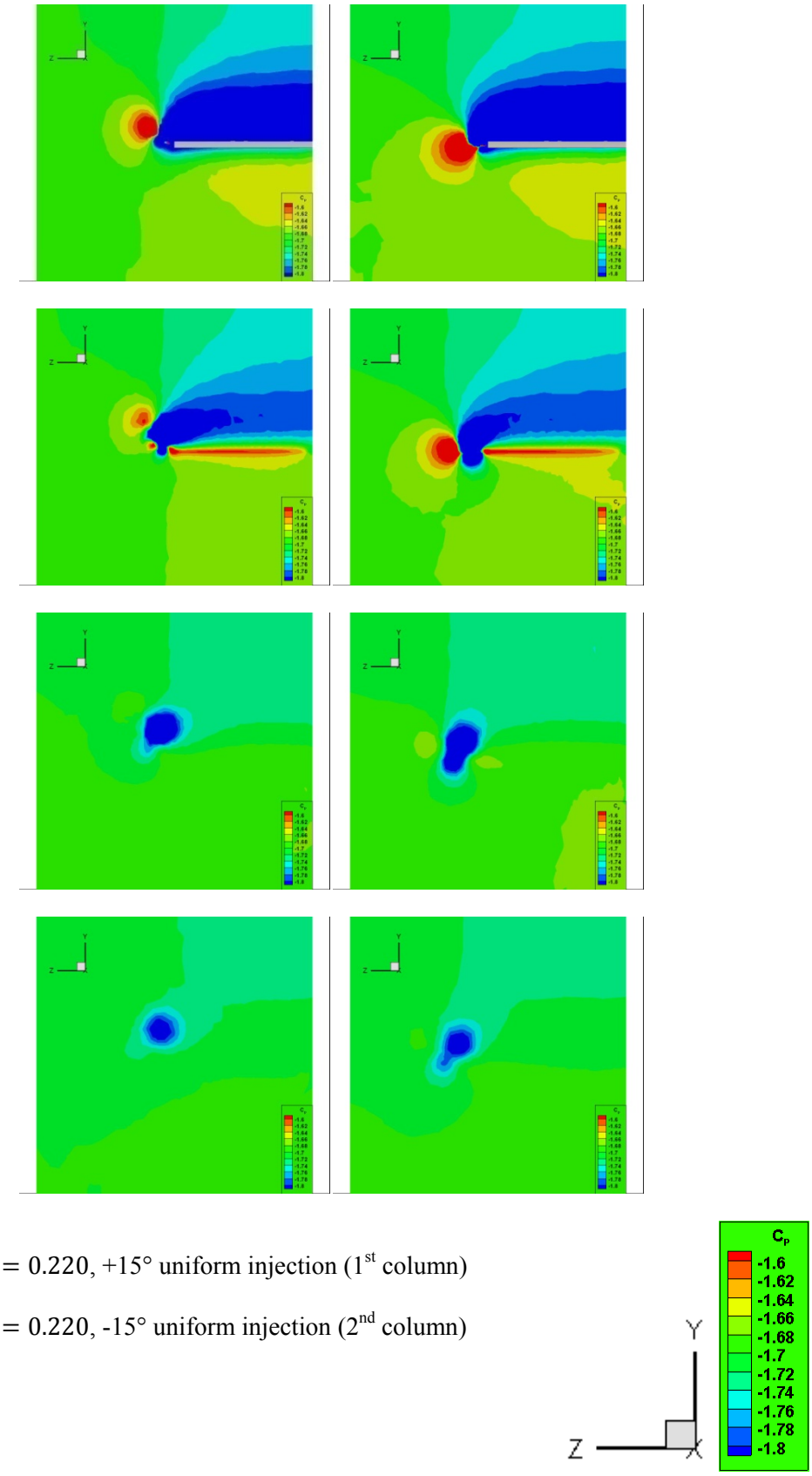

Figure 3.36: Cp for +15° uniform injection (left column) and -15° uniform injection (right column) cases at 8° angle of attack of 4 different stations starting from leading edge, which are located at 0.5 chord (1st row), 1 chord (2nd row), 2 chord (3rd row), 3 chord (4th row).

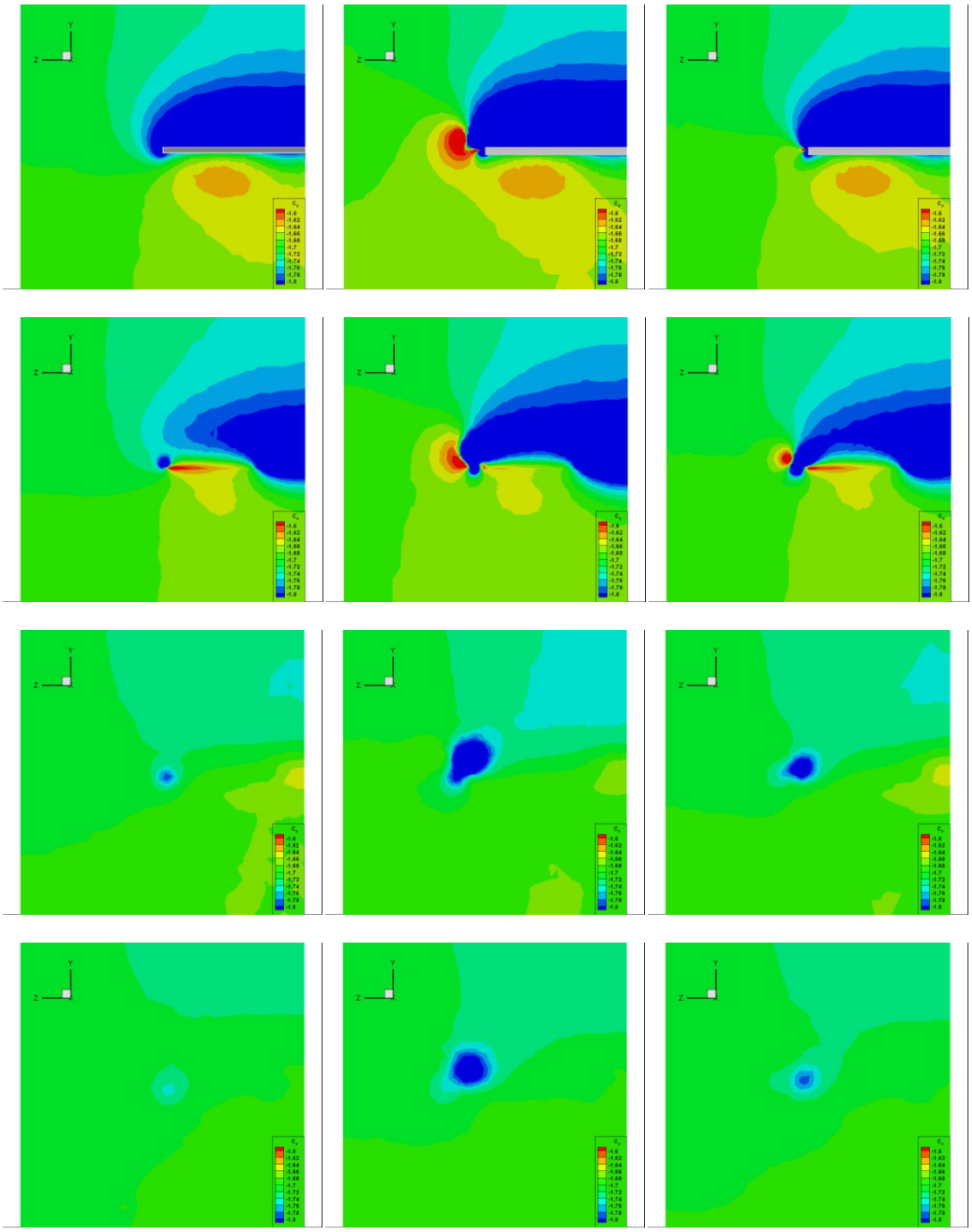

Figure 3.37: Cp for no injection (left column), uniform injection (middle column) and triangular waveform injection (right column) cases at 12° angle of attack of 4 different stations starting from leading edge, which are located at 0.5 chord (1st row), 1 chord (2nd row), 2 chord (3rd row), 3 chord (4th row).

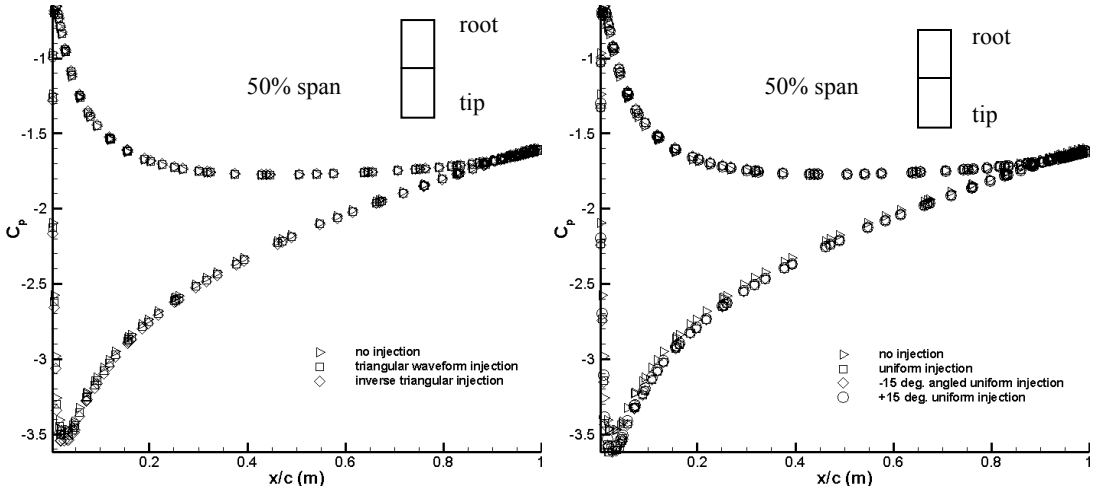

Figure 3.38: Chordwise c_P distribution on the wing with different injection cases and momentum coefficients, i.e. cμ=0.054 (left), cμ=0.22 (right) at 50% span plane.

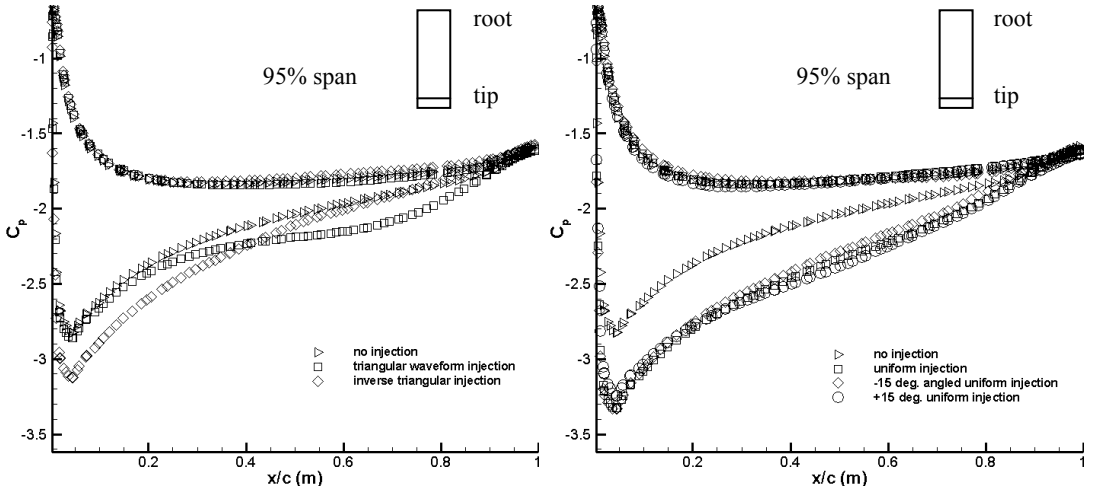

Figure 3.39: Chordwise c_P distribution on the wing with different injection cases and momentum coefficients, i.e. cμ=0.054 (left), cμ=0.22 (right) at 95% span plane.

3.2.7 Comparison of Uniform Injection Cases with/without Fully Developed Flow:

Regardless of the injection tube diameters, a validation case must essentially be presented. In the figure below (figure 3.40), velocity contour plots show that, in the case including fully developed flow, high velocity contours are larger in size; however that difference gradually decreases on the lower velocity curves. On the contour plots presented above, results of the two cases were slightly different, yet showing the same overall behavior. On the validation case below, it's observed that locating the vortex core in the case without fully developed tubular flow has a better accuracy compared to the former case according to the experimental results.

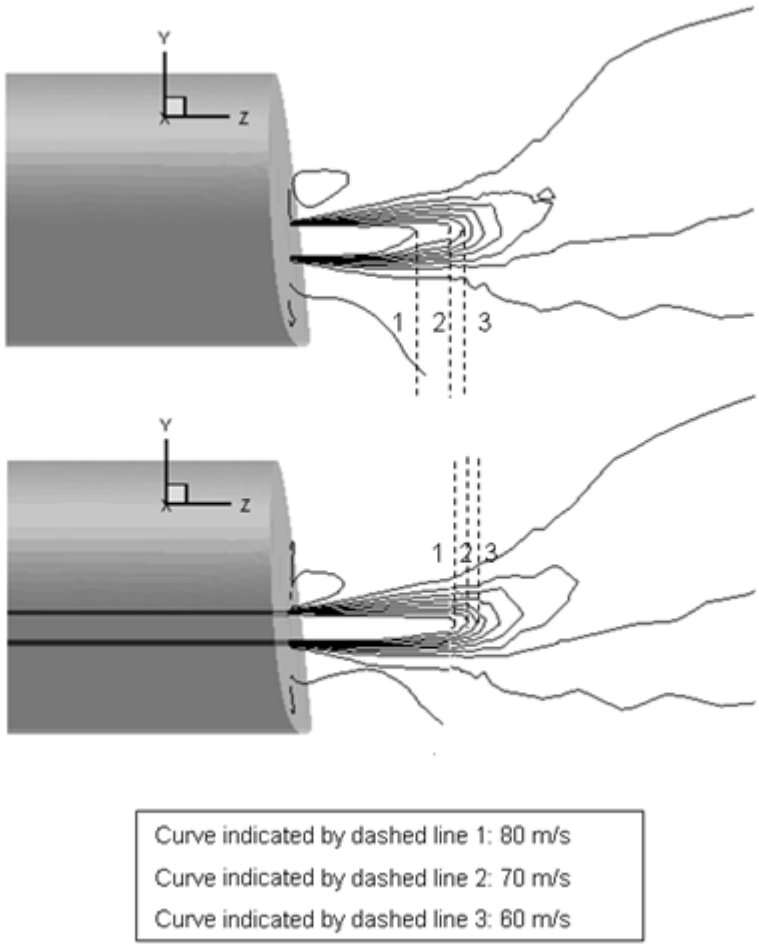

Figure 3.40: Comparison of injection velocity (z component) of uniform injection case (upper) and uniform injection case with FDF (lower).

3.2.8 Lift and Drag Coefficients:

Forces acting on the wing were computed, as well. Perpendicular component of the total force with respect to oncoming flow, i.e. lift, is represented by the dimensionless parameter c_L while drag, which is the component parallel to the flow direction, is represented by c_D.

First of all, results belong to three common cases for all angle of attack configurations, namely no injection, uniform and triangular waveform injection, are presented (figure 3.41). Lift coefficients of 8° angle of attack configuration with additional cases are plotted in graph, as well (figure 3.42). For all common cases, uniform injection is observed as the most successful injection method by means of lift increment. As the angle of attack increases, the gap between uniform injection and other types are increasing. For configurations with larger angle of attack, tip disturbance increases, tip vortices get larger and stronger, and inherently tip losses emerge; however uniform injection method decreases the loss of lift and the performance increases with increasing angle of attack.

Secondly, 8° angle of attack cases were investigated solely. Performance of the uniform injection is the best compared to other injection scenarios; angled uniform injections are following uniform injection with very slight differences. In total, uniform injection gives %14.5 increase of lift compared to case with no injection. Percent changes in the lift and drag is presented below (Table 3.1)

Table 3.1: Lift and drag coefficients, percent change for different cases

Percent Change in Lift and Drag Coefficient				
	4 aoa	**8 aoa**	**12 aoa**	
Uniform	19.53	14.48	12.37	**CL**
	0.08	0.78	2.45	**CD**
Triangular Waveform	9.20	4.28	4.31	**CL**
	0.82	1.14	1.73	**CD**
Sinus waveform		6.76		**CL**
		1.41		**CD**
Inverse Tr. Waveform		7.18		**CL**
		-0.21		**CD**
Uniform w/ (FDF)		7.90		**CL**
		-3.37		**CD**
Uniform +15° ang.		13.26		**CL**
		1.20		**CD**
Uniform -15° ang.		14.09		**CL**
		0.32		**CD**

Variation of the drag coefficient was plotted in figures 3.43 and 3.44. First of all, common cases were compared as the previous lift coefficient graph (figure 3.43). For moderate angles of attack, the drag coefficient values are close to each other, yet triangular waveform injection has the highest drag while drag coefficient resulted from uniform injection case is slightly higher than the no injection case. As the angle of attack increases, drag coefficient at uniform injection case increased dramatically, and gets the highest value at 12 angle of attack configuration. Comparing the 8 angle of attack cases (figure 3.44), it's observed that uniform injection with fully developed flow simulation has the lowest drag coefficient value. This is due to the fact that tube exit gaps were defined as surfaces and assigned velocity inlet boundary conditions in rest of the cases. This particular change in the definition of boundary condition leads to a change in the exit velocity distribution, as well as exit jet density. As a result, lift and drag values are lower than any uniform injection cases according to the change in the velocity and density of the jet flow.

Moreover, on figures 3.45 and 3.46 lift to drag ratio of all cases were compared. As expected, uniform injections are the most effective cases by means of high lift and relatively lower drag. Among four different uniform injection cases, -15° uniform injection has the highest L/D ratio, making this injection type to be the most suitable one by means of optimum performance.

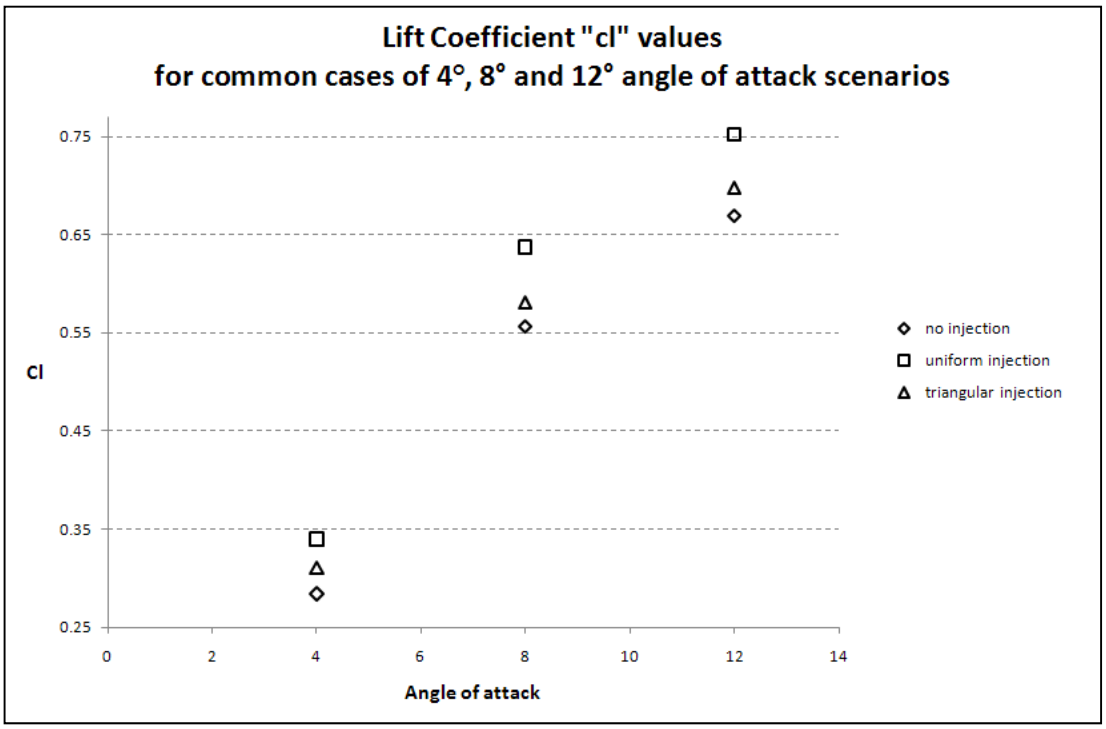

Figure 3.41: Lift coefficient for common cases at all angle of attack configurations

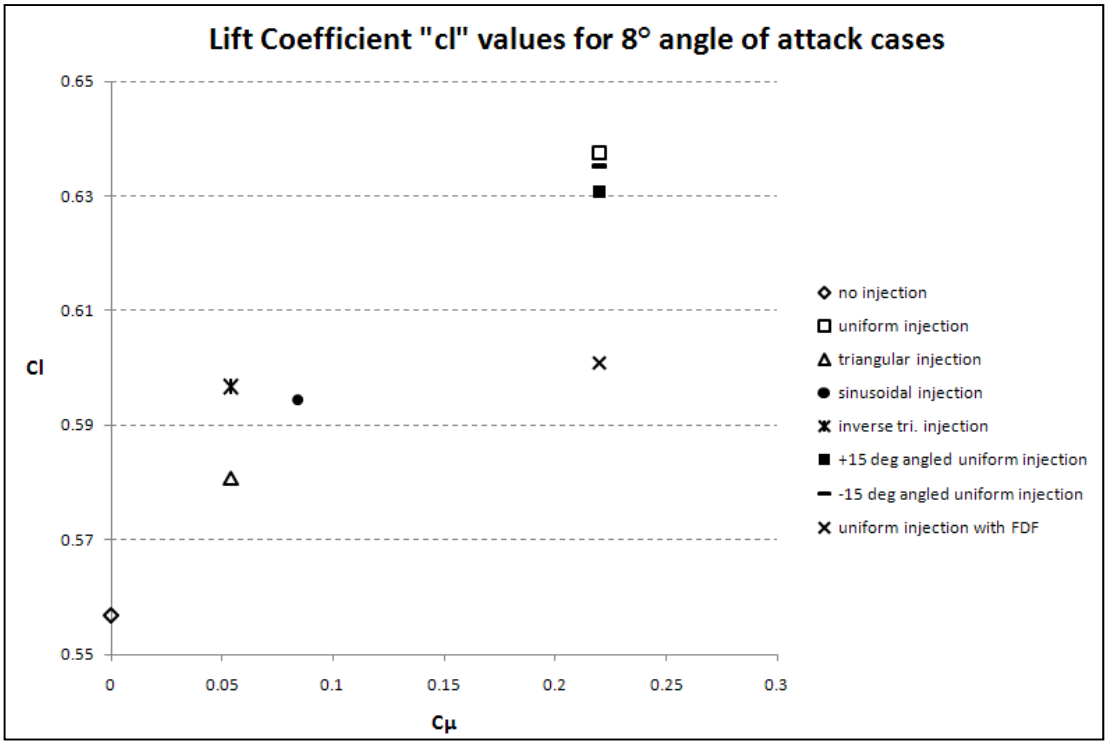

Figure 3.42: Jet momentum vs. lift coefficient for injection cases having 8° angle of attack configuration.

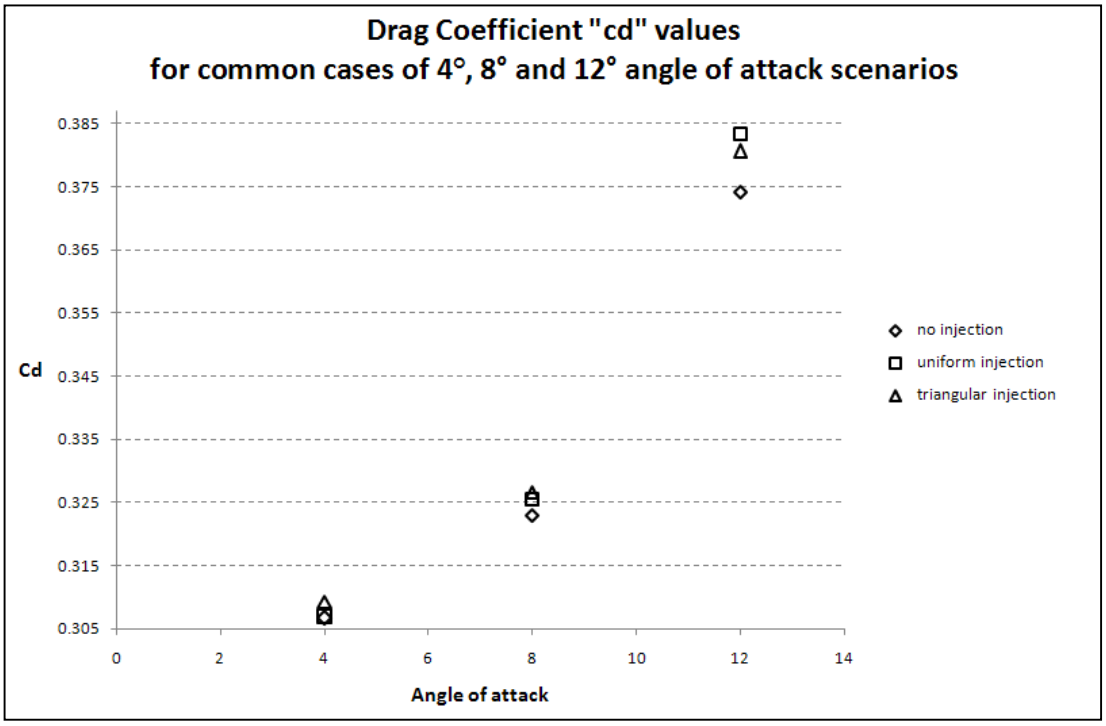

Figure 3.43: Drag coefficient for common cases at all angle of attack configurations

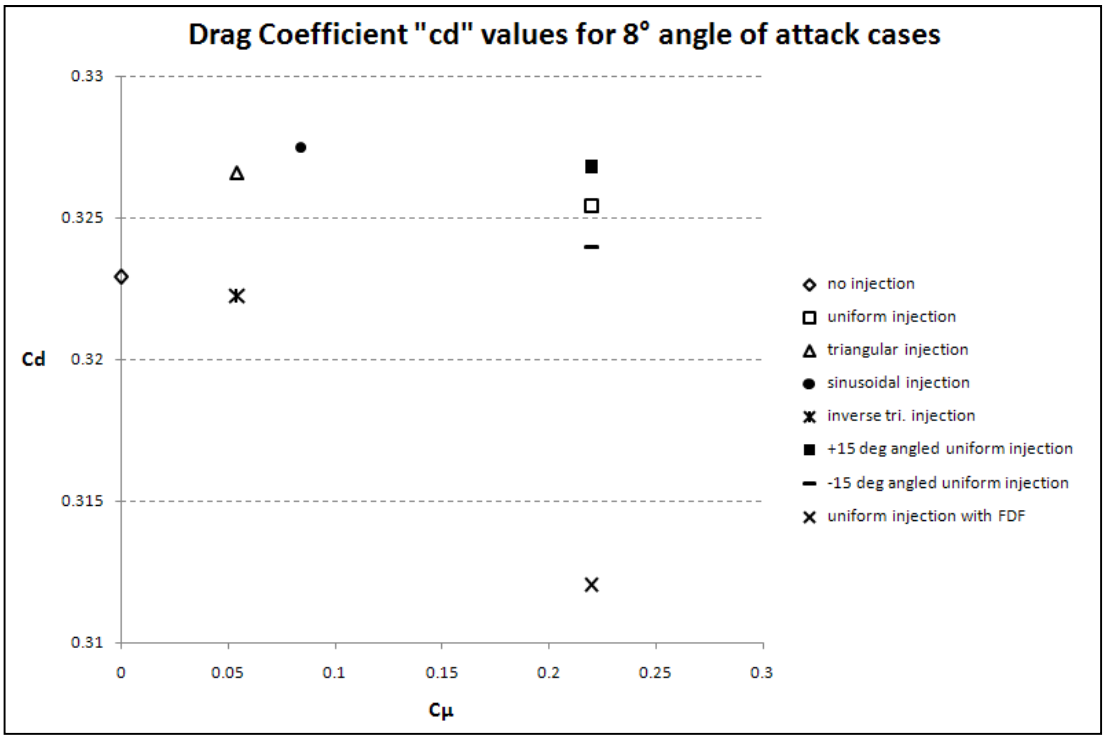

Figure 3.44: Drag coefficient for injection cases having 8° angle of attack configuration.

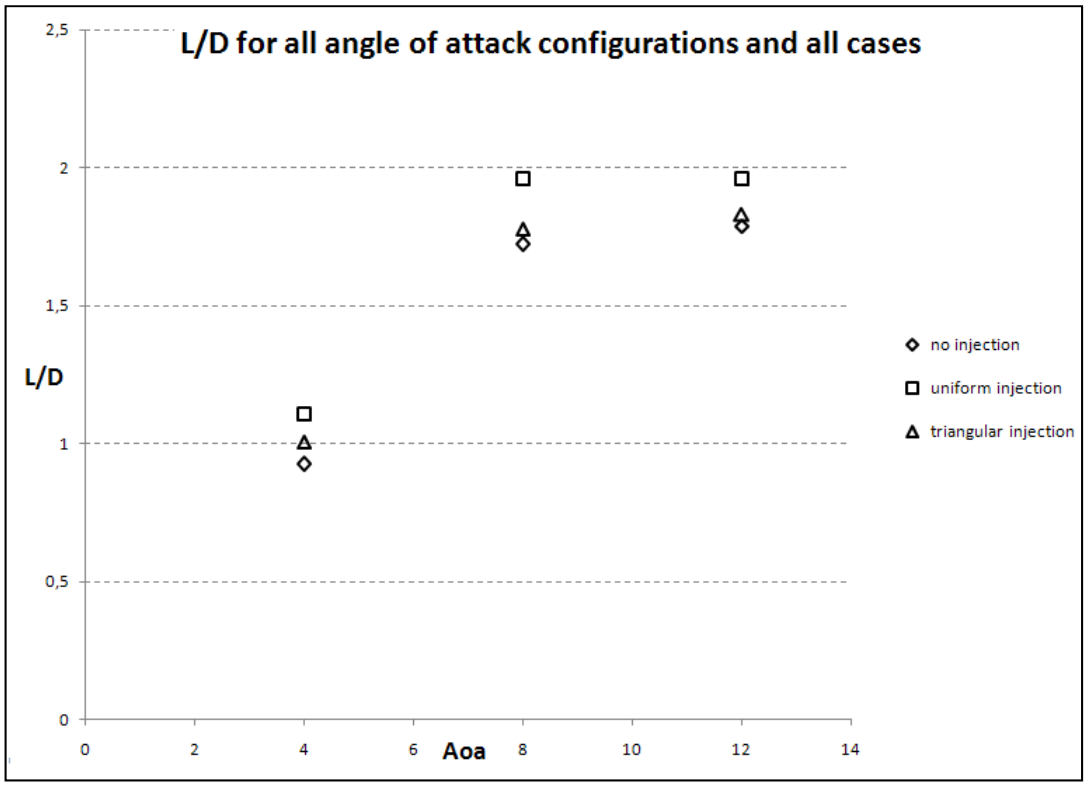

Figure 3.45: Lift-to-drag ratio for common cases at all angle of attack configurations

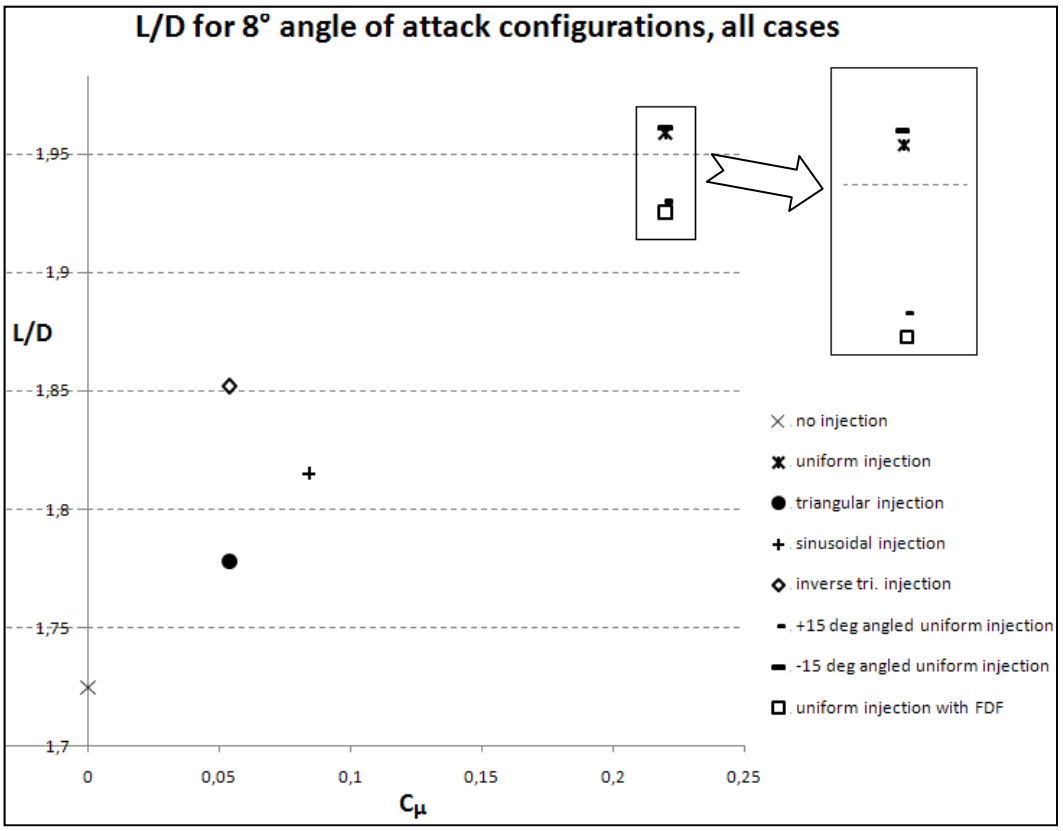

Figure 3.46: Lift-to-drag ratio for injection cases having 8° angle of attack configuration.

3.3 Validation with experimental results and vortex core locations:

The same study was conducted as a project which is sponsored by The Scientific and Technological Research Council of Turkey (TUBITAK) under the Project No 108M232. The measurements were performed using Constant Temperature Anemometry as well as Kiel probe traverses and located at x=2.0 c station with the wing that has 8° angle of attack configuration. The solution plane at specified destination does not cover the whole wind tunnel section. Planar solution zone (figure 3.47) starts close to the wing tip and combs a rectangular section.

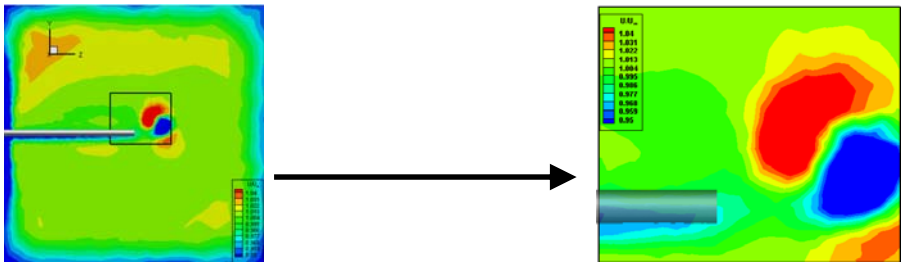

Figure 3.47: Experimental solution plane

The parameters that were compared are dimensionless U velocity having different injection scenarios, dimensionless total pressure, jet momentum coefficients and location of the vortex cores.

At first glance, U velocity results seem to be comparable when considering the range of the variable is the same (figure 3.48). The shape and the size of the low velocity fields are very similar to each other, yet CFD results seem to be more compatible with results of measurements with Kiel probe. While looking at pressure plots (figure 3.49), location and shape of the low pressure zones seem coherent; however slight differences at core were observed by means of magnitude.

Secondly, locations of vortex centers were plotted (figure 3.50, 3.51). The difference between experimental and computational results pointed out that there's a tendency of shifting the centers in an order. If cases were investigated individually, computational results have a consistency in itself with respect to experimental outputs. Thus it's a good practice for further studies to define a correction method for this solution behavior.

Furthermore, vortex diffusion distances were plotted for 8 angle of attack cases in order to determine the distance of diffusion by means of jet momentum coefficient. As seen on the figure 3.52, increase in the jet momentum coefficient creates stronger vortices with low core pressure and high rotational characteristics, causing the diffusion take longer time and distance.

Finally, vortex core locations of all injection cases were presented, as well as the change in the vortex center due to different injections. Effect of injection by means of expansion of the turbulent region and elevation of the vortex is seen on the figures 3.53 and 3.54 by comparing uniform, triangular waveform and no injection cases for 8° angle of attack configuration at different solution planes. As results, it's observed that, injection elevates and throws away tip vortex structures from the tip region while the turbulence intensity of vortex cores are increasing.

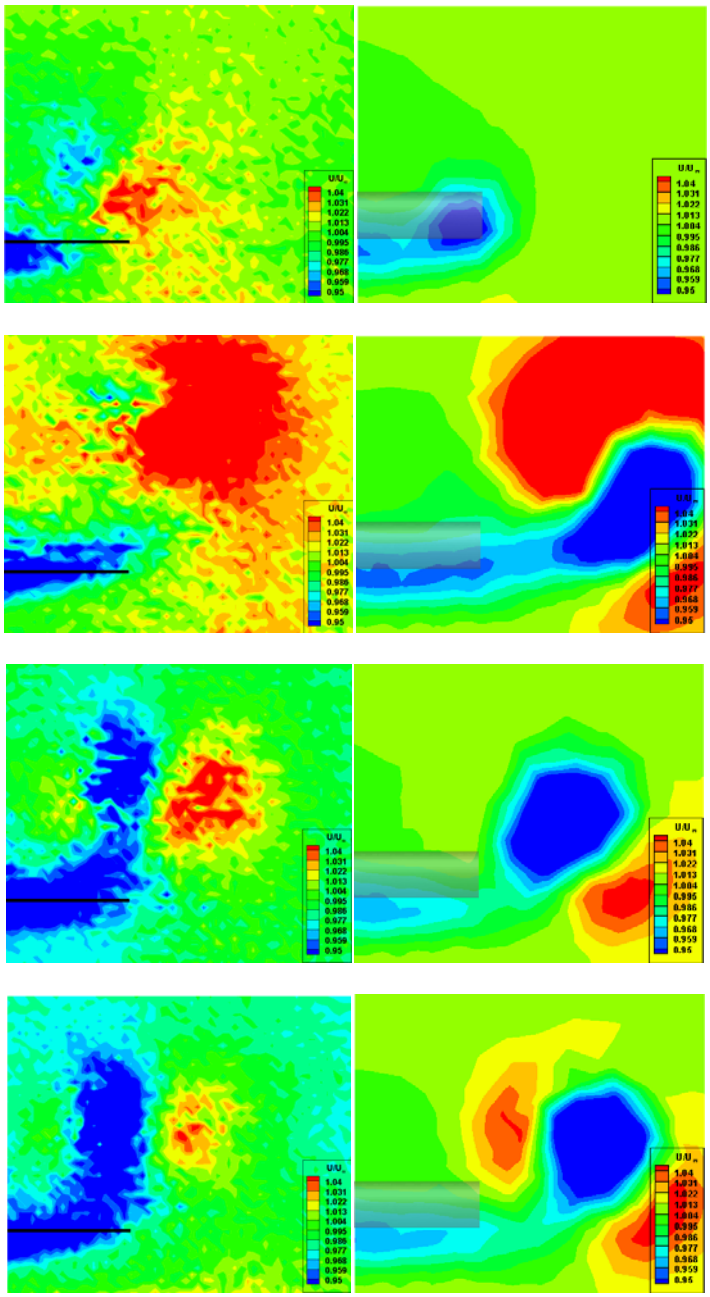

$C_\mu = 0$, no injection (1st row)

$C_\mu = 0.220$, uniform injection (2nd row)

$C_\mu = 0.054$, triangular waveform injection (3rd row)

$C_\mu = 0.084$, sinusoidal waveform injection (4th row)

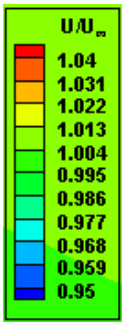

Figure 3.48: Dimensionless U plots, hotwire measurement results [1] (left), CFD results (right); from top to bottom, no injection, uniform injection, triangular injection and sinusoidal injection cases at x=2c station

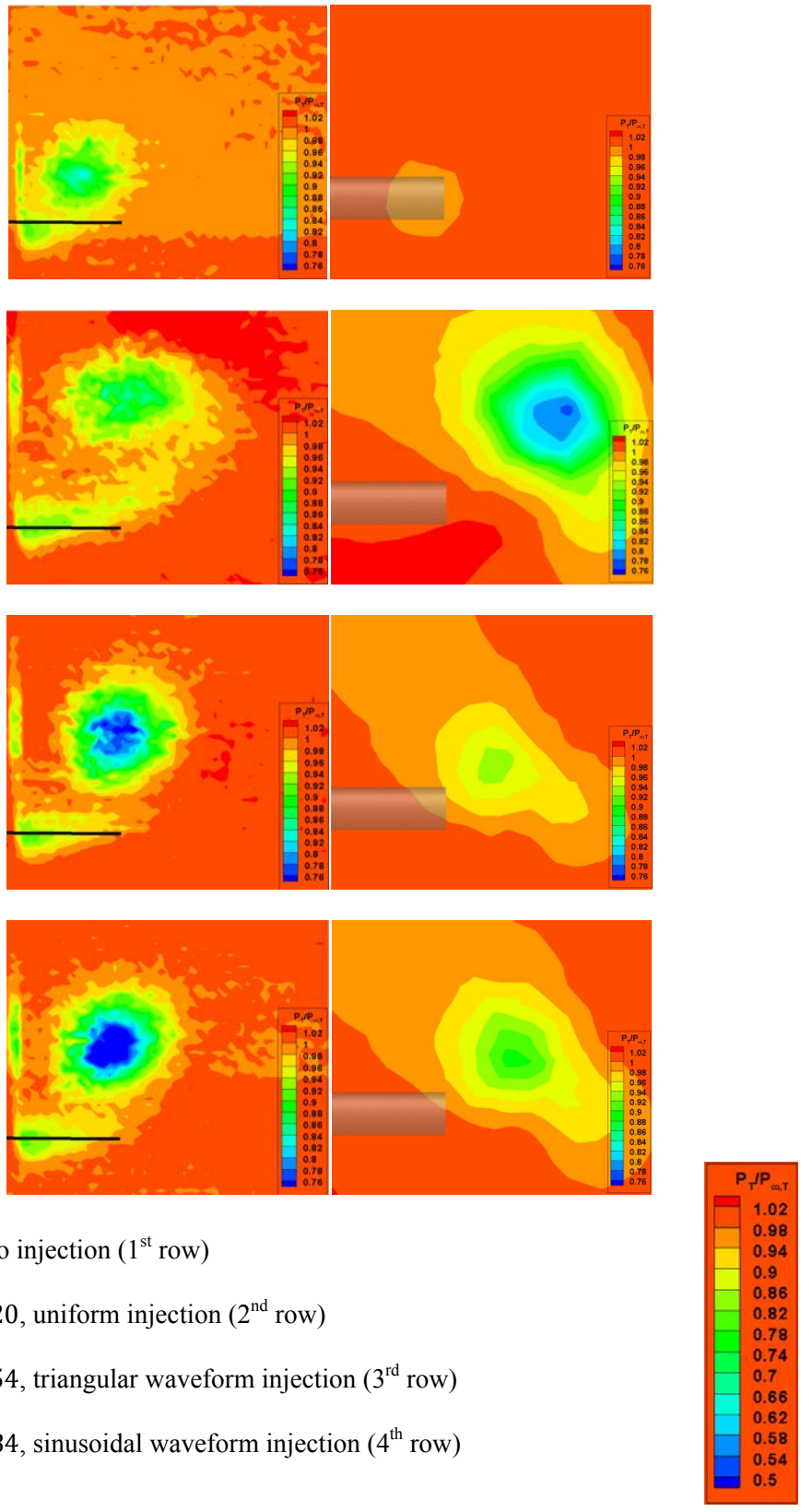

$C_\mu = 0$, no injection (1st row)

$C_\mu = 0.220$, uniform injection (2nd row)

$C_\mu = 0.054$, triangular waveform injection (3rd row)

$C_\mu = 0.084$, sinusoidal waveform injection (4th row)

Figure 3.49: Dimensionless pressure plots, measurement with Kiel probe results [1] (left), CFD results (right); from top to bottom, no injection, uniform injection, triangular injection and sinusoidal injection cases at x=2c station

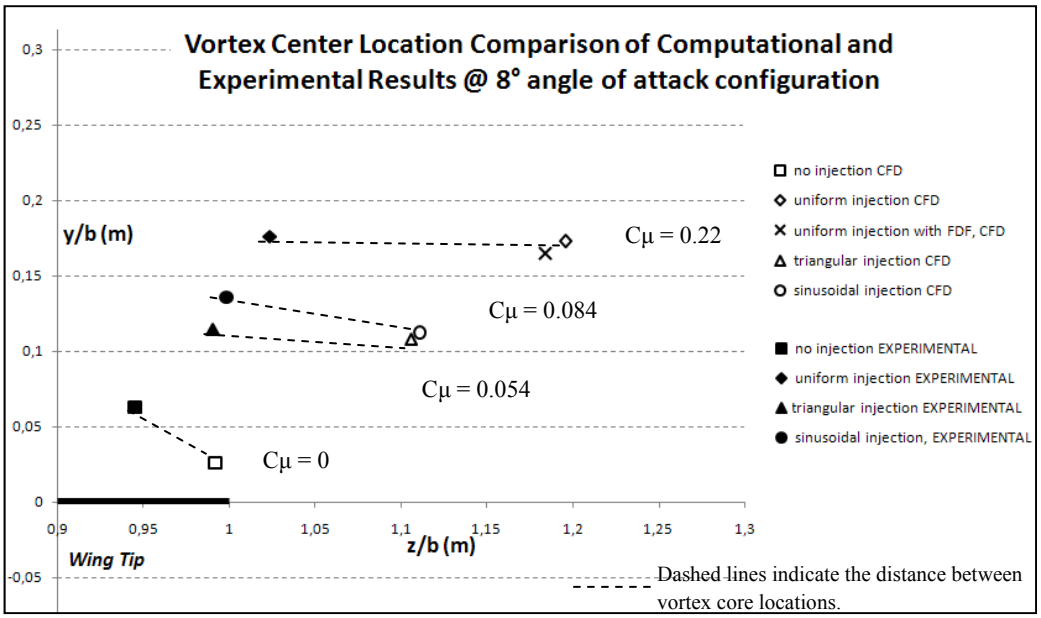

Figure 3.50: Comparison of vortex center locations

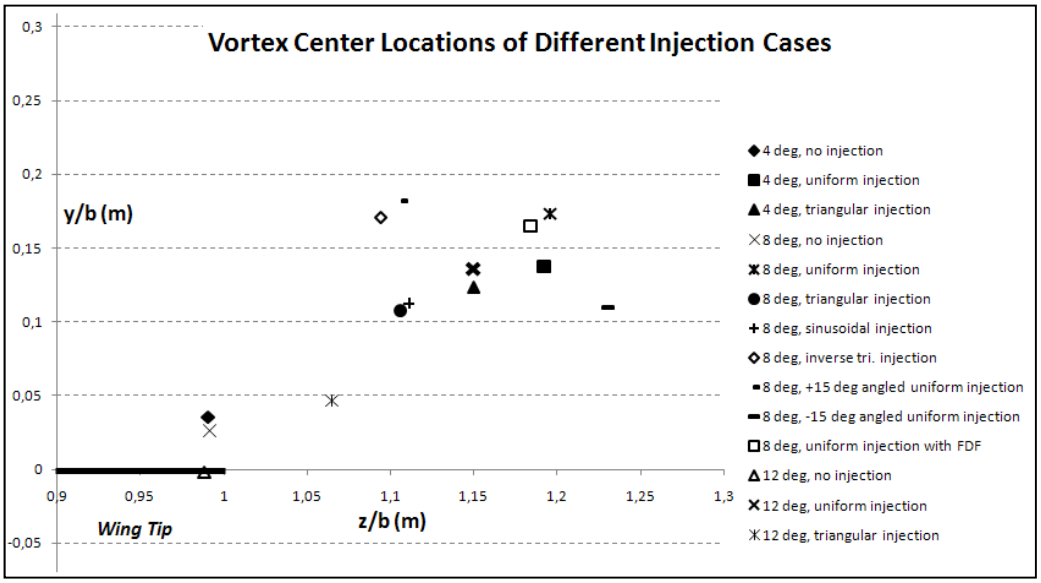

Figure 3.51: Comparison of vortex center locations of all cases

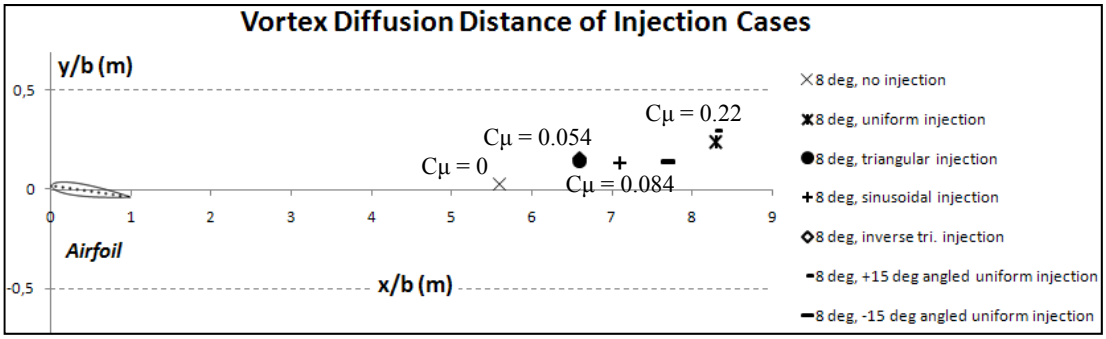

Figure 3.52: Comparison of vortex diffusion distances of 8° angle of attack cases

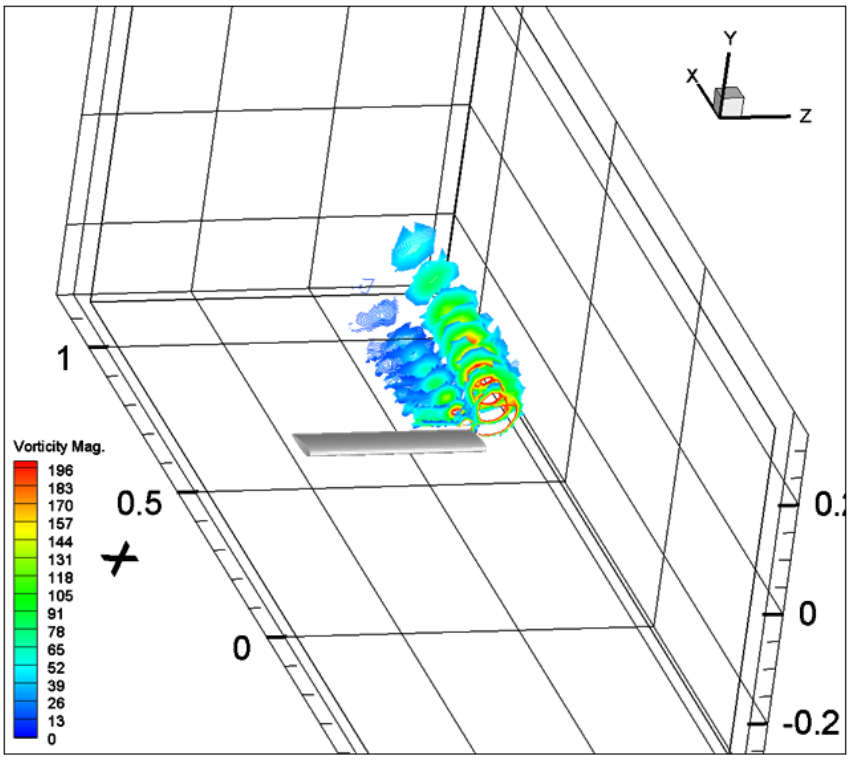

Figure 3.53: Comparison of vortex center locations of 8° angle of attack configuration, no injection (left), uniform injection (right)

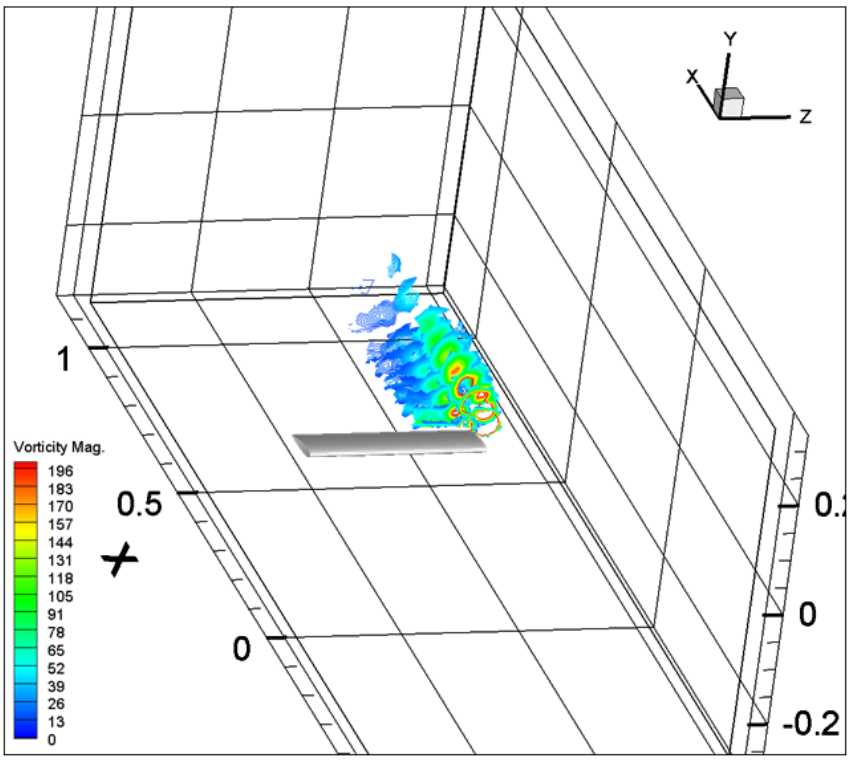

Figure 3.54: Comparison of vortex center locations of 8° angle of attack configuration, no injection (left), triangular waveform injection (right)

CHAPTER 4

CONCLUSION

In this thesis, the effect of tip injection to the wing tip vortices was presented as a computational study. A wing with an aspect ratio of 3 that has NACA0015 profile, which is located inside a wind tunnel as a cantilever beam was employed. Freestream velocity is 10 m/s, with a Reynolds number of 67000, which is compatible with experimental study. 3 different cases with injection scenarios namely, no injection, uniform injection and triangular waveform injection, were solved numerically for 3 different angle of attack configurations, e.g. 4°, 8° and 12°. In addition there are 5 more scenarios for 8° angle of attack configuration that are, sinusoidal waveform injection, reverse triangular waveform injection, two cases consisting of angled injections having both +15° and -15° with respect to the flapping axis of the wing. The last simulation was conducted in order to visualize the effect of tube walls on the jet injection, which was neglected for all cases. Therefore for the last case, in order to simulate pipe flow, a case is provided with uniform injection velocity. After the solutions are finalized, contour plots of variables, namely, dimensionless U, V and W velocities, turbulent kinetic energy, vorticity magnitude and pressure coefficient, were presented. A validation case for 8° angle of attack configuration by means of comparing U velocities and vortex core locations were provided.

Results show that, tip injection pushes tip vortices upwards and out of the wing tip region. For different jet momentum coefficient values, i.e. the term that defines the strength of the jet injection, vortex core locations were determined; with increasing jet momentum coefficient, it's observed that tip vortices are moved away and elevated from the tip. Avoiding the tip loss, lift generation was increased with the increasing effective wing area. Furthermore, diameter of the tip vortices enlarge and intensity of turbulence at the core region of vortices increases. Yet, comparing results of three different angle of attack configurations, it is observed that, turbulence intensity at the core decreases with increasing angle of attack. This is due to dispersion of the tip injection uniformity from leading edge to trailing edge; as at 4° angle of attack, tip jet flow tends to be blown more uniformly

considering the small angle between freestream and the wing, however as the angle becomes larger, the strength of the total injection diminishes.

Comparing lift and drag coefficient variations for all scenarios, uniform injection case came out to be the most efficient one considering all angle of attack configurations; especially when lift-to-drag ratios are compared, -15° uniform injection scenario turns out to be the most beneficial having the highest L/D.

In validation cases, it's observed that simulations have a good accuracy in determining the range of the velocity variable. The locations of the vortex center are lower than those in experimental results, yet for corresponding cases, when compared individually, displacements occur in a similar tendency.

In conclusion, tip injection changes the structure and characteristics of the tip vortices. Injection pushes vortex structures out of the tip zone with increasing jet momentum coefficient, alleviating effects of tip losses; in that way, lift generation is increased.

For future work, it's planned to run more simulations for different injection scenarios which will have the same overall jet momentum coefficient, but different injection types. Furthermore, unsteady tip injection cases, i.e. where the injection velocity is time dependant, will be studied. Comparison with corresponding experimental work will be presented, as well.

REFERENCES

[1] Mercan, B., Ostovan, Y., Dogan, E., Uzol, O., 2010, "Effect of Chordwise Modulated Waveform Tip Injection on the Characteristics of the Tip Vortex," AIAA 2010-4270, 40th Fluid Dynamics Conference and Exhibit 28 June - 1 July 2010, Chicago, Illinois.

[2] Gursul, I., Vardaki, E., Margaris, P., Wang, Z., 2007, "Control of Wing Vortices," Active Flow Control, Notes on Numerical Fluid Mechanics and Multidisciplinary Design, pp.137-151, Springer-Verlag Berlin.

[3] Matalanis, C. G., Nelson, G. D., Eaton, J. K., 2007, "Novel Aerodynamic Device for Wake Vortex Alleviation," AIAA Journal, Vol. 45, No. 9.

[4] Nie C., Tong, Z., Geng, S., Zhu, J., Huang, W., 2007, "Experimental Investigations of Micro Air Injection to Control Rotating Stall," Journal of Thermal Science, Vol. 16, No. 1.

[5] Geng, S., Zhang, H., Chen, J., Huang, W., 2007, "Numerical Study on the Response of Tip Leakage Flow Unsteadiness to Micro Tip Injection in a Low Speed Isolated Compressor Rotor," GT2007-27779, Proceedings of ASME Turbo Expo 2007, May 14-17 Montreal, Canada.

[6] Margaris, P., Gursul, I., 2007, "Vortex Topology of Wing Tip Blowing", AIAA 2007-1122. 45th AIAA

[7] Panagakos, A., Lee, T., 2006, "Tip Vortex Control via an Active Trailing Edge Tab," Journal of Aircraft, Vol. 43, No.4.

[8] Margaris, P., Gursul, I., 2006, "Wing Tip Vortex Control Using Synthetic Jets", Aeronautical Journal, Vol. 110, No. 1112, pp. 673-681.

[9] Cai, J., 2006 "LES for Wing Tip Vortex Around an Airfoil" Thesis, PhD, University of Texas at Arlington.

[10] Lu, X., Chu, W., Zhu, J., Tong, Z., 2006, "Numerical and Experimental Investigations of Steady Micro Tip Injection on a Subsonic Axial Flow Compressor Rotor," International Journal of Rotating Machinery, Vol. 2006, pp. 1-11.

[11] Greenblatt, D., Pack-Melton, L. G., Yao, C. S., Harris, J., 2005, "Active Control of a Wing Tip Vortex," AIAA 2005-4851. 23rd AIAA Applied Aerodynamics Conference, 6-9 June 2005, Toronto, Canada.

[12] Duraisamy, K., and Baeder, J., "Numerical Simulation of the Effects of Spanwise Blowing on Wing-Tip Vortex Formation and Evolution," AIAA Journal of Aircraft, Vol. 43 (4), 2005.

[13] Shojaefard et al., 2005, "Numerical Investigation of Flow Control by Suction and Injection on a Subsonic Airfoil", American Journal of Applied Sciences 2 (10), pp. 1474-1480.

[14] Coton, F. N., Green, R. B., Early, J. M., Price, J. L., 2005, "Amelioration of Blade Vortex Interaction Using Blade Tip Jets," American Helicopter Society, 61st Annual Forum Proceedings, pp. 1874-1885.

[15] May, D., 2005, “Wing Tip Vortex Dependence with Angle of Attack”, Thesis, Mechanical and Industrial Engineering, Concordia University, Montreal, Quebec, Canada.

[16] Viieru et al., 2005 “Effect of Tip Vortex on Wing Aerodynamics of Micro Air Vehicles”, Journal of Aircraft, Vol. 42, No. 6.

[17] Bae, J. W., Breuer, K. S., Tan, C. S., 2005, “Active Control of Tip Clearance Flow in Axial Flow Compressors,” ASME Journal of Turbomachinery, Vol. 127, pp. 352-362.

[18] Duraisamy, K., and Baeder, J., ``Control of Helicopter Rotor Tip Vortex Structure using Upper Surface Blowing", 60th Annual Forum of the American Helicopter Society, pp. 1952-1967, June 2004.

[19] Margaris, P., Gursul, I., 2004, “Effect of Steady Blowing on Wing Tip Flow Field,” AIAA 2004-2619. 2nd Flow Control Conference, Portland, Oregon, June-July 2004.

[20] Heyes, A. L., Smith, D. A. R., 2004, “Spatial Perturbation of a Wing Tip Vortex Using Pulsed Spanwise Jets,” Experiments in Fluids, Vol.37, pp. 120-127.

[21] Vasilescu, R., Dancila, D. S., 2003, “Modeling of Piezoelectrically Modulated and Vectored Blowing for a Wing Section,” AIAA 2003-219, 41st AIAA Aerospace Sciences Meeting and Exhibit, 6- 9 January 2003, Reno, Nevada.

[22] Menter, F. R., August 1994, "Two-Equation Eddy-Viscosity Turbulence Models for Engineering Applications," AIAA Journal, Vol. 32, No. 8, pp. 1598-1605.

[23] Shi, Z., 1990, “A Study of Jets in Crossflow and Its Application on Wing Tip Blowing”, Doctoral Thesis, University of Tennessee, Knoxville,.

[24] Cumpsty, N. A., 1989, Compressor Aerodynamics, Longman Group, London.

[25] Tavella, D. A., Wood, N. J., Lee, C. S., Roberts, L., 1988, “Lift Modulation with Lateral Wing-Tip Blowing, “Journal of Aircraft, Vol. 25, No. 4.

[26] Wisler, D. C., 1985, “Loss Reduction in Axial Flow Compressors through Low Speed Model Testing,” ASME Journal of Turbomachinery, Vol. 107, pp. 354-363.

[27] Smith, L. H. Jr., 1958, “The Effect of Tip Clearance on the Peak Pressure Rise of Axial Flow Fans and Compressors,” ASME Symposium on Stall, ASME, NY, pp. 149-152.

[28] Grid spacing calculator, http://geolab.larc.nasa.gov/APPS/YPlus/, 15.11.2010

[29] ANSYS FLUENT 6.3 documentation